A STUDY OF INTERWELL INTERFERENCE AND WELL PERFORMANCE IN UNCONVENTIONAL RESERVOIRS BASED ON COUPLED FLOW AND GEOMECHANICS MODELING WITH IMPROVED COMPUTATIONAL EFFICIENCY

A Dissertation

by

XUYANG GUO

Submitted to the Office of Graduate and Professional Studies of
Texas A&M University
in partial fulfillment of the requirements for the degree of

DOCTOR OF PHILOSOPHY

Chair of Committee,	John E. Killough
Co-Chair of Committee,	Kan Wu
Committee Members,	Maria A. Barrufet
	Eduardo Gildin
Head of Department,	Jeff Spath

August 2018

Major Subject: Petroleum Engineering

ABSTRACT

Completion quality of tightly spaced horizontal wells in unconventional reservoirs is important for hydrocarbon recovery efficiency. Parent well production usually leads to heterogeneous stress evolution around parent wells and at infill well locations, which affects hydraulic fracture growth along infill wells. Recent field observations indicate that infill well completions lead to frac hits and production interference between parent and infill wells. Therefore, it is important to characterize the heterogeneous interwell stress/pressure evolutions and hydraulic fracture networks. This work presents a reservoir-geomechanics-fracturing modeling workflow and its implementation in unconventional reservoirs for the characterization of interwell stress and pressure evolutions and for the modeling of interwell hydraulic fracture geometry.

An in-house finite element model coupling fluid flow and geomechanics is first introduced and used to characterize production-induced stress and pressure changes in the reservoir. Then, an in-house complex fracture propagation model coupling fracture mechanics and wellbore/fracture fluid flow is used for the simulation of hydraulic fractures along infill wells. A parallel solver is also implemented in a reservoir geomechanics simulator in a separate study to investigate the potential of improving computational efficiency.

Results show that differential stress (DS), parent well fracture geometry, legacy production time, bottomhole pressure (BHP) for legacy production, and perforation cluster location are key parameters affecting interwell fracture geometry and the occurrence of

frac hits. In general, transverse infill well fractures are obtained in scenarios with large DS and small legacy producing time/BHP. Non-uniform parent well fracture geometry leads to frac hits in certain cases, while the assumption of uniform parent well fracture half-lengths in the numerical model could not capture the phenomenon of frac hits. Perforation cluster locations along infill wells do not play an important role in determining whether an infill well hydraulic fracture is transverse, while they are important for the occurrence of frac hits.

In addition, the implementation of a parallel solver, PETSc, in a fortran-based simulator indicates that an overall speedup of 14 can be achieved for simulations with one million grid blocks. This result provides a reference for improving computational efficiency for geomechanical simulation involving large matrices using finite element methods (FEM).

DEDICATION

I dedicate this work to my parents.

ACKNOWLEDGEMENTS

In the first place, I want to express my gratitude to my advisor Professor John E. Killough for his support and insightful guidance. It is an honor that I have been receiving his advice since I was a senior at Texas A&M. I am especially grateful that he offered me the opportunity to join the reservoir simulation community. He also offered me the opportunities to work on some interesting research projects which form the foundation of this dissertation.

I also want to thank my co-advisor Professor Kan Wu for her patient guidance and for sharing her experience. She spent a lot of time making suggestions and reviewing my research. She also helped me to understand many concepts in geomechanics. I am always inspired by her passion.

I would like to thank Professor Maria A. Barrufet and Professor Eduardo Gildin for serving as my committee members. They both offered many suggestions on the work and helped to improve the work. The knowledge I learned from Dr. Barrufet's reservoir fluids class and Dr. Gildin's reservoir simulation class turned out to be quite useful for my research in the graduate school.

Thanks also go to members of Dr. Killough's research group and of Dr. Wu's research group. They offered many suggestions. I also thank the department faculty and staff for making the time in the department a great experience. The time I spent with my friends in the states and back in China is greatly appreciated as well.

Special thanks go to Professor Yuhe Wang of Texas A&M at Qatar and Professor Hongqing Song of University of Science and Technology Beijing for their valuable help on my research.

Finally, I am deeply indebted to my parents. They give me continuous support, encouragement, and selfless love. They also inspire me in my pursuit of academic goals.

CONTRIBUTORS AND FUNDING SOURCES

This work was supervised by a dissertation committee consisting of Professor John E. Killough [advisor], Professor Kan Wu [co-advisor] and Professor Eduardo Gildin of the Department of Petroleum Engineering and Professor Maria A. Barrufet of the Department of Chemical Engineering.

The implementation of an external/open-source finite element library described in Section 2.1 was originally prepared by Dr. Daegil Yang of Chevron. The geomechanics module described in Section 2.2 was prepared by Professor Jihoon Kim of the Department of Petroleum Engineering at Texas A&M University. The fracture model used in Section 5 was developed by Professor Kan Wu of the Department of Petroleum Engineering at Texas A&M University.

All other work conducted for this dissertation was completed by the student independently. The computational environment was configured with the help from Texas A&M High Performance Research Computing, who also provided access to the supercomputer for simulations in this work.

Graduate study was supported financially by the Crisman Institute for Petroleum Research at Texas A&M University.

NOMENCLATURE

DS	Differential Stress
BHP	Bottomhole Pressure
FEM	Finite Element Methods
MPI	Message Passing Interface
OpenMP	Open Multi-Processing
CRS	Compressed Row Storage
SRV	Stimulated Reservoir Volume
LGR	Local Grid Refinement
EDFM	Extended Discrete Fracture Model
GMRES	Generalized Minimal Residual Method
BiCG	Bi-Conjugate Gradient Method
BiCGSTAB	Bi-conjugate Gradient Stabilized Method
ILU	Incomplete LU Factorization
$\boldsymbol{v_{ws}}$	Relative velocity between the solid and water phases, m/s
$\boldsymbol{v_s}$	Solid phase rock rate, m/s
S_w	Water saturation, %
ρ_w	Water density, kg/m^3
ϕ	Porosity, %
q_w	Water sink/source, m^3/s
$\boldsymbol{v_{os}}$	Relative velocity between the solid and oil phases, m/s

S_o	Oil saturation, %
ρ_o	Oil density, kg/m^3
q_o	Oil sink/source, m^3/s
k_{rw}	Water relative permeability, dimensionless
k_{ro}	Oil relative permeability, dimensionless
μ_w	Water viscosity, Pa·s
μ_o	Oil viscosity, Pa·s
p_w	Water pressure, Pa
p_o	Oil pressure, Pa
$\boldsymbol{k}$	Second order permeability tensor
c_w	Water compressibility, 1/Pa
c_o	Oil compressibility, 1/Pa
t	Time, s
ε_v	Volumetric strain, Volume/Volume
b or α_f	Biot's coefficient, dimensionless
$\boldsymbol{u}$	Displacement vector
K_s	Bulk modulus, Pa
$\boldsymbol{v_t}$	Total velocity, m/s
λ_w	Water mobility, 1/ Pa·s
λ_o	Oil mobility, 1/ Pa·s
F_w	Water fractional flow, dimensionless
$\boldsymbol{\sigma}$	Stress tensor

$\boldsymbol{\sigma}_0$	Initial total stress tensor
p_0	Initial pressure, Pa
$\mathbf{1}$	Second order identity tensor
C_{dr}	Fourth order stiffness tensor
ε	Strain
∇^s	Symmetric gradient operator
$\boldsymbol{n}$	Outward unit normal vector
Γ	Boundary
$\boldsymbol{t}$	Boundary traction
h	Cell thickness of the well block
B_o	Oil formation volume factor
B_w	Water formation volume factor, m^3/m^3
r_w	Well radius, m
r_o	Effective well cell radius, m
P_{wf}	Bottomhole pressure, Pa
P_c	Well cell pressure, Pa
S_{w0}	Initial water saturation, %
v_a	Stabilization term for continuous Galerkin
β	Dimensionless stabilization constant
h_k	Cell diameter, m
γ	Shear strain, m/m
τ	Shear stress, Pa

λ	First Lame parameter, Pa
ν	Poisson's ratio, m/m
E	Young's modulus, Pa
G	Shear modulus, Pa
p_d	Dimensionless pressure
t_d	Dimensionless time
c_v	Consolidation coefficient, m^2/s
L_f	Distance to boundary, m
f	Fluid flow
m_f	Mass accumulation
$\mathbf{f}_f$	Mass flux
$\mathbf{g}$	Second order gravity tensor
H	Heat
m^H	Heat accumulation
$\mathbf{f}^H$	Heat flux
q^H	Sink/source for heat
T	Temperature, K
ρ_R	Rock density, m^3/s
C_R	Heat capacity of rock, J/(kg·K)
e_f	Specific internal energy of fluid, J/kg
$\mathbf{K}_H$	Second order composite thermal conductivity tensor

h_f	Specific enthalpy of the fluid, J/kg
M_g	Gas molar mass, kg/mol
R	Gas constant, J/(mol·K)
z_g	Real gas factor, dimensionless
ΔQ	Difference between cumulative productions, %
Δn	Difference between values of a studied parameter, %
$\frac{l_t}{l_f}$	Transverse percentage of a fracture, dimensionless
r_{id}	Idle time ratio, dimensionless

TABLE OF CONTENTS

Page

LIST OF FIGURES

Page

LIST OF TABLES

Page

1 INTRODUCTION

1.1 Background

Hydrocarbon production from unconventional reservoirs has made a great impact on the oil and gas industry. Significant production increases have been reported from many unconventional reservoirs worldwide (Kerr 2010; Jia et al. 2012; Weijermars et al. 2017). An effective way of developing unconventional reservoirs with low permeability is the usage of horizontal wells completed with multi-stage fractures (Cipolla et al. 2009; Daneshy 2011). In order to maximize the contact area with shale reservoirs and improve production, tightly spaced horizontal wells are often placed in reservoirs with close spacing (Marongiu-Porcu et al. 2015; Safari et al. 2017).

Infill wells are placed between parent wells to further increase hydrocarbon production in many cases. A strategy, the drill-to-hold practice, has been widely used in unconventional plays in the United States for the development of infill wells. In this strategy, operators only complete and produce one parent well in each lease to hold this lease while the completion and production of any infill well are postponed. As an example, in more than 2,000 leases in Eagle Ford Shale, only one well was drilled and produced in each lease (Railroad Commission of Texas 2015). Infill wells can be drilled and completed afterwards based on the decisions made by field operators.

Data indicate that in recent years, the growth of infill well is significant in many major unconventional plays in the United States such as Eagle Ford, Bakken, and

Haynesville (Miller et al. 2016; Lindsay et al. 2018). In these unconventional plays, the yearly newly drilled infill well numbers already surpassed the yearly newly dilled parent well numbers. For example, 70% of the newly drilled Eagle Ford wells were infill wells in 2017.

Rock deformation and production-induced stress changes in unconventional reservoirs have been paid attention. In reservoirs developed by parent and infill wells, the in-situ stress state is altered by depletion. The altered stress state has great impact on the completion quality of infill wells and the corresponding hydrocarbon production performance. This impact leads to production and fracturing interferences between parent wells and infill wells. Therefore, it is important to characterize the interaction between fluid flow and reservoir geomechanics and how this interaction affects hydraulic fractures. Currently, coupled flow and geomechanics models and hydraulic fracture models are widely used for the analysis and evaluation of interwell interference.

1.2 Literature Review

1.2.1 Interwell Interference

As well spacing between horizontal wells becomes closer in the development of shale reservoirs, interwell interference is observed when production is obtained from both parent wells and infill wells. Since production is affected by interwell interference, operators and researches have put many efforts in the understanding of this phenomenon. Interwell interferences are typically caused by connected hydraulic fractures, pressure interaction through shale matrix, and fracture hits (King and Valencia 2016; Cao et al.

2017). Ajani and Kelkar (2012) conducted a detailed study quantifying the production interference between closely spaced wells based on field data from Woodford Shale in Oklahoma. The strategy proposed in their study can determine the correlations between well age, well spacing, and positive and negative effects of interference on well production. Gupta et al. (2012) used an integrated modeling workflow to analyze the in-situ stress alterations due to depletion in several realistic field cases, which helps to design the optimum infill well placement, the best infill well completion, and the refracturing of wells with legacy production. Hydraulic fracture networks between parent wells and infill wells were identified as an important parameter affecting optimum production (Portis et al. 2013). Negative effects on production caused by the occurrence of frac hits were reported from Eagle Ford, Haynesville, and Marcellus (Yaich et al. 2014; Malpani et al. 2015). Marongiu-Porcu et al. (2016) studied the fracture interference in Eagle Ford Shale scenarios and proposed uneven drainage in the reservoir as an important reason affecting hydraulic fracturing. Recent efforts focusing on the characterizing and modeling of complex fracture networks associated with horizontal wells were reported for the evaluation of diffusivity equation and reservoir response using Fast Marching Method (King et al 2016; Wang et al. 2017; Wang et al. 2018). Safari et al. (2017) modeled the stress reorientation and interwell fracturing in reservoirs developed by tightly spaced wells and observed complex interwell fracturing results. Cao et al. (2017) proposed that frac hits can be used as an indicator of optimum well spacing in Wolfcamp formation in the Permian Basin. Similar observations were also introduced by Esquivel and Blasingame (2017) in Haynesville. Detailed analysis of frac hits was carried out by King et al. (2017)

and Rainbolt and Esco (2018), where they investigated the characteristics and causes of frac hits, and how to prevent and remediate frac hits. In a numerical study based on Permian Basin reservoir data, Ajisafe et al. (2017a) simulated the production interference between a parent well and an infill well. The cumulative production from the single parent well is actually greater than the total production from the parent well and the infill well, indicating a strong and negative effect of interwell interference in this specific case. Hwang et al. (2017) diagnosed the stress interference using multi-stage pumping data. Manchanda et al. (2018) explained the mechanism of parent and child well fracture interference and studied the mitigation methods. Similar analyses of interwell interference can also be found in Cipolla et al. (2011), Weng et al. (2014), and Bai et al. (2016). In such analyses, proper modeling of hydraulic fracture growth is important as it is the proxy of interwell communication (Liu and Ehlig-Economides 2015; Tang et al. 2017; Liu and Ehlig-Economides 2017; Zhou et al. 2017; Xie et al. 2018). The production contribution of individual hydraulic fractures can also be quantified by semi-analytical models (He et al. 2017a; He et al. 2017b; He et al. 2017c). Recently, attempts were made to alleviate the interwell interference caused by legacy production. Such attempts include refracturing of parent wells and loading (injecting) parent wells with fluid. Gakhar et al. (2017) discussed the effects of parent well refracturing and recharging in infill well completion cases. Bommer et al. (2017) and Bommer and Bayne (2018) loaded parent wells in Bakken Shale with fluids to defend their parent well productions and reported mixed performances.

Based on the review, the existence of interwell interference has been proved by field observations, and numerical models have been widely used to understand the mechanism of this interference.

1.2.2 Coupled Flow and Geomechanics Modeling

Frac hits and the associated hydraulic fractures are key parameters in the understanding of interwell interference. Two important variables, reservoir pressure and in-situ stress state, directly affect the networks of hydraulic fractures between parent wells and infill wells. In order to obtain the spatial and temporal evolutions of pressure and stress, coupled flow and geomechanics modeling based on consolidation theories is widely used in the literature. Terzaghi (1923; 1925) first presented the concept of effective stress in consolidation, and his contribution serves as a foundation for the study of the fluid and rock interaction. In addition, Biot's theory of poroelasticity is widely used to describe the poromechanical interaction (Biot 1941; Biot 1955). The use of these consolidation theories in reservoir engineering in the petroleum industry is important for the coupled modeling of fluid flow and geomechanics (Bataee and Irawan 2014). As an extension, Geertsma (1966) first introduced the theory of poroelasticity for a unified treatment of rock mechanics in petroleum engineering and the subsidence caused by compaction was discussed.

Based on the concepts of consolidation in reservoir rocks, the coupled processes of flow in porous media and rock deformation can be modeled. Instead of using constant rock compressibility to denote the simplified rock deformation process, full geomechanics

should be coupled with fluid flow for better accuracy and reliability. Several methods are used for the coupling between flow and geomechanics: full coupling, explicit coupling, and iterative coupling (Dean et al. 2006). The fully coupled method solves flow and geomechanics problems in one system. It has the optimum accuracy, stability, and reliability, while the associated computational cost is also very significant (Chin and Thomas 1999; Settari and Walters 2001; Chin et al. 2002; Dean et al. 2006). The explicitly coupled method solves the flow problem and the geomechanics problem separately, and the solutions are updated at certain time steps for the coupled processes (Minkoff et al. 2003). This method improves the computational speed while sacrifices accuracy and stability. The iteratively coupled method solves flow and geomechanics separately, and their solutions are iteratively communicated between the two problems at a time step until the system becomes convergent. Thus, the computational cost is relatively reduced while the accuracy and stability of solutions are improved (Tran et al. 2004; Kim et al. 2011; Kim et al. 2012; Mikelic and Wheeler 2013).

Based on the consolidation theories related to reservoir engineering and the coupling strategies, many sophisticated mathematical models were developed to characterize the relationship between stress and pressure in the coupled problem of fluid flow and reservoir geomechanics. Settari and Mourtis (1998) modeled the joint system considering all effects of geomechanics, multiphase behaviors, fracturing, and heat transport in the subsurface reservoirs where the coupling was achieved by iterative methods. Gai et al. (2003) proposed a numerical simulator that couples geomechanics with fluid flow. The model also has parallel computing capability. Rutqvist and Stephansson

(2003) provided a comprehensive review of the coupling strategies for hydromechanical considerations in fractured rocks, and indicated that there were still many uncertainties in the quantification of complex hydromechanical problems. Wan et al. (2003) presented a coupled flow and geomechanics study considering stress sensitive formations. A stabilized method was used in the study to provide improved stability in the numerical solution in terms of reducing the pressure oscillation in the solution. Dean et al. (2006) compared three different coupling strategies between flow and geomechanics (explicitly coupled, iteratively coupled, and fully coupled), and concluded that as long as strict tolerance is used, three strategies lead to similar simulation results. Wheeler and Gai (2007) pointed out that the values of permeability and fluid compressibility are key parameters determining the convergence in a sequentially coupled system. Kim et al. (2009) studied the accuracy, stability, and efficiency of several different iterative coupling methods for hydromechanical problems and proposed that the fixed-stress method provides good convergence and stability. The undrained split method is also unconditionally stable. The other two sequential coupling methods, drained split and fixed-strain split, are conditionally stable. Dean and Schmidt (2009) developed a geomechanical reservoir simulator considering complex subsurface behaviors of fracture growth, heat transport, deposition, elastoplastic deformation, and multiphase-multicomponent flows. Zoback (2007) provided detailed discussions of the reservoir geomechanical problems and their interaction with fluid flow. Roussel et al. (2013) introduced a finite element model that couples hydromechanical problems, and presented several case studies describing the stress evolution correlated with pore pressure depletion. Yang et al. (2014) developed a

fully coupled 3D simulator that considers multiphase flow and linear elasticity, where an external finite element library was applied for the space discretization. Alpak (2015) introduced a robust simulator that couples multiphase flow with geomechanics using the fully implicit strategy. Shovkun and Espinoza (2017) presented a coupled model which takes into account the effects of stress sensitivity, desorption, fine migration, and shear failure. Their model was used in case studies based on data from gas reservoirs in San Juan coal basin and Barnett Shale. Thermal effects coupled with fluid flow and rock deformation in subsurface porous media were also considered in a numerical modeling study for thermal-hydraulic-mechanical behaviors (Guo et al. 2018c).

Previous studies also pointed out that the coupling of geomechanical effects has an impact on the production solution, although the effects are usually not significant. Yu and Sepehrnoori (2014) incorporated a compaction table denoting stress sensitivity in a reservoir simulation, and indicated that, compared to flow-only simulation, the gas production rate is decreased when the geomechanical effects are considered. Moradi et al. (2017) also reported that incorporating stress sensitivity in their coupled simulator leads to decreased production rate, which was explained by the fracture aperture change due to hydromechanical effects in the reservoir. An et al. (2017) developed a coupled flow and geomechanics model and simulated the effects of matrix shrinkage and stress sensitivity on permeability and hydrocarbon production in shale reservoirs, and found out that production decreases with the increase of geomechanical effects.

1.2.3 Parallel Simulation for Coupled Flow and Geomechanics

When coupled flow and geomechanics modeling is applied to problems with field-scale, large numbers of cells are usually required to improve the accuracy of the modeling work. However, this leads to large stiffness matrices in the geomechanics problem and large coefficient matrices in the flow problem. In order to improve the efficiency in solving such large matrices, high performance computing is often used in these coupled simulations.

Thomas et al. (2002) developed a coupled flow and geomechanics simulator using iterative methods. Parallel computing based on message passing interface was incorporated in the simulator so that field-scale problems can be solved economically. Domain decomposition was used to partition the mesh, and bi-conjugate gradient method preconditioned by ILU was used for the solver. Gai et al. (2003) presented a parallel simulator considering poroelasticity and multiphase fluid flow. Iterative coupling was applied for the flow-geomechanics problem, and a strategy called super coarsening multigrid routine was incorporated after preconditioning to further improve the simulator's scalability and convergence rate. Reagan et al. (2013) first discussed a parallel simulation study of a realistic 3D gas hydrate reservoir which solves more than nine million equations at each step. This was the largest TOUGH simulation back then. However, the authors mentioned that the simulation did not capture enough active and productive behaviors such as gas formation and dissociation. Wang (2014) developed a parallel simulator for coupled flow and geomechanics considering wellbore deformation, compaction, fracturing, and sand production. Finite element methods were used and good

scalability was achieved in the simulation on massively parallel clusters. Luo et al. (2015) introduced a parallel framework for geomechanics simulation coupled with reservoir simulation. The coupling was achieved by iterative coupling. They found out that matrix assembly and secondary parameter updates have the optimum speedups while the overall simulation has lower speedups. In a coupled poromechanical study, White et al. (2016) investigated preconditioning methods in parallel simulation. Good scaling of the parallel simulation was observed for both fully implicit and sequentially implicit methods.

1.3 Motivation

Based on the literature review, it is noted that the coupled subsurface behaviors of fluid flow and rock deformation are widely modeled for the analysis of interwell interference, and the computational efficiency of the coupled modeling is investigated due to its relatively high computational load. Two aspects motivated by previous studies are considered in this work: (1) a detailed and comprehensive analysis using a coupled flow and geomechanics model considering parameters not well discussed in the literature is needed; (2) a portable parallelization scheme providing practical speedup of coupled flow and geomechanics codes can decrease the code re-development effort if a serial code exists.

1.3.1 Detailed Interwell Interference Analysis

A detailed interwell interference analysis in unconventional reservoirs serves as a complement to the studies conducted in the literature. Thus, a more comprehensive understanding of interwell interference can be obtained.

First, previous studies involving coupled simulations largely focused on uniform hydraulic fractures along parent wells (Gupta et al. 2012; Roussel et al. 2013; and Safari et al. 2017), and this assumption ignores the effects of hydraulic fracture geometry on interwell interference. In fact, according to field diagnostics, hydraulic fractures along parent wells usually have non-uniform half-lengths and complex geometries (Webster et al. 2013; Wheaton et al. 2014; Ugueto et al. 2016). Although some studies considered non-uniform hydraulic fractures (Ajisafe et al. 2017a; Ajisafe et al. 2017b), they primarily focused on the simulation of realistic cases and the detailed parametric studies were not thoroughly discussed. In this study, parametric studies with sensitivity analyses are carried out considering non-uniform parent well hydraulic fractures.

Second, the modeling of frac hits in infill well completion scenarios was not well discussed in the literature. While the occurrence of frac hits caused by infill well completion was proved by field reports (Esquivel and Blasingame 2017; King et al. 2017; Rainbolt and Esco 2017; Cao et al. 2017), typical modeling studies were not very effective in capturing frac hits. For example, Rezaei et al. (2017a) and Rezaei et al. (2017b) presented the simulation of infill well completion in a reservoir with legacy parent well production, and they reported that the infill well hydraulic fractures always grow longitudinally and avoid parent well hydraulic fractures. Roussel et al. (2013) using

similar case setup presented that infill well hydraulic fractures grow longitudinally when they approach fracture tips of hydraulic fractures along parent wells, leading to interwell hydraulic fracture networks without any frac hits. These indicate that the typical setups in such studies do not comprehensively represent the geomechanical behaviors in the field. Modification of such setup should be made so that the modeling work can capture frac hits. Thus, the mechanism of frac hits from the perspective of geomechanics can be analyzed by numerical modeling studies.

Third, since geomechanics is coupled with flow in porous media, a set of sensitivity analyses is required to quantify its effects on the simulated reservoir response. Previous coupled flow and geomechanics studies analyzed the effects such as organic component (An et al. 2017) and fracture aperture (Moradi et al. 2017), while some other parameters were ignored.

1.3.2 Portable Parallelization Scheme

Large-scale geomechanics problems solved by finite element methods usually have large stiffness matrices and total degree of freedom, which results in heavy computational load. Parallel computing is usually used for improved computational efficiency. Many sophisticated parallelization schemes like multigrid and domain decomposition can usually provide good scalability for parallel performance. However, they also require massive code re-development effort.

In this study, a parallel solver is incorporated in a serial code that couples flow and geomechanics in an attempt to achieve practical speedup while minimum code re-

development effort is introduced in the parallelization. This parallel scheme mainly focuses on the parallel assembly of linear system and the parallel solver for matrix solution, which only require the re-development of several subroutines of a serial code.

1.4 Dissertation Outline

There are seven Sections in this work. After the introduction in Section 1, Section 2 presents two coupled flow and geomechanics simulators. The first simulator fully couples two-phase isothermal fluid flow with linear elasticity. The second simulator is a parallel simulator which sequentially couples the single-phase non-isothermal fluid flow with elastoplasticity. Using the first simulator, Section 3, Section 4, and Section 5 presents the studies of geomechanical effects on well performance and reservoir response, production-induced stress reorientation in unconventional reservoirs, and detailed interwell fracturing interference between parent and infill wells. In Section 6, the parallel performance of the second simulator is presented. It also investigates the effects of production/injection, plasticity, and matrix decomposition on parallel performance. Conclusions and future work are presented in Section 7.

2 METHODOLOGY*

Two models are presented in this section. The first model is a fully coupled flow and geomechanics model based on finite element methods which couples two-phase black oil model with linear elasticity. This model is used for the well performance and interwell interference studies in Sections 3-5. The second model is a parallel model which sequentially couples fluid-heat flow with elastoplasticity. MPI-based parallel solver and OpenMP are used for the parallelization. Section 6 is based on the second model. It is noted that the two models presented in this section belong to separate studies and are not related, and the numerical results in Sections 3-5 are not related to results in Section 6.

*Part of this section is reprinted with permission from "Pressure Characteristics and Performance of Multi-Stage Fractured Horizontal Well in Shale Gas Reservoirs with Coupled Flow and Geomechanics" by X. Guo, H. Song, K. Wu, and J. Killough. Journal of Petroleum Science and Engineering, Copyright [2018] by Elsevier, from "Hybrid MPI-OpenMP Scalable Parallelization for Coupled Non-Isothermal Fluid-Heat Flow and Elastoplastic Geomechanics" by X. Guo, J. Kim, and J. Killough. SPE Proceedings, Copyright [2017] by Society of Petroleum Engineers, and from "Investigation of Production-Induced Stress Changes for Infill Well Stimulation in Eagle Ford Shale" by X. Guo, K. Wu, and J. Killough. SPE Journal, Copyright [2018] by Society of Petroleum Engineers.

2.1 Fully Coupled Flow and Geomechanics Modeling

2.1.1 Governing Equations

In this model, the flow problem is based on mass conservation and the geomechanics problem is based on linear elasticity. The two problems are fully coupled and solved within the same linear system for stability and accuracy. The model is extended from the formulations presented in Yang et al. (2014).

Based on mass conservation, the two-phase flow diffusivity for water and oil is in Eqs. 2.1 and 2.2 as

$$\frac{\partial(\phi S_w \rho_w)}{\partial t} + \nabla \cdot [\phi S_w \rho_w (\boldsymbol{v_{ws}} + \boldsymbol{v_s})] = \rho_w q_w, \tag{2.1}$$

$$\frac{\partial(\phi S_o \rho_o)}{\partial t} + \nabla \cdot [\phi S_o \rho_o (\boldsymbol{v_{os}} + \boldsymbol{v}_s)] = \rho_o q_o, \tag{2.2}$$

where $(\boldsymbol{v_{ws}} + \boldsymbol{v_s})$ is the water interstitial velocity, $\boldsymbol{v_{ws}}$ is the relative velocity between the solid phase and water phase, $\boldsymbol{v_s}$ is the deformation rate of solid phase rock due to flow in porous media, S_w is water saturation, ρ_w is the density of water, ϕ is porosity, q_w is the water sink/source term. Similarly, $(\boldsymbol{v_{os}} + \boldsymbol{v_s})$ is the oil interstitial velocity, $\boldsymbol{v_{os}}$ is the relative velocity between the solid phase and oil phase, S_o is oil saturation, ρ_o is the density of oil, q_o is the oil sink/source term. In general, $\frac{\partial(\phi S_w \rho_w)}{\partial t}$ and $\frac{\partial(\phi S_o \rho_o)}{\partial t}$ are the accumulation terms; $\nabla \cdot [\phi S_w \rho_w (\boldsymbol{v_{ws}} + \boldsymbol{v_s})]$ and $\nabla \cdot [\phi S_o \rho_o (\boldsymbol{v_{os}} + \boldsymbol{v}_s)]$ are the flux terms; $\rho_w q_w$ and $\rho_o q_o$ are the sink/source terms.

Darcy's law is used in the calculation of flux terms (Hubbert 1956) for both water and oil phases as

$$\boldsymbol{v_w} = \phi S_w \boldsymbol{v_{ws}} = -\frac{\boldsymbol{k} k_{rw}}{\mu_w} \nabla p_w, \tag{2.3}$$

$$\boldsymbol{v_o} = \phi S_o \boldsymbol{v_{os}} = -\frac{\boldsymbol{k} k_{ro}}{\mu_o} \nabla p_o, \tag{2.4}$$

where k_{rw} is water relative permeability, k_{ro} is oil relative permeability, μ_w is water viscosity, μ_o is oil viscosity, p_w is water phase pressure, p_o is oil phase pressure, $\boldsymbol{k}$ is the second order permeability tensor. The effect of gravity is not considered.

Eqs. 2.1 and 2.2 are also written as

$$\frac{\partial(\phi S_w \rho_w)}{\partial t} + \nabla \cdot (\phi S_w \rho_w \boldsymbol{v_{ws}}) + \nabla \cdot (\phi S_w \rho_w \boldsymbol{v_s}) = \rho_w q_w, \tag{2.5}$$

$$\frac{\partial(\phi S_o \rho_o)}{\partial t} + \nabla \cdot (\phi S_o \rho_o \boldsymbol{v_{os}}) + \nabla \cdot (\phi S_o \rho_o \boldsymbol{v_s}) = \rho_o q_o, \tag{2.6}$$

which are identical to the following forms

$$\frac{\partial(\phi S_w \rho_w)}{\partial t} + \nabla \cdot (\phi S_w \rho_w \boldsymbol{v_{ws}}) + \boldsymbol{v_s} \cdot \nabla(\phi S_w \rho_w) + \phi S_w \rho_w \nabla \cdot \boldsymbol{v_s} = \rho_w q_w, \tag{2.7}$$

$$\frac{\partial(\phi S_o \rho_o)}{\partial t} + \nabla \cdot (\phi S_o \rho_o \boldsymbol{v_{os}}) + \boldsymbol{v_s} \cdot \nabla(\phi S_o \rho_o) + \phi S_o \rho_o \nabla \cdot \boldsymbol{v_s} = \rho_o q_o. \tag{2.8}$$

Based on Eqs. 2.3 and 2.4, Eqs. 2.7 and 2.8 are written as

$$\frac{\partial(\phi S_w \rho_w)}{\partial t} + \nabla \cdot (\rho_w \boldsymbol{v_w}) + \boldsymbol{v_s} \cdot \nabla(\phi S_w \rho_w) + \phi S_w \rho_w \nabla \cdot \boldsymbol{v_s} = \rho_w q_w, \tag{2.9}$$

$$\frac{\partial(\phi S_o \rho_o)}{\partial t} + \nabla \cdot (\rho_o \boldsymbol{v_o}) + \boldsymbol{v_s} \cdot \nabla(\phi S_o \rho_o) + \phi S_o \rho_o \nabla \cdot \boldsymbol{v_s} = \rho_o q_o. \tag{2.10}$$

Concepts of material derivatives in continuum mechanics are used for the two-phase flow of water and oil as

$$\frac{d(\phi S_w \rho_w)}{dt} = \frac{\partial(\phi S_w \rho_w)}{\partial t} + \boldsymbol{v_s} \cdot \nabla(\phi S_w \rho_w), \tag{2.11}$$

$$\frac{d(\phi S_o \rho_o)}{dt} = \frac{\partial(\phi S_o \rho_o)}{\partial t} + \boldsymbol{v_s} \cdot \nabla(\phi S_o \rho_o). \tag{2.12}$$

Using the assumption of infinitesimal deformation $\frac{\partial(\phi\rho_w)}{\partial t} \gg \boldsymbol{v_s} \cdot \nabla(\phi\rho_w)$ and $\frac{\partial(\phi\rho_o)}{\partial t} \gg \boldsymbol{v_s} \cdot \nabla(\phi\rho_o)$, Eqs. 2.11 and 2.12 are written as

$$\frac{d(\phi S_w \rho_w)}{dt} \approx \frac{\partial(\phi S_w \rho_w)}{\partial t}, \tag{2.13}$$

$$\frac{d(\phi S_o \rho_o)}{dt} \approx \frac{\partial(\phi S_o \rho_o)}{\partial t}. \tag{2.14}$$

Using Eqs. 2.13 and 2.14 in Eqs. 2.9 and 2.10,

$$\frac{\partial(\phi S_w \rho_w)}{\partial t} + \nabla \cdot (\rho_w \boldsymbol{v_w}) + \phi S_w \rho_w \nabla \cdot \boldsymbol{v_s} = \rho_w q_w, \tag{2.15}$$

$$\frac{\partial(\phi S_o \rho_o)}{\partial t} + \nabla \cdot (\rho_o \boldsymbol{v_o}) + \phi S_o \rho_o \nabla \cdot \boldsymbol{v_s} = \rho_o q_o. \tag{2.16}$$

Water and oil compressibilities are written as

$$c_w = \frac{1}{\rho_w}\frac{\partial \rho_w}{\partial p_w}, \tag{2.17}$$

$$c_o = \frac{1}{\rho_o}\frac{\partial \rho_o}{\partial p_o}, \tag{2.18}$$

where c_w and c_o can be incorporated in Eqs. 2.15 and 2.16 as

$$S_w \rho_w \frac{\partial \phi}{\partial t} + \rho_w \phi \frac{\partial S_w}{\partial t} + \phi S_w \rho_w c_w \frac{\partial p_w}{\partial t} + \nabla \cdot (\rho_w \boldsymbol{v_w}) + \phi S_w \rho_w \nabla \cdot \boldsymbol{v_s} = \rho_w q_w, \tag{2.19}$$

$$S_o \rho_o \frac{\partial \phi}{\partial t} + \rho_o \phi \frac{\partial S_o}{\partial t} + \phi S_o \rho_o c_o \frac{\partial p_o}{\partial t} + \nabla \cdot (\rho_o \boldsymbol{v_o}) + \phi S_o \rho_o \nabla \cdot \boldsymbol{v_s} = \rho_o q_o, \tag{2.20}$$

where porosity term ϕ is treated as a function of time.

The time derivative of porosity can be described by the coupling between bulk volume and pore volume based on Geertsma (1957) and Biot and Willis (1957) as

$$\frac{\partial \phi}{\partial t} = \frac{b-\phi}{K_s}\frac{\partial p}{\partial t} + (b-\phi)\frac{\partial \varepsilon_v}{\partial t}, \tag{2.21}$$

where p is the total pressure of the two-phase flow. In this study, capillary pressure is neglected so that p can be replaced by p_w or p_o. ε_v is the volumetric strain. b is Biot's coefficient.

By definition, the solid phase rate $\boldsymbol{v_s}$ is equal to the time derivative of displacement $\boldsymbol{u}$ as

$$\boldsymbol{v_s} = \frac{\partial \boldsymbol{u}}{\partial t}. \tag{2.22}$$

Also, the relationship between volumetric strain ε_v and displacement $\boldsymbol{u}$ is as

$$\varepsilon_v = \nabla \cdot \boldsymbol{u}. \tag{2.23}$$

Using Eqs. 2.21, 2.22 and 2.23 in Eqs 2.19 and 2.20,

$$S_w\rho_w\left[\frac{b-\phi}{K_s}\frac{\partial p_w}{\partial t} + (b-\phi)\frac{\partial \varepsilon_v}{\partial t}\right] + \rho_w\phi\frac{\partial S_w}{\partial t} + \phi S_w\rho_w c_w\frac{\partial p_w}{\partial t} + \nabla\cdot(\rho_w\boldsymbol{v_w}) + \phi S_w\rho_w\frac{\partial \varepsilon_v}{\partial t} = \rho_w q_w, \tag{2.24}$$

$$S_o\rho_o\left[\frac{b-\phi}{K_s}\frac{\partial p_o}{\partial t} + (b-\phi)\frac{\partial \varepsilon_v}{\partial t}\right] + \rho_o\phi\frac{\partial S_o}{\partial t} + \phi S_o\rho_o c_o\frac{\partial p_o}{\partial t} + \nabla\cdot(\rho_o\boldsymbol{v_o}) + \phi S_o\rho_o\frac{\partial \varepsilon_v}{\partial t} = \rho_o q_o. \tag{2.25}$$

Rearranging the terms, Eqs. 2.24 and 2.25 become

$$\left(S_w\rho_w\frac{b-\phi}{K_s} + \phi S_w\rho_w c_w\right)\frac{\partial p_w}{\partial t} + \rho_w\phi\frac{\partial S_w}{\partial t} + S_w\rho_w b\frac{\partial \varepsilon_v}{\partial t} + \nabla\cdot(\rho_w\boldsymbol{v_w}) = \rho_w q_w, \tag{2.26}$$

$$\left(S_o\rho_o\frac{b-\phi}{K_s} + \phi S_o\rho_o c_o\right)\frac{\partial p_o}{\partial t} + \rho_o\phi\frac{\partial S_o}{\partial t} + S_o\rho_o b\frac{\partial \varepsilon_v}{\partial t} + \nabla\cdot(\rho_o\boldsymbol{v_o}) = \rho_o q_o. \tag{2.27}$$

Dividing the density terms in Eqs. 2.26 and 2.27, adding the two equations, and using $S_w + S_o = 1$, one can get

$$\left(\frac{b-\phi}{K_s} + \phi S_w c_w + \phi S_o c_o\right)\frac{\partial p_w}{\partial t} + b\frac{\partial \varepsilon_v}{\partial t} + \nabla\cdot(\boldsymbol{v_o} + \boldsymbol{v_w}) = q_o + q_w, \tag{2.28}$$

which is the governing equation for pressure.

Note that the total velocity $\boldsymbol{v_t} = \boldsymbol{v_o} + \boldsymbol{v_w}$ or

$$\boldsymbol{v_t} = -(\frac{\boldsymbol{k}k_{rw}}{\mu_w} + \frac{\boldsymbol{k}k_{ro}}{\mu_o})\nabla p \tag{2.29}$$

can be used to express the water velocity term if water and oil mobility values (λ_w and λ_o) are given:

$$\boldsymbol{v_w} = \frac{\lambda_w}{\lambda_w+\lambda_o}\boldsymbol{v_t}, \tag{2.30}$$

where $\frac{\lambda_w}{\lambda_w+\lambda_o}$ is also written as F_w, the fractional flow of water.

Thus, Eq. 2.26 can be rewritten for the governing equation for water saturation as

$$\left(S_w\frac{b-\phi}{K_s} + \phi S_w c_w\right)\frac{\partial p_w}{\partial t} + \phi\frac{\partial S_w}{\partial t} + S_w b\frac{\partial \varepsilon_v}{\partial t} + \nabla\cdot\left(\frac{\lambda_w}{\lambda_w+\lambda_o}\boldsymbol{v_t}\right) = q_w. \tag{2.31}$$

The governing equation of the geomechanics problem in this study considers momentum balance based on the quasi-static assumption (Hughes 1987) as

$$\nabla\cdot\boldsymbol{\sigma} = 0, \tag{2.32}$$

where $\boldsymbol{\sigma}$ is the total stress tensor (Cauchy stress tensor). The sign convention in this study is that compressive stress is negative. The total stress is also expressed as

$$\boldsymbol{\sigma} = \boldsymbol{\sigma}_0 - b(p-p_0)\mathbf{1} + C_{dr}:\varepsilon, \tag{2.33}$$

where $\boldsymbol{\sigma}_0$ is the initial total stress, p_0 is the initial pressure, $\mathbf{1}$ is the second order identity tensor, C_{dr} is the fourth order stiffness tensor, ε is the strain tensor. $C_{dr}:\varepsilon$ represents the effective stress. The strain tensor ε follows the assumption of infinitesimal transformation. It is the symmetric gradient of displacement as

$$\varepsilon = \nabla^s\boldsymbol{u} = \frac{1}{2}(\nabla^T\boldsymbol{u} + \nabla\boldsymbol{u}), \tag{2.34}$$

where ∇^s is the symmetric gradient operator.

Thus, the four governing equations for the fully coupled flow and geomechanics problem are obtained as

$$\left(\frac{b-\phi}{K_s} + \phi S_w c_w + \phi S_o c_o\right)\frac{\partial p_w}{\partial t} + b\frac{\partial \varepsilon_v}{\partial t} + \nabla \cdot (\boldsymbol{v_o} + \boldsymbol{v_w}) = q_o + q_w, \tag{2.35}$$

$$\boldsymbol{v_t} = -(\frac{\boldsymbol{k}k_{rw}}{\mu_w} + \frac{\boldsymbol{k}k_{ro}}{\mu_o})\nabla p, \tag{2.36}$$

$$\left(S_w\frac{b-\phi}{K_s} + \phi S_w c_w\right)\frac{\partial p_w}{\partial t} + \phi\frac{\partial S_w}{\partial t} + S_w b\frac{\partial \varepsilon_v}{\partial t} + \nabla \cdot \left(\frac{\lambda_w}{\lambda_w+\lambda_o}\boldsymbol{v_t}\right) = q_w, \tag{2.37}$$

$$\nabla \cdot \boldsymbol{\sigma} = 0. \tag{2.38}$$

It is noted that the rock compressibility term c_r in classic reservoir simulation is not used in this model, because the production-induced rock deformation is not denoted by a constant compressibility term and rock deformation based on consolidation theories and momentum balance as shown in Eq. 2.21 and Eq. 2.38 is considered in the coupled flow and geomechanics model.

2.1.2 Boundary Conditions

The boundary condition for the flow problem is Neumann boundary or no-flow boundary. It is written as

$$\boldsymbol{v_t} \cdot \boldsymbol{n} = 0 \text{ on } \Gamma, \tag{2.39}$$

where $\boldsymbol{n}$ is the outward unit normal vector and Γ is the boundary of the domain.

The boundary condition for the geomechanics has two types: constant traction and fixed displacement:

$$\boldsymbol{\sigma} \cdot \boldsymbol{n} = \boldsymbol{t} \text{ on } \Gamma_1, \tag{2.40}$$

$$\boldsymbol{u} \cdot \boldsymbol{n} = 0 \text{ on } \Gamma_2, \tag{2.41}$$

where Γ_1 is the geomechanical boundary with constant traction and Γ_2 is the geomechanical boundary with fixed displacement of zero. $\boldsymbol{t}$ is the boundary traction. $\Gamma_1 \cap \Gamma_2 = \emptyset$. A typical geomechanical boundary setup is shown in Figure 2.1.

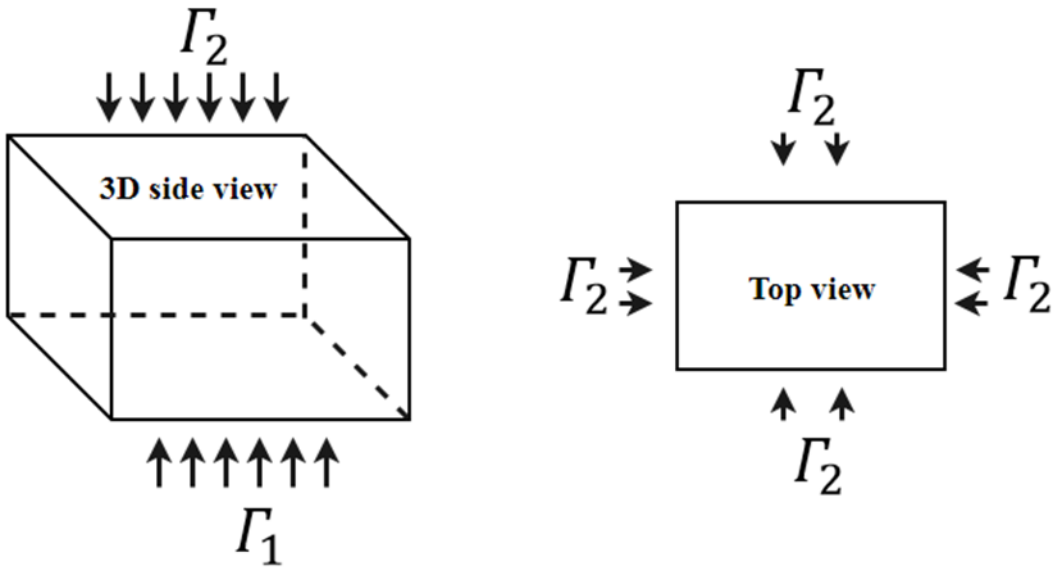

Figure 2.1. A typical setup for geomechanics boundary condition (reprinted with permission from Guo et al. 2018a)

Another boundary condition is the sink/source terms for water and oil phases. Two types of boundary conditions can be prescribed in this problem: constant rate and constant bottomhole pressure.

First, constant rates can be used at wells with constant water rate of q_w and constant oil rate as q_o. These terms are already in the governing equations and no further modification needs to be made.

Second, constant bottomhole pressure can be used at wells. Peaceman equation (1978) is used to relate bottomhole pressure with rates as

$$q_o = \frac{2\pi k k_{ro} h}{\mu_o B_o \ln\left(\frac{r_o}{r_w}\right)} (P_c - P_{wf}), \tag{2.42}$$

$$q_w = \frac{2\pi k k_{rw} h}{\mu_w B_w \ln\left(\frac{r_o}{r_w}\right)} (P_c - P_{wf}), \tag{2.43}$$

where h is the cell thickness, B_o is formation volume factor for oil, B_w is formation volume factor for water, r_w is the well radius, r_o is the effective grid-cell radius, P_{wf} is the bottomhole pressure, and P_c is the grid block pressure which is equal to fluid pressure in the specific cell.

2.1.3 Initial Conditions

Initial conditions are required for fluid flow, saturation, and stress. At time zero, they are expressed as

$$p = p_0, \tag{2.44}$$

$$S_w = S_{w0}, \tag{2.45}$$

$$\boldsymbol{\sigma} = \boldsymbol{\sigma}_0. \tag{2.46}$$

2.1.4 Numerical Solution

Finite element methods are used for the space discretization of the coupled problem. An open source finite element library DEAL.II is used for the space discretization (Bangerth et al. 2007; Yang 2013).

Four test functions $(\psi, \chi, \omega, \varphi)$ are used to write the weak forms of the governing equation system (Eqs. 2.35-2.38). The numerical solutions for pressure p, water saturation S_w, velocity $\boldsymbol{v}$, and displacement $\boldsymbol{u}$ are p_h, S_{wh}, $\boldsymbol{v}_h$, and $\boldsymbol{u}_h$. For the discretized system, the numerical solutions are solved in the space $DG \times CG \times RT \times CG$ where DG is discontinuous Galerkin, CG is continuous Galerkin, and RT is Raviart-Thomas.

The weak forms are obtained as follow

$$\left(\omega, \frac{1}{(\lambda_o+\lambda_w)k}\boldsymbol{v}_t^{n+1}\right)_\Omega - (\nabla\cdot\omega, p^{n+1})_\Omega = 0, \tag{2.47}$$

$$(-\varepsilon(\varphi), \boldsymbol{\sigma}_0)_\Omega - 2\left(\varepsilon(\varphi), \mu\varepsilon(\boldsymbol{u}^{n+1})\right)_\Omega - \left(\lambda(\nabla\cdot\varphi), (\nabla\cdot\boldsymbol{u}^{n+1})\right)_\Omega + \left(\nabla\cdot\varphi, b(p^{n+1}-p_0)\right)_\Omega = -(\varphi, \boldsymbol{t})_\Gamma, \tag{2.48}$$

$$\left(\psi, \left(\frac{b-\emptyset}{K_s} + S_w^{n+1}\emptyset c_w + (1-S_w^{n+1})\emptyset c_o\right)\frac{p^{n+1}-p^n}{\Delta t}\right)_\Omega + \left(\psi, b\frac{\varepsilon_v^{n+1}-\varepsilon_v^n}{\Delta t}\right)_\Omega + (\psi, \nabla\cdot v_t^{n+1})_\Omega = (\psi, q_o+q_w)_\Omega, \tag{2.49}$$

$$\left(\chi, S_w^{n+1}\left(\frac{b-\emptyset}{K_s}+\emptyset c_w\right)\frac{p^{n+1}-p^n}{\Delta t} + \emptyset\frac{S_w^{n+1}-S_w^n}{\Delta t} + s_w^{n+1}b\frac{\varepsilon_v^{n+1}-\varepsilon_v^n}{\Delta t}\right)_\Omega + (\nabla\chi, (\nabla S_w^{n+1} - F_w v_t^{n+1}))_\Omega + (\upsilon_a\nabla\chi, \nabla S_w^{n+1})_\Omega = (\chi, q_w)_\Omega\,, \tag{2.50}$$

where $(a,b)_\Omega = \int_\Omega ab$ and $(a,b)_\Gamma = \int_\Gamma ab$.

In Eq. 2.49, a stabilization term υ_a is used for the continuous Galerkin method for saturation solution. This term uses a piecewise constant artificial viscosity to improve the

stability in the solution. According to Chueh et al. (2010), this stabilization inhibits the oscillation if there are strong saturation gradients. The artificial viscosity term is expressed as

$$v_a|_k = \beta \|v_t\|_{L^\infty(k)} \times h_k, \tag{2.51}$$

where β is the dimensionless stabilization constant, h_k is the cell diameter, and $\|v_t\|_{L^\infty(k)}$ is the infinity norm of the local cell's velocity.

Backward Euler method is used for the implicit time stepping in the numerical solution. Newton-Raphson method is used for the iterations. At time step n and at Newton iteration k, the Jacobian matrix can be expressed as

$$\begin{bmatrix} \frac{\partial R^{\boldsymbol{v_t}}}{\partial \boldsymbol{v_t}} & \frac{\partial R^{\boldsymbol{v_t}}}{\partial p} & \frac{\partial R^{\boldsymbol{v_t}}}{\partial S_w} & \frac{\partial R^{\boldsymbol{v_t}}}{\partial \boldsymbol{u}} \\ \frac{\partial R^{p}}{\partial \boldsymbol{v_t}} & \frac{\partial R^{p}}{\partial p} & \frac{\partial R^{p}}{\partial S_w} & \frac{\partial R^{p}}{\partial \boldsymbol{u}} \\ \frac{\partial R^{S_w}}{\partial \boldsymbol{v_t}} & \frac{\partial R^{S_w}}{\partial p} & \frac{\partial R^{S_w}}{\partial S_w} & \frac{\partial R^{S_w}}{\partial \boldsymbol{u}} \\ 0 & \frac{\partial R^{\boldsymbol{u}}}{\partial p} & \frac{\partial R^{\boldsymbol{u}}}{\partial S_w} & \frac{\partial R^{\boldsymbol{u}}}{\partial \boldsymbol{u}} \end{bmatrix}^{n+1,k} \begin{bmatrix} \delta \boldsymbol{v_t}^{n+1} \\ \delta p^{n+1} \\ \delta S_w^{n+1} \\ \delta \boldsymbol{u}^{\boldsymbol{n+1}} \end{bmatrix}^k = \begin{bmatrix} R^{\boldsymbol{v_t},n+1} \\ R^{p,n+1} \\ R^{S_w,n+1} \\ R^{\boldsymbol{u},n+1} \end{bmatrix}^k \tag{2.52}$$

where R is the residual (Yang 2013).

After the displacement solution is obtained through the model, displacement is converted to stress through the elasticity correlations:

$$\begin{gathered} \varepsilon_{xx} = \frac{\partial u_x}{\partial x}, \varepsilon_{yy} = \frac{\partial u_y}{\partial y}, \varepsilon_{zz} = \frac{\partial u_z}{\partial z}, \\ \gamma_{xy} = \frac{\partial u_x}{\partial y} + \frac{\partial u_y}{\partial x}, \gamma_{yz} = \frac{\partial u_y}{\partial z} + \frac{\partial u_z}{\partial y}, \gamma_{zx} = \frac{\partial u_z}{\partial x} + \frac{\partial u_x}{\partial z} \end{gathered} \tag{2.53}$$

$$\begin{bmatrix}\sigma_{xx}\\ \sigma_{yy}\\ \sigma_{zz}\\ \tau_{xy}\\ \tau_{yz}\\ \tau_{zx}\end{bmatrix} = \begin{bmatrix} \lambda\frac{1-\nu}{\nu} & \lambda & \lambda & 0 & 0 & 0 \\ \lambda & \lambda\frac{1-\nu}{\nu} & \lambda & 0 & 0 & 0 \\ \lambda & \lambda & \lambda\frac{1-\nu}{\nu} & 0 & 0 & 0 \\ 0 & 0 & 0 & G & 0 & 0 \\ 0 & 0 & 0 & 0 & G & 0 \\ 0 & 0 & 0 & 0 & 0 & G \end{bmatrix} \begin{bmatrix}\varepsilon_{xx}\\ \varepsilon_{yy}\\ \varepsilon_{zz}\\ \gamma_{xy}\\ \gamma_{yz}\\ \gamma_{zx}\end{bmatrix} \tag{2.54}$$

where γ is the shear strain, τ is shear stress, λ is the first Lame parameter expressed as $\lambda = \frac{E\nu}{(1+\nu)(1-2\nu)}$, ν is the Poisson's ratio, E is Young's modulus, G is shear modulus. σ_{xx}, σ_{yy}, and σ_{zz} are components of effective stresses.

2.1.5 Model Validation

The model is validated with two analytical problems: Mandel's problem (Mandel 1953; Abousleiman et al. 1996) and McNamee-Gibson's problem (McNamee and Gibson 1960a; McNamee and Gibson 1960b). Consolidation is considered in these problems. They are often used to validate the numerical solutions from coupled flow and geomechanics simulations.

The model is first validated with Mandel's problem. Figure 2.2 shows the setup of the problem. In this 2D problem, a uniformly distributed force F is exerted on the top. The porous media are initially saturated with fluid. The porous media are considered as poroelastic materials. The left and bottom boundaries are no flow boundaries with fixed zero displacement. The right boundary is a stress free and drainage boundary. Once the force is exerted at the beginning, the rock consolidation leads to a sudden increase of pressure within the domain. Then, due to the fluid depletion at the drainage boundary, the

pressure within the domain gradually decreases. The inputs for the calculation are in Table 2.1. The detailed analytical solution of pressure is provided in Verruijt (2013).

The matching results are in Figure 2.3. In the matching, two dimensionless parameters, normalized pressure p_d and dimensionless time t_d, are used. They are expressed as

$$p_d = \frac{p - p_{init}}{p_1 - p_{init}}, \tag{2.55}$$

$$t_d = \frac{t c_v}{L_f^2}, \tag{2.56}$$

$$c_v = \frac{k}{\mu_f (\frac{1}{K_{dr}} + \phi c_f)}, \tag{2.57}$$

where p_1 is the pressure at the monitoring point at the first time step, p_{init} is the initial pressure within the domain, c_v is the consolidation coefficient, L_f is the vertical distance of the point, μ_f is fluid viscosity, c_f is fluid compressibility, and K_{dr} is drained modulus.

The initial increase of pressure at the monitoring point is captured, and the maximum p_d is obtained. After that, pressure monotonically decreases due to the effect of the drainage boundary. When the dimensionless time increases to one, the normalized pressure is already decreased to 20% of the initial value.

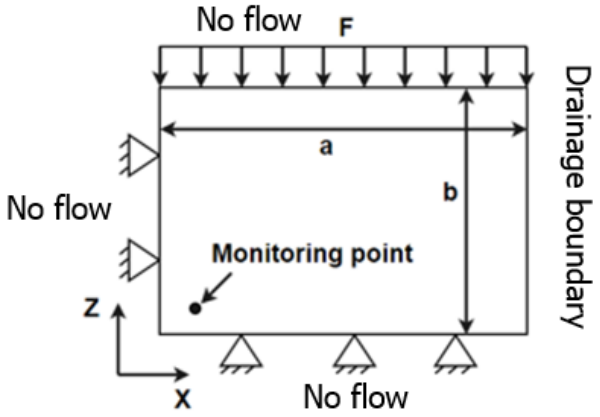

Figure 2.2. Mandel's problem (reprinted with permission from Guo et al. 2018b)

Parameter	**Value**
Dimension a, m	20
Dimension b, m	10
X location of the monitoring point, m	0.1
Z location of the monitoring point, m	0.1
Initial pressure, MPa	8
Young's modulus, GPa	20
Poisson's ratio	0
Porosity	0.2
Fluid viscosity, Pa·s	2×10^{-3}
Permeability, m^2	2×10^{-15}
F, MPa	50
Density of fluid, kg/m^3	1000

Table 2.1. Inputs for Mandel's problem (reprinted with permission from Guo et al. 2018b)

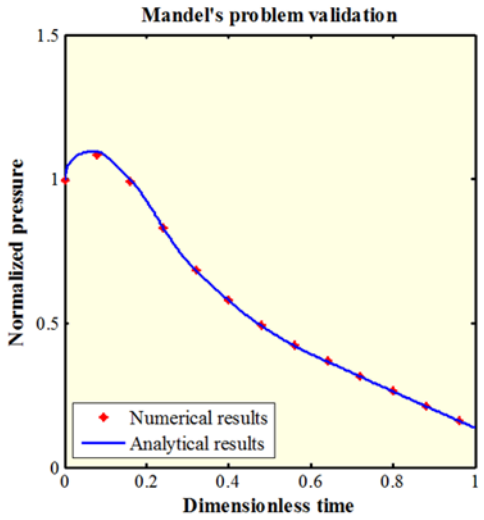

Figure 2.3. Matching with Mandel's problem (reprinted with permission from Guo et al. 2018b)

The model is then validated with McNamee-Gibson's problem. It provides another analytical solution to a 2D consolidation problem. The Mandel-Cryer effect is presented in this problem. In McNamee-Gibson's problem, a semi-infinite domain is involved. Uniform forces are exerted on the top of the domain for a certain length. The setup of this problem is shown in Figure 2.4. The left, right, and bottom boundaries are drainage boundaries which allow for fluid depletion. These three boundaries are also fixed displacement boundaries. No flow boundary is prescribed at the top of the 2D plane, with two uniformly distributed forces applied. A monitoring point is selected to present the initial increase of pressure due to the Mandel-Cryer effect. Inputs for this problem are recorded in Table 2.2.

The matching between the analytical solution and the numerical results is shown in Figure 2.5. Like in Mandel's problem, dimensionless parameters of normalized pressure p_d and dimensionless time t_d are used in the matching. The initial increase of pressure at the monitoring point is captured for $t_d < 0.3$, which describes the Mandel-Cryer effect. When $t_d > 0.3$, the pressure at the monitoring point drops below the initial value. It keeps decreasing due to the drainage boundary.

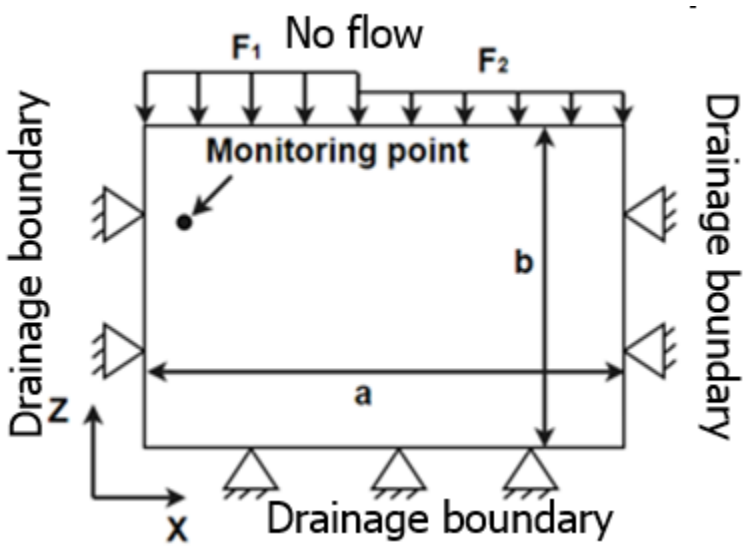

Figure 2.4. McNamee-Gibson's problem (reprinted with permission from Guo et al. 2018b)

Parameter	Value
Dimension a, m	20
Dimension b, m	20
X location of the monitoring point, m	0.1
Z location of the monitoring point, m	16
Initial pressure, MPa	10
Young's modulus, GPa	0.45
Poisson's ratio	0
Porosity	0.25
Fluid viscosity, Pa·s	1×10^{-3}
Permeability, m^2	4.9×10^{-14}
F_1, MPa	20
F_2, MPa	10
Density of fluid, kg/m^3	1000

Table 2.2. Inputs for McNamee-Gibson's problem (reprinted with permission from Guo et al. 2018b)

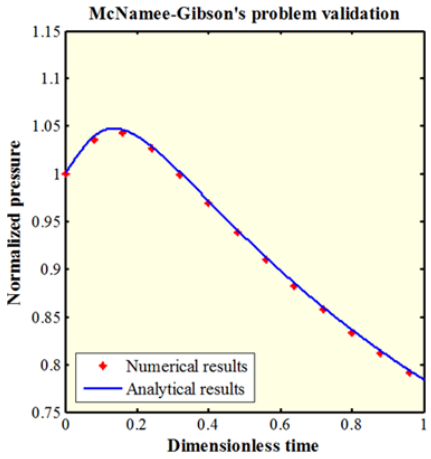

Figure 2.5. Matching with McNamee-Gibson's problem (reprinted with permission from Guo et al. 2018b)

2.1.6 Conclusion

In summary, a fully coupled flow and geomechanics model is presented. Two-phase black oil and linear elasticity are considered in the model. Finite element methods are used for the space discretization in 3D. Backward Euler is used for time stepping. Newton-Raphson is used for iterations. The model is then validated with two analytical solutions: Mandel's problem and McNamee-Gibson's problem. This model is used in the studies presented in Sections 3-5.

2.2 Parallelization with parallel solver

In Section 2.2, a standalone parallelized sequentially coupled flow and geomechanics model is presented. The parallel model in this section is developed based on an existing TOUGH serial code coupling single phase fluid-heat flow and elastoplasticity (Pruess 1999; Kim et al. 2014), and the parallelization is based on the application of a parallel solver PETSc (Balay et al. 2014). The combination of the two aforementioned packages forms the foundation of the parallelized coupled flow and geomechanics model. It is noted that this model is not related to the fully coupled model presented in the previous Section 2.1 and it is not related to the numerical results presented in Sections 3-5. Only results in Section 6 document the parallel performance of the parallelized coupled model presented in this subsection. It is also noted that there are several published parallelized versions of the TOUGH-based geomechanics models (e.g., TOUGH-CSM, TOUGHREACT-ROCHMECH) using various sophisticated

parallelization schemes which enable the massive parallel processing on clusters (Rutqvist 2017).

A portable parallelization scheme is introduced in this subsection. Before the parallelization, a second coupled flow and geomechanics model is presented. Unlike the fully coupled model in Section 2.1, this model involves sequential coupling. The coupling is made between the flow problem and the geomechanics problem. Thus, once the portable parallelization scheme for the sequentially coupled model is established, the scheme can be ported to serial codes with similar modular structures considering various complex physical effects.

Specifically, non-isothermal fluid-heat flow is coupled with elastoplastic geomechanics. Therefore, the simulator solves for the temporal and spatial evolutions of pressure, temperature, and displacement. The sequential coupling method is fixed-stress as proposed in Kim et al. (2009). The serial simulator is developed based on the fortran-based TOUGH+family codes (Pruess 1999; Kim et al. 2014).

2.2.1 Sequentially Coupled Model

In the coupled model solved by sequential methods, the fluid-heat flow problem and the geomechanics problem are solved separately in two different linear systems. Pressure and temperature are first solved in one time step. After that, they are used along with the stress solution in the sequential coupling to update the coupled system.

Mass conservation is used for the fluid flow equation (Pruess et al. 1999):

$$\frac{d}{dt}\int_{\Omega} m_f d\Omega + \int_{\Gamma} \mathbf{f}_f \cdot \mathbf{n}\, d\Omega = \int_{\Omega} q_f d\Omega, \tag{2.58}$$

where f represents the fluid flow, m_f is the mass flow (accumulation), $\mathbf{f}_f$ is the mass flux term for the fluid flow, q_f is the sink/source for fluid flow, Ω is the domain, and Γ is the boundary. The mass flux for fluid flow $\mathbf{f}_f$ can be further expressed by Darcy's law as

$$\mathbf{f}_f = -\rho_f \frac{\boldsymbol{k}}{\mu_f}(\nabla p_f - \rho_f \mathbf{g}), \tag{2.59}$$

where ρ_f is the fluid density, μ_f is the fluid viscosity, and $\mathbf{g}$ is the second order gravity tensor.

Energy conservation is used for the heat flow equation:

$$\frac{d}{dt}\int_{\Omega} m^H d\Omega + \int_{\Gamma} \mathbf{f}^H \cdot \mathbf{n}\, d\Omega = \int_{\Omega} q^H d\Omega, \tag{2.60}$$

where H represents heat, m^H is the heat flow (accumulation), $\mathbf{f}^H$ is the heat flux, and q^H is the sink/source term for heat. Heat accumulation m^H can be written as

$$m^H = (1-\phi)\int_{T_0}^{T} \rho_R C_R dT + \phi \rho_f e_f, \tag{2.61}$$

where T is the temperature of rock, T_0 is the reference temperature, ρ_R is the density of rock, C_R is the heat capacity of rock, and e_f is the specific internal energy of fluid.

Heat flux $\mathbf{f}^H$ can be further expressed as

$$\mathbf{f}^H = -\mathbf{K}_H \nabla T + h_f \mathbf{w}_f, \tag{2.62}$$

where $\mathbf{K}_H$ is the second order composite thermal conductivity tensor, h_f is the specific enthalpy of the fluid, and $\mathbf{w}_f$ is the mass flux.

Momentum balance (Hughes 1987) is used for the governing equation of geomechanics. The quasi-static assumption is used in the formulation.

$$\nabla \cdot \boldsymbol{\sigma} + \rho_b \mathbf{g} = 0, \tag{2.63}$$

where ρ_b is the bulk density. Similar to the model presented in Section 2.1, the infinitesimal transformation assumption is used as

$$\varepsilon = \nabla^s \boldsymbol{u} = \frac{1}{2}(\nabla^T \boldsymbol{u} + \nabla \boldsymbol{u}), \tag{2.64}$$

Based on Biot (1941) and Coussy (1995), the constitutive relations for the coupling of fluid-heat flow and elastoplasticity are established as follow

$$\delta \boldsymbol{\sigma} = \overbrace{\mathbf{C}_{dr} \delta \boldsymbol{\varepsilon}}^{\delta \boldsymbol{\sigma}'} - \alpha_f \delta p_f 1 - 3\alpha_{\mathrm{T}} K_{dr} \delta T \mathbf{1}, \tag{2.65}$$

$$\frac{\delta m_f}{\rho_f} = \alpha_f \delta \varepsilon_v + \frac{1}{M_f} \delta p_f - 3\alpha_{m,f} \delta T, \tag{2.66}$$

$$\delta \bar{S} = \bar{s}_f \delta m_f + 3\alpha_T K_{dr} \delta \varepsilon_v - 3\alpha_{m,f} \delta p_f + \frac{C_d}{T} \delta T, \tag{2.67}$$

where δ represents the change caused by solid deformation, $\delta \boldsymbol{\sigma}'$ is the effective stress in incremental form, $\mathbf{1}$ is a second order identity tensor, $3\alpha_{\mathrm{T}}$ is the volumetric skeleton thermal dilation coefficient. $3\alpha_{m,f}$ is further written as $3\alpha_{m,f} = 3\alpha_\phi + \phi 3\alpha_f$, where $3\alpha_\phi$ is the thermal dilation coefficient for porosity, and $\phi 3\alpha_f$ is the thermal dilation coefficient for fluid. C_d is the total volumetric heat capacity. C_d is further written as $C_d = C_R + m_f C_{p,f}$, where $C_{p,f}$ is the fluid volumetric specific heat capacity at constant pressure. $\bar{s}_f$ is the specific entropy of fluid.

In this context of thermos-poro-mechanics multiway coupling, the Biot's coefficient is also written as α_f and the Biot modulus is written as M_f. They are also expressed as

$$\alpha_f = 1 - \frac{K_{dr}}{K_s}, \tag{2.68}$$

$$\frac{1}{M_f} = \phi c_f + \frac{\alpha_f - \phi}{K_s}, \tag{2.69}$$

where K_s is the solid grain bulk modulus.

Shear failure is taken into account using the Mohr-Coulomb model (Zoback 2007). This model is often used for the modeling of failure in cohesive frictional materials. The equations are as

$$f = \tau'_m - \sigma'_m \sin\Psi_f - c_h \cos\Psi_f \leq 0, \tag{2.70}$$

$$\mathrm{g} = \tau'_m - \sigma'_m \sin\Psi_d - c_h \cos\Psi_d \leq 0, \tag{2.71}$$

$$\sigma'_m = \frac{\sigma'_1 + \sigma'_3}{2}, \tag{2.72}$$

$$\tau'_m = \frac{\sigma'_1 - \sigma'_3}{2}, \tag{2.73}$$

where σ'_1 is the maximum principal effective stress, σ'_3 is the minimum principal effective stress, c_h is the cohesion, Ψ_f is the friction angle, Ψ_d is the dilation angle, f is the yield function, and g is the plastic potential function.

After the mathematical formulations for the fluid-heat flow and elastoplasticity problems are presented, the numerical solution is then introduced. In the elastoplasticity problem, the space discretization is achieved using the nodal-based finite element method (Hughes 1987). In the fluid-heat flow problem, the space discretization is achieved using the finite volume method (Aziz and Settari 1979). The fluid-heat flow module is based on TOUGH2 (Pruess 1999) and the geomechanics module is based on TOUGH-ROCMECH (Kim et al. 2014). Backward Euler is used for the implicit method in time stepping.

The sequential coupling is achieved using the fixed-stress method. Kim et al. (2011) proved that the fixed-stress method can lead to good stability, efficiency, and accuracy in

the numerical solution, and this method results in solutions comparable to the fully coupled method. In this sequential strategy, at each time step, the flow problem is first solved. When the flow problem is being solved, the stress in the geomechanics problem is fixed. Geomechanics is then solved based on the updated flow solutions. Lagrange porosity and its correction are used for the implementation of the fixed-stress method in the model as

$$\Phi^{n+1} - \Phi^n = \underbrace{\left(\frac{\alpha_f^2}{K_{dr}} + \frac{\alpha_f - \Phi^n}{K_s}\right)}_{\Phi^n c_p}\left(p_f^{n+1} - p_f^n\right) + 3\alpha_T \alpha_f (T^{n+1} - T^n) + \underbrace{\frac{\alpha_f}{K_{dr}}(\sigma_v^n - \sigma_v^{n-1})}_{\Delta\Phi}, \tag{2.74}$$

where n is the time step, c_p is the pore compressibility (Settari and Mourtis 1998), σ_v is the total volumetric mean stress.

For the accuracy and stability of sequential coupling methods compared to fully coupled methods, Dean et al. (2006) pointed out that if a tight tolerance is used in the coupling process, explicit coupling, iterative coupling, and full coupling yield very similar simulation results for the nonlinear iterations in the coupled flow and geomechanics problem. This observation is honored in the fixed-stress coupling process in the coupled model in this subsection.

2.2.2 Parallel Solver

Parallel matrix assembly and parallel matrix solution are used to solve the linear systems in the aforementioned coupled model. Both MPI and OpenMP memory

architectures are used in the parallelization. The MPI-based parallelization is achieved by the open-source package PETSc (Balay et al. 2014) which provides numerical solutions with high performance computing capacities. The OpenMP-based parallelization is used for DO loops that are highly localized without data communication between adjacent cells. The use of the distributed memory architecture of MPI improves the computational efficiency for large-scale problems, and the use of the shared memory architecture of OpenMP reduces overheads for subroutines that have DO loops with simple structures.

In 3D structured meshes, using Newton-Raphson method, the Jacobian matrix for the flow problem has seven banded diagonals of non-zero elements, while the stiffness matrix for the geomechanics problem usually has more banded diagonals with non-zero elements. In problems with millions of cells, the corresponding matrices lead to significant computational loads. This motivates the use of the parallel solver for better computational efficiency. Figure 2.6 presents the parallelization using the MPI-based PETSc package in the sequentially coupled model. As indicated in the figure, the code re-development effort is reduced considering the parallelization of a serial code: MPI is only involved in the parallel matrix assembly and in matrix solution. The Jacobian matrices have the format of CRS (compressed row storage). Note that array operations can significantly increase the matrix assembly efficiency and the sparse format can lead to good efficiency.

Two segments of pseudo-codes are provided to describe the parallel matrix operations. Table 2.3 shows the pseudo-code for parallel matrix assembly. In each process, local non-zero elements are assigned to matrices and vectors through iterations. Table 2.4 shows the pseudo-code for the PETSc function calls. Matrices and vectors are first created

in the parallel environment. Then, the Krylov space solver with preconditioning is used for matrix solution.

OpenMP (Dagum and Menon 1998) is then used in local DO loops for the speedup of iterations. The loops include the parameter updating subroutine for sequential coupling as in Eq. 2.74, the subroutines for the generation of non-zero elements for the coefficient matrices in the flow problem and for the stiffness matrices in the geomechanics problem, subroutines calculating stresses and strains based on displacement solutions, and the localized plasticity updating subroutines after the elasticity stiffness matrix solution.

```
local element number = total element number / proc_number      ! assign local  elements


DO i = 1, local element number                                 ! at a certain process
    Assigning Jacobian_value(i)                                ! assign values to sparse matrix format
    Call PETSc assembly to assign values to parallel solver    ! feed values to parallel solver
END DO
```

Table 2.3. Pseudo-code for parallel matrix assembly (reprinted with permission from Guo et al. 2017)

Call MatCreate	! create coefficient matrix
Call MatSetSizes	! decompose the matrix in parallel
Assigning values to the created parallel matrix	! parallel assignment of matrix non-zero values
Call VecCreate	! create right hand side vector
Call VecSetSizes	! decompose the vector in parallel
Assigning right hand side vector values	! parallel assignment of right hand side values
Call KSPSolve	! invoke parallel solver to solve the system

Table 2.4. Pseudo-code for calling PETSc functions (reprinted with permission from Guo et al. 2017)

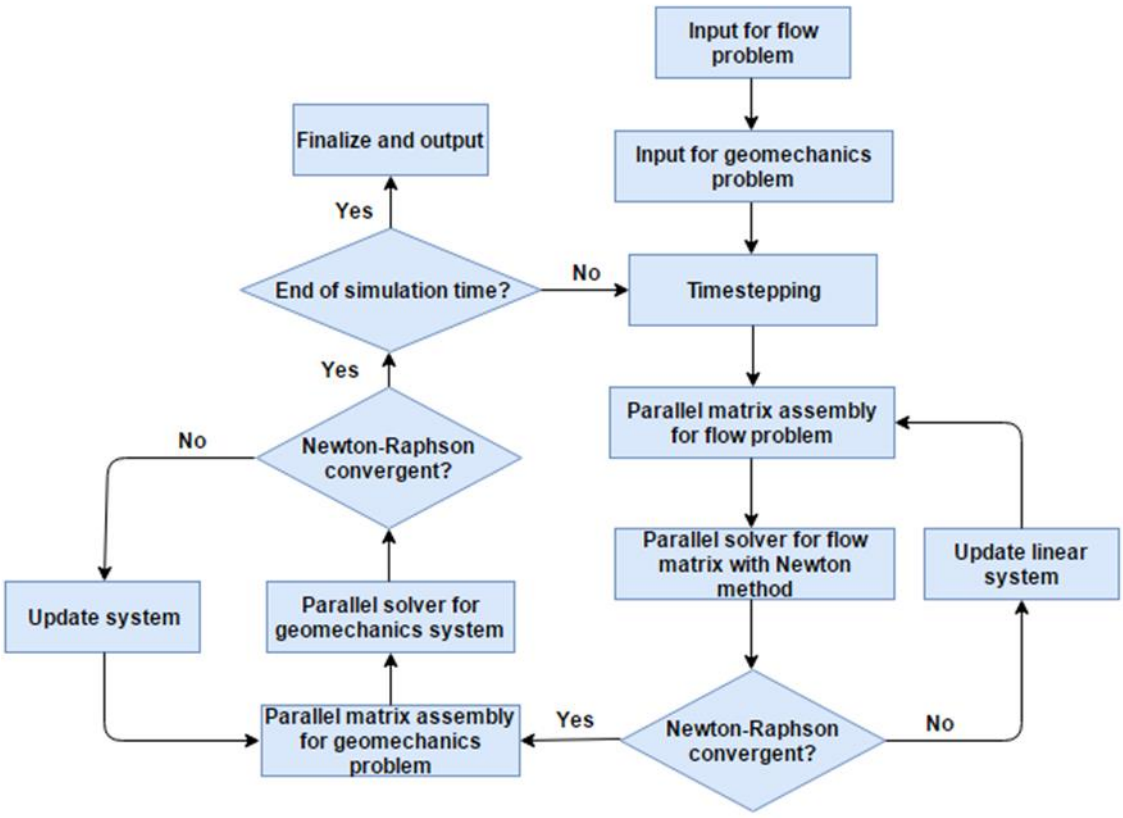

Figure 2.6. Parallelization of the sequentially coupled model (reprinted with permission from Guo et al. 2017)

2.2.3 Model Validation

The parallel simulator is validated with Terzaghi's problem and the details of the analytical solution are discussed in Verruijt (2013). This is a 1D consolidation problem where a constant overburden stress is exerted and two drainage boundaries for flow are prescribed. The sketch of the problem is shown in Figure 2.7. Due to the overburden stress, pressure increase can be observed during the initial stages. Then, pressure drops due to depletion at the drainage boundaries. Inputs for the problem are shown in Table 2.5. The matching results are in Figure 2.8. The dimensionless parameters are described in Eqs. 2.56-2.57, while h is the half length of the domain and z is the distance to the top. p/p_0 is the ratio of pressure at the current time to the initial pressure. The pressure increase due to consolidation is observed at t_d of 0.04 and t_d of 0.3. As dimensionless time further increases ($t_d = 4.6$), pressure is drained.

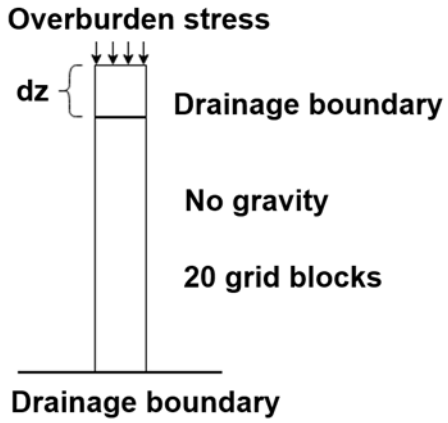

Figure 2.7. Terzaghi's problem setup (reprinted with permission from Guo et al. 2017)

Property	Value
Permeability	6.5×10^{-15} m^2
Porosity	0.43
Young's modulus	0.6 GPa
Rock density	2600 kg/m^3
Fluid density	728.3 kg/m^3
Fluid viscosity	8.632×10^{-4} $Pa \cdot s$
Boundary pressure	0 Pa
Overburden stress	20 MPa
Grid spacing	0.05 m

Table 2.5. Inputs for Terzaghi's problem (reprinted with permission from Guo et al. 2017)

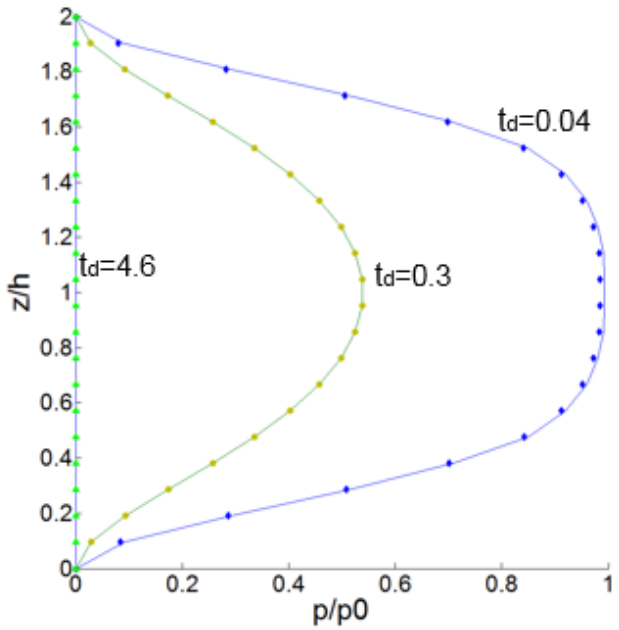

Figure 2.8. Numerical results validated with Terzaghi's problem (reprinted with permission from Guo et al. 2017)

2.2.4 Conclusion

A parallel simulator for sequentially coupled fluid-heat flow and elastoplastic geomechanics is presented in this subsection. A portable parallelization scheme is introduced which requires reduced code re-development efforts. This scheme can be used for sequentially coupled codes with similar modular structures. The parallelized simulator is validated with the analytical solution of Terzaghi's problem. The parallel performance obtained in case studies is profiled in Section 6.

3 WELL PERFORMANCE CONSIDERING GEOMECHANICS*

3.1 Introduction

Coupled flow and geomechanics modeling is first used to quantify geomechanical effects on hydrocarbon production. Thus, in the further analysis of production-induced stress state changes, the uncertainty introduced by incorporating geomechanics in the modeling can be understood. In this study, the fully coupled flow and geomechanics model presented in Section 2.1 is used.

This section incorporates full geomechanics with flow modeling for the understanding and characterization of reservoir performance and pressure characterization in a horizontal well completed by multi-fractures and the associated geomechanical effects.

*Part of this section is reprinted with permission from "Pressure Characteristics and Performance of Multi-Stage Fractured Horizontal Well in Shale Gas Reservoirs with Coupled Flow and Geomechanics" by X. Guo, H. Song, K. Wu, and J. Killough. Journal of Petroleum Science and Engineering, Copyright [2018] by Elsevier.

Field data from Barnett Shale are used. Specifically, the fluid is single phase gas. Unlike the slightly compressible fluid (e.g., water and oil), the compressibility of gas cannot be modeled by a constant compressibility term, and the real gas law should be used to model for the compressible gas. As a result, the governing equations for the model which consider two-phase fluid in Eqs. 2.35-2.38 are modified to single phase gas coupled to linear elasticity in this section as

$$\left(\frac{b-\phi}{K_s}+\emptyset\frac{M_g}{RT\rho_g}\left(\frac{1}{z_g}-\frac{p}{z_g^2}\frac{\partial z_g}{\partial p_g}\right)\right)\frac{\partial p_g}{\partial t}+b\frac{\partial \varepsilon_v}{\partial t}+\nabla\cdot\left(\boldsymbol{v_g}\right)=q_g, \tag{3.1}$$

$$\boldsymbol{v_g}=-\left(\frac{\boldsymbol{k}}{\mu_g}\right)\nabla p_g, \tag{3.2}$$

$$\nabla\cdot\boldsymbol{\sigma}=0, \tag{3.3}$$

where M_g is the molar mass of gas, R is the gas constant, ρ_g is gas density, z_g is the real gas factor, p_g is gas pressure, $\boldsymbol{v_g}$ is gas velocity, q_g is sink/source term for gas flow, and μ_g is gas viscosity.

3.2 Model Calibration

Reservoir, fluid, and production data from the literature (Miller et al. 2010; Song et al. 2015) are used for the construction of the reservoir model. The geomechanical inputs for the model are based on Vermylen (2011) and Zoback (2007). Hydraulic fractures are explicitly modeled by LGR (local grid refinement), where the size of the cells increase gradually as it moves away from hydraulic fractures to account for the sharp pressure gradient at and around highly permeable fractures (Yu and Sepehrnoori 2014).

From Zoback (2007), overburden and sideburden stresses can be calculated as

$$S_v = 23\ MPa/km\ \times\ D, \tag{3.4}$$

$$S_v > S_{Hmax} > S_{hmin}\ and\ S_{hmin} \geq 0.6S_v, \tag{3.5}$$

where S_v is the vertical stress, D is the depth in km, $23\ MPa/km$ is the estimated gradient of vertical stress, S_{Hmax} is the maximum horizontal stress, S_{hmin} is the minimum horizontal stress. In fact, Vermylen (2011) indicated that the extensional stress regime in Barnett Shale can be described by Eq. 3.5. In addition, given the depth, S_v is calculated to be 33 MPa. Side traction of 30 MPa is estimated for S_{Hmax} based on Eq. 3.5. Besides, in order to avoid fracturing of rock caused by pore pressure, S_{Hmax} and S_{hmin} should be greater than the pressure (initial pressure is 26.9 MPa in this case).

The focus in this study is the characteristics of pressure and production simulated by the fully coupled flow and geomechanics model, while the simulation and characterization of stress are not focused. Therefore, the uncertainty analysis of stress boundaries is not a key component of the study, and overburden and sideburden stresses are estimated with uncertainty. However, it is noted that stress analysis becomes very important in the analysis of in-situ stress evolutions. Altmann et al. (2014) indicated that in-situ stress state changes caused by production and injection are highly sensitive to stress regimes, where slight errors in stress estimation can lead to significant differences in the computation of production-induced and injection-induced stress changes.

A single horizontal well completed with six bi-wing hydraulic fractures is used for the modeling as shown in Figure 3.1. SRV (stimulated reservoir volume) is also used to account for the increased permeability around hydraulic fractures. History matching is also conducted to match for the reservoir gas rates as in Figure 3.2. Note that two sets of

numerical results (coupled model and decoupled model) are presented. Coupled model stands for the simulation results based on Eqs. 3.1-3.3, and decoupled model stands for the simulation results based on the fluid flow only model which excludes the terms accounting for geomechanics. Calibrated parameters for the reservoir model are recorded in Table 3.1.

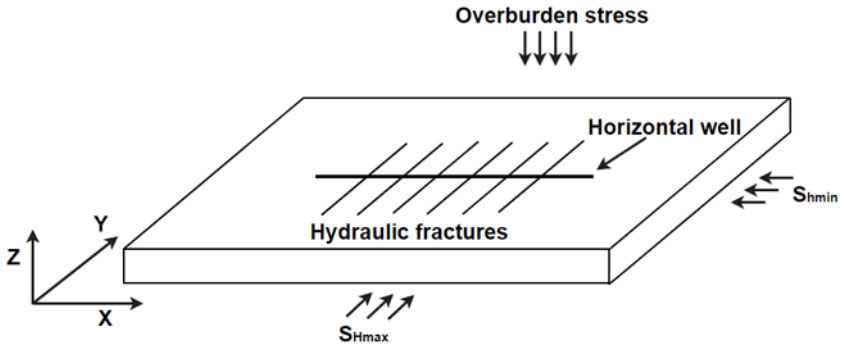

Figure 3.1. Reservoir model for the Barnett Shale gas production case (reprinted with permission from Guo et al. 2018a)

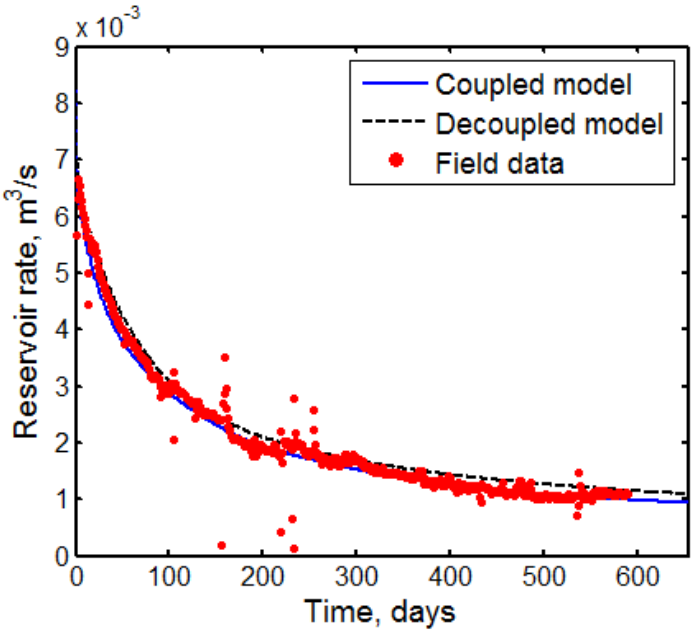

Figure 3.2. History match for gas production rates (reprinted with permission from Guo et al. 2018a)

Property	**Value**
Horizontal well length	456 m
Well location on y direction	500 m
Well location on x direction	522 – 978 m
SRV (stimulated reservoir volume) width	92 m
Porosity of SRV	0.03
Permeability of SRV	50 md (4.93×10^{-14} m^2)
Porosity of shale	0.1
Permeability of shale	1 md (9.87×10^{-16} m^2)
Pay zone height	25 m
Fracture half length	46 m
Number of fractures	6
Fracture stage spacing	73 m
Fracture conductivity	2.5 md-ft (0.75×10^{-15} m^2-m)
Biot's coefficient	1.0
Young's modulus	25 GPa
Poisson's ratio	0.22
Initial pressure	26.9 MPa
Bottom hole pressure	1.4 MPa
Side traction	30 MPa
Overburden traction	33 MPa

Table 3.1. Parameters for the Barnett Shale model (reprinted with permission from Guo et al. 2018a)

3.3 Parametric Study

Sensitivity analyses are then carried out based on the calibrated reservoir model for the parametric study. The base case is described by the parameters in Table 3.1. Pressure and gas production rates are analyzed. The parametric study is focused on several parameters including the coupling of geomechanics to fluid flow, rock elastic properties (Young's modulus, Biot's coefficient, and Poisson's ratio), and fracture geometry. It is noted that previous studies in the literature did not focus on the effect of fracture geometry in coupled flow and geomechanics modeling, while fracture geometry (spacing and half-length) is actually a key parameter in the development of unconventional reservoirs.

3.3.1 Coupling/Decoupling of Geomechanics with Flow

The general effect of coupling geomechanics to fluid flow on reservoir response and well performance is first investigated. Numerical results from the coupled simulation are compared with those from the decoupled simulation where only fluid flow is simulated. The flow problems in the two simulations are identical. Data in Table 3.1 are used for the simulations.

The simulated gas rates at reservoir condition are in Figure 3.3 and the corresponding cumulative production rates are in Figure 3.4. Figure 3.5 shows the pressure contours at and around the fractured reservoir volumes. Both results from the decoupled simulation and the coupled simulation are shown for comparison. Figure 3.6 plots the 1D pressure distribution along the horizontal well and along three hydraulic fractures on the

left. The pressure distributions along the three fractures on the right are not plotted due to symmetry.

In Figure 3.3 and Figure 3.4, production rates from the flow only simulation are lower than those from the coupled simulation. The difference in cumulative production increases with time. At the end of the simulation time of 653 days, there is a difference of 1.6×10^4 m^2 for the cumulative gas production.

In Figure 3.5, only pressure distributions around the most affected zones are shown. Pressure in areas outside the SRV does not experience significant change caused by the depletion in the well, as the shale matrix permeability is low. It is indicated that the pressure values at and around the six hydraulic fractures are lower in the coupled simulation result, and the shapes of pressure contours from the coupled simulation can better represent the geometry of the hydraulic fractures. In addition, this pressure comparison provides the reason why production from the decoupled simulation is higher than that from the coupled simulation: in Peaceman equation (Eq. 2.42), at a constant bottomhole pressure, a higher well cell pressure leads to a higher production rate. Here, decoupled simulation leads to higher well cell pressures, indicating a higher driving potential for production.

Figure 3.6 then shows the pressure differences along 1D lines. The pressure difference between coupled and decoupled simulation results is very small outside the SRV. This is explained by the insignificant fluid depletion in the low permeability zones. In contrast, greater differences are observed at and between the six producing intervals along the horizontal well. These intervals experience the greatest effects caused by fluid

flow, leading to significant production-induced geomechanical effects. Besides, based on pressure profiles along hydraulic fractures, it is indicated that as it moves from the leftmost fracture to the inner fractures, the difference between coupled and decoupled simulation results increases. Monitoring the pressure difference at the producing interval, it is found out that the difference is 0.308 MPa in the first fracture, 0.534 MPa in the second fracture, and 0.571 in the third fracture. This shows that the central stages of the horizontal well experience greater geomechanical effects than the two far ends of the well. It is also noticed that the pressure depletion is greater at the center of the well. Thus, it is proposed that the geomechanical effect on reservoir response is positively correlated with the magnitude of pressure depletion. For locations experiencing greater pressure depletion, they also experience greater strain and stress changes, which lead to greater pore volume changes. The increased pore volume changes then lead to greater pressure value changes.

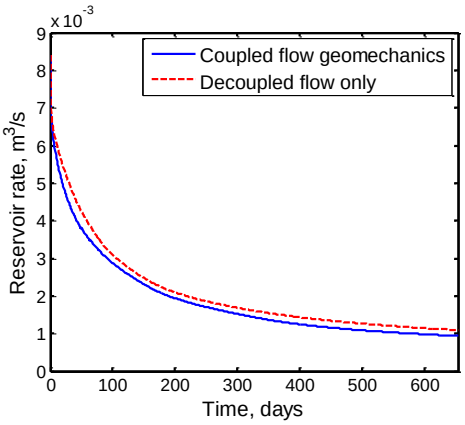

Figure 3.3. Gas rates at reservoir condition for coupled and decoupled simulations (reprinted with permission from Guo et al. 2018a)

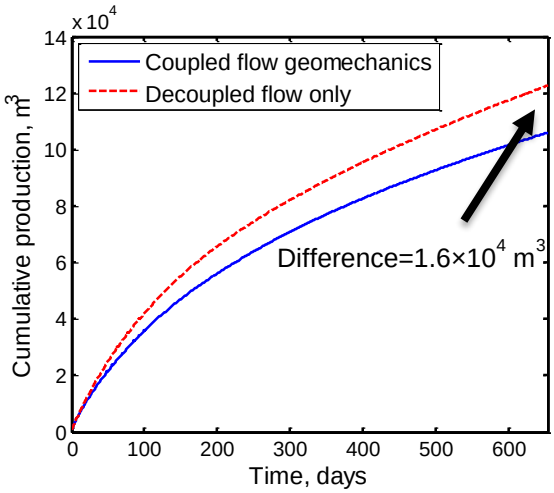

Figure 3.4. Cumulative rates at reservoir condition for coupled and decoupled simulations (reprinted with permission from Guo et al. 2018a)

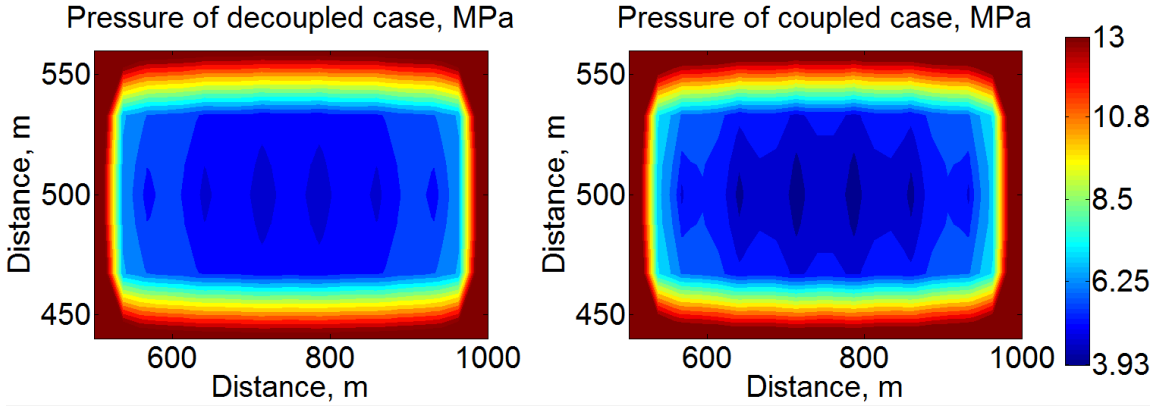

Figure 3.5. Pressure contours for the decoupled and coupled simulations at the end of the simulation (reprinted with permission from Guo et al. 2018a)

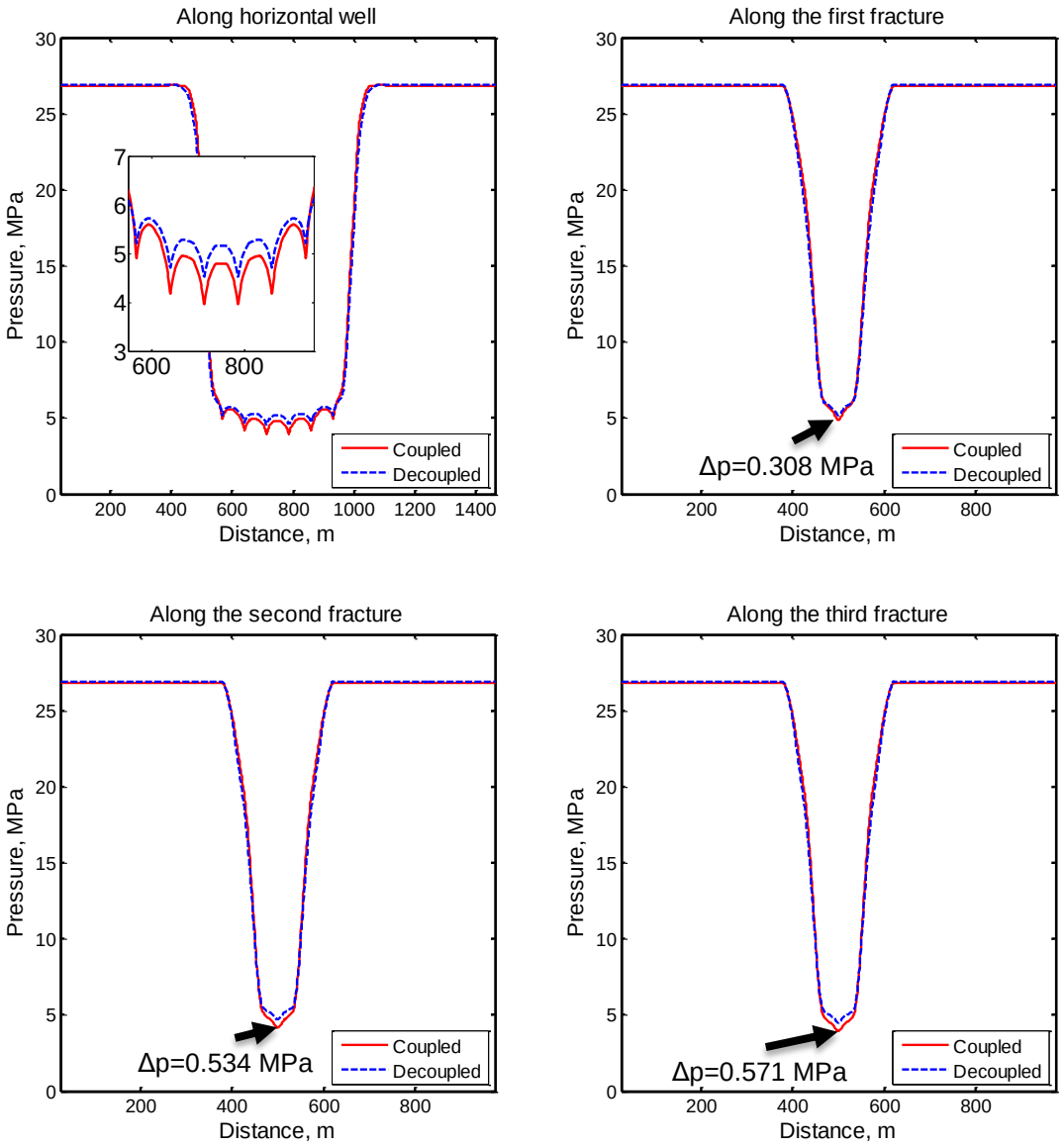

Figure 3.6. Pressure profiles along the well and fractures (reprinted with permission from Guo et al. 2018a)

3.3.2 Elastic Properties

Since geomechanics is considered in the coupled modeling, it is also important to investigate the effects of relevant elastic properties on reservoir response. Using the fully coupled model, effects of several parameters of Young's modulus, Biot's coefficient, and Poisson's ratio are studies.

Young's modulus E is first studied as it represents how pore volume deformation correlates with volumetric strain. In fact, the relationship between pore volume change and volumetric strain is physically represented by the bulk modulus. However, bulk modulus cannot be directly measured, which increases the difficulties using it for the sensitivity analysis. Besides, in linear elasticity, there simply exists a linear correlation between Young's modulus and bulk modulus via Poisson's ratio. Therefore, Young's modulus is used as the investigated parameter. Except for the E of 25 GPa in the base case, another three values of 20 GPa, 35 GPa, and 85 GPa are simulated for the sensitivity analysis.

Figure 3.7 and Figure 3.8 show that the gas rates and cumulative gas rates both decrease with the decrease of Young's modulus. The results from the decoupled simulation are also presented as a reference. Smaller Young's modulus essentially indicates reduced rock stiffness, which leads to more depletion-induced pressure changes caused by rock deformation. As Young's modulus increases, the stiffness also increases. The decoupled case actually represents the simulation with a large enough Young's modulus implying negligible depletion-induced rock deformation. Specifically, as shown in Eq. 3.1, the geomechanical terms $\frac{b-\phi}{K_s}$ and $b\frac{\partial \varepsilon_v}{\partial t}$ are approximately zero when Young's

modulus is essentially large, and the terms can be neglected, transforming the coupled pressure equation to the typical pressure equation describing flow diffusivity. Figure 3.8 provides a better description of the differences between cumulative productions. The differences increase with the increase of time. For the overall simulation time of 653 days, the cumulative production difference between the decoupled simulation and the coupled simulation using Young's modulus of 85 GPa is 0.48×10^4 m^3. The difference between the decoupled simulation and the coupled simulation using Young's modulus of 35 GPa increases to 1.04×10^4 m^3. As Young's modulus decreases to 25 GPa in the coupled simulation, the cumulative production difference increases to 1.60×10^4 m^3. As Young's modulus decreases further to 20 GPa in the coupled simulation, the cumulative production difference increases to 2.25×10^4 m^3.

Figure 3.9 presents pressure contours at the end of the simulation time for different Young's moduli. Lower pressure contours are observed in results with lower Young's moduli, especially at and around hydraulic fractures in the SRV regions. This is also explained by the greater pressure depletion caused by rocks with lower stiffness. The differences in areas outside the SRV are negligible as depletion is insignificant.

Figure 3.10 presents the comparison of 1D pressure distributions for various Young's modulus cases. Following the trend in Figure 3.9, lower Young's moduli lead to lower pressure profiles along the horizontal well. The six sudden decreases in pressure represent the locations of the producing intervals along the horizontal well. For the six producing intervals, the pressure difference between the case with the greatest Young's modulus and the case with the lowest Young's modulus is the minimum in the left most

hydraulic fracture, with the difference of 0.425 MPa. The difference increases to 0.737 MPa when it moves to the second hydraulic fracture. The maximum difference is observed at the third producing interval, with a value of 0.762 MPa. In addition, the difference of pressure is hardly observed in areas outside the SRV. This trend is in accordance with the observations made in Figure 3.6 that geomechanical effects on reservoir response are positively correlated with the magnitude of pressure depletion.

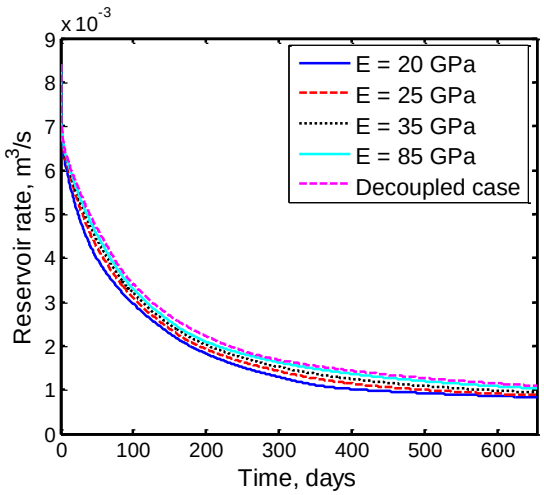

Figure 3.7. Gas rates with different Young's moduli (reprinted with permission from Guo et al. 2018a)

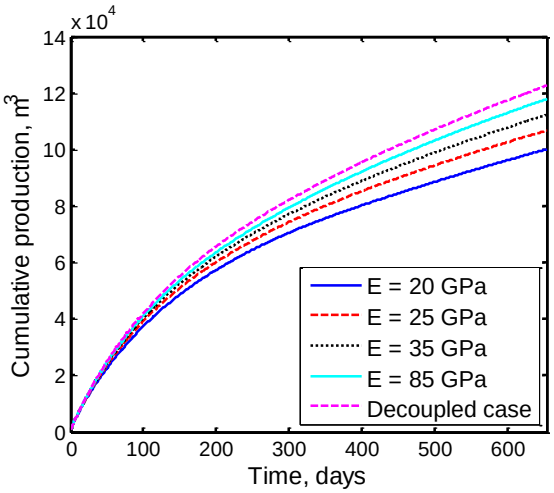

Figure 3.8. Cumulative gas production with different Young's moduli (reprinted with permission from Guo et al. 2018a)

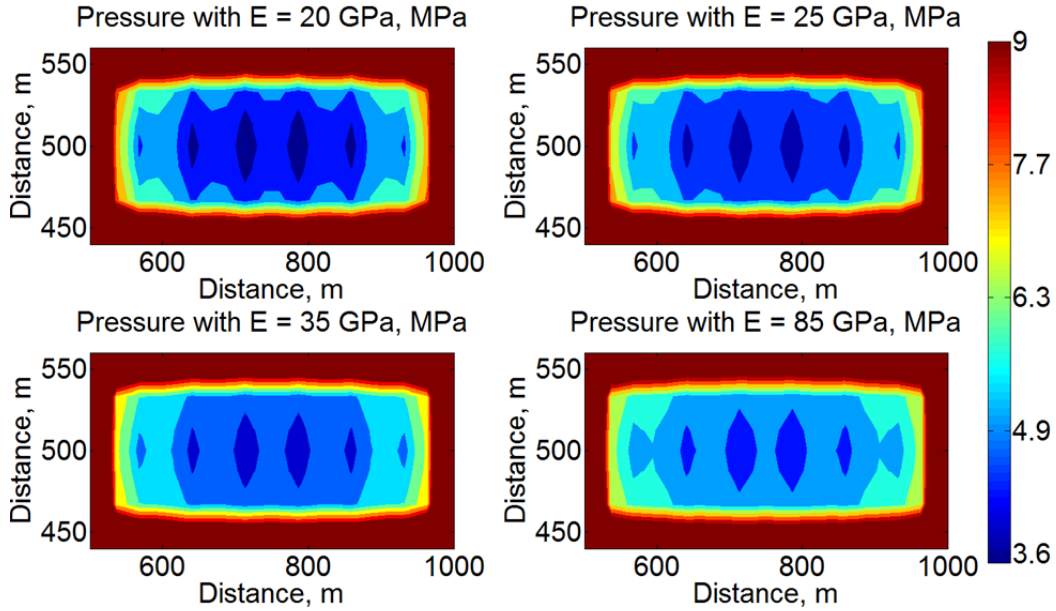

Figure 3.9. Pressure contours in the SRV with different Young's moduli at the end of the simulation (reprinted with permission from Guo et al. 2018a)

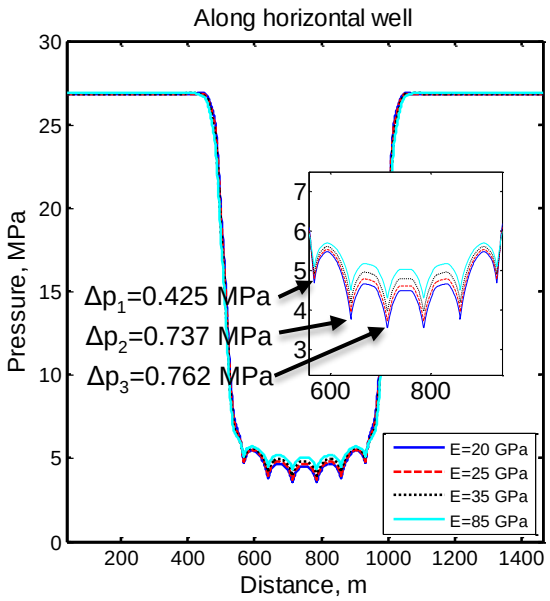

Figure 3.10. 1D pressure distribution along the horizontal well with different Young's moduli (reprinted with permission from Guo et al. 2018a)

Then, the effect of Biot's coefficient is studied. Biot's coefficient is defined as a poroelastic term ranging between 0 and 1 that depicts the compressibility of porous media with fluid saturation. A small Biot's coefficient indicates that the solid phase compressibility is large compared to the compressibility of the fluid saturated porous media. A small Biot's coefficient also indicates increased rock stiffness. Except for the Biot's coefficient of 1.0 as in the base case, another two values of 0.6 and 0.8 are tested.

Figure 3.10 and Figure 3.11 show the gas production rates and the corresponding cumulative gas production rates simulated with various Biot's coefficients. The difference

between various cases is not significant. Based on the zoomed in plots, greater Biot's coefficients lead to lower production and stronger geomechanical effects. Again, Eq. 3.1 is used for the explanation: the values of the geomechanical terms $\frac{b-\phi}{K_s}$ and $b\frac{\partial \varepsilon_v}{\partial t}$ increase as b increases. For the overall simulation time of 653 days, the difference of cumulative production between the decoupled simulation and the coupled simulation increases with the increase of Biot's coefficient. The difference is 1.36×10^4 m^3 for Biot's coefficient of 0.6. As Biot's coefficient increases to 0.8, the difference is 1.52×10^4 m^3. As Biot's coefficient further increases to 1.0, the difference becomes 1.60×10^4 m^3.

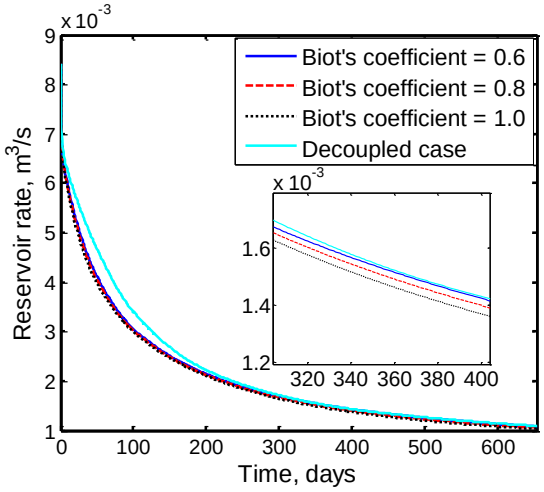

Figure 3.11. Gas rates with different Biot's coefficients (reprinted with permission from Guo et al. 2018a)

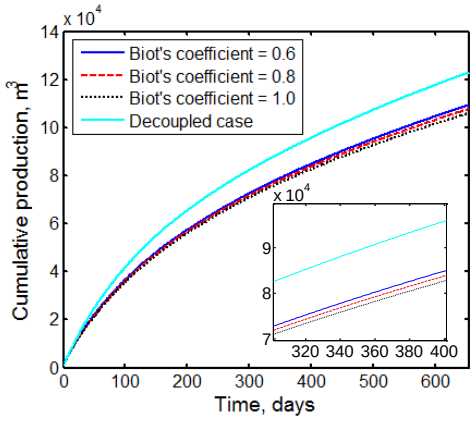

Figure 3.12. Cumulative gas production with different Biot's coefficients (reprinted with permission from Guo et al. 2018a)

Finally, the geomechanical effect of Poisson's ratio on reservoir response is studied. Poisson's ratio denotes the relationship between the deformation in the axial direction and in the transverse direction. A small Poisson's ratio indicates that more bulk volume is changed in the deformation. Except for the Poisson's ratio of 0.22 in the base case, another two Poisson's ratio values 0.12 and 0.22 are tested.

Figure 3.13 and Figure 3.14 show the gas rates and the corresponding cumulative gas rates for the analysis of effects of Poisson's ratios. Decreasing the value of Poisson's ratio decreases the production rates, and Poisson's ratio of 0.12 has the lowest production rates. Based on Eq. 3.1, changing Poisson's ratio actually changes the geomechanical term $\frac{b-\phi}{K_s}$, as the bulk modulus term can be denoted by Poisson's ratio in linear elasticity as

$$K = \frac{E}{3(1-2\nu)}, \tag{3.6}$$

where K is the bulk modulus, which has a linear relationship with Young's modulus via Poisson's ratio. It is noted that as Poisson's ratio ν decreases, the bulk modulus term also decreases, which further increases the value of the geomechanical term $\frac{b-\phi}{K_s}$, indicating enhanced geomechanical effects on reservoir response and decreased production. As Poisson's ratio increases from 0.12 to 0.32, the corresponding cumulative production difference between decoupled and coupled simulations decreases from 1.89×10^4 m^3 to 1.48×10^4 m^3.

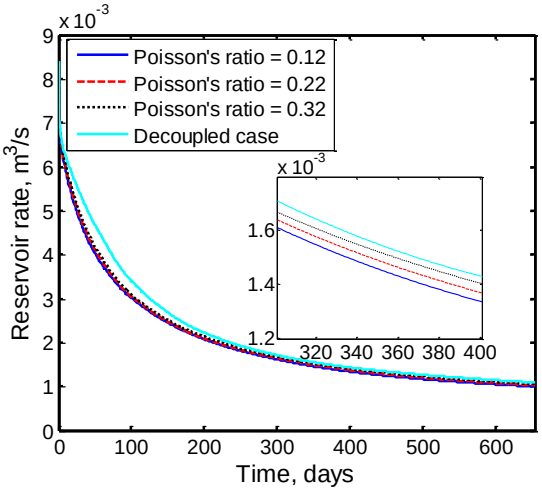

Figure 3.13. Gas rates with different Poisson's ratios (reprinted with permission from Guo et al. 2018a)

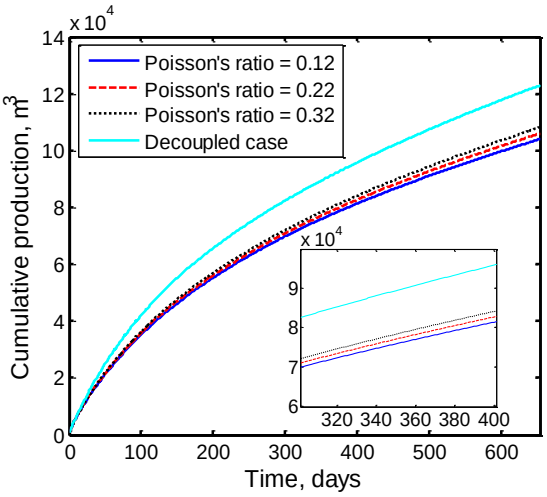

Figure 3.14. Cumulative gas production with different Poisson's ratios (reprinted with permission from Guo et al. 2018a)

3.3.3 Fracture Spacing

The role of fracture spacing is discussed based on the numerical results from the fully coupled flow and geomechanics modeling. Fracture spacing is an important parameter for the development of unconventional reservoirs produced by multi-stage hydraulic fractures.

In this sensitivity analysis, the length of the horizontal well is kept as constant, with the number of fractures changing. Totally four fracture densities (6, 9, 12, and 15 bi-wing fractures) are studied. Figure 3.15 presents the map view of the 6-fracture and the 9-fracture cases. As the fracture number increases from six to nine, the fracture spacing decreases from 38 m to 25 m. Note that fractures are distributed with uniform spacing along the horizontal wellbore.

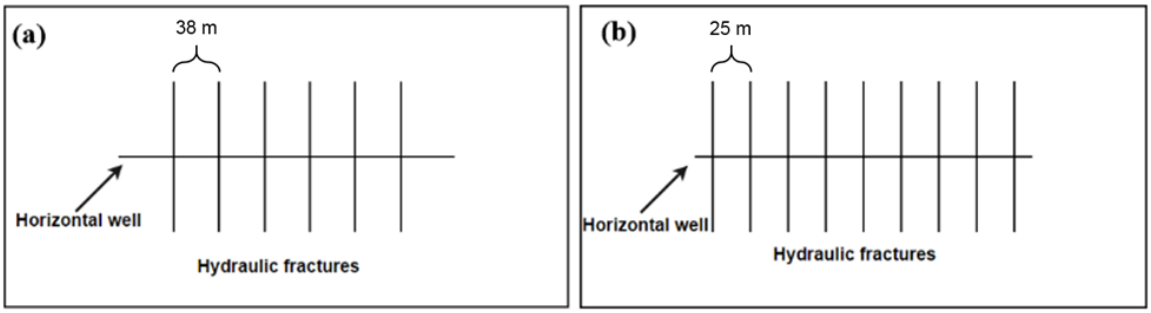

Figure 3.15. Map views of 6- and 9-fracture cases (reprinted with permission from Guo et al. 2018a)

Figure 3.16 shows the gas rates at reservoir condition with various fracture numbers. Figure 3.17 shows the corresponding cumulative gas production. Intuitively, cases with more fractures have higher production rates, and this trend is especially obvious at early stages of the production. After 400 days of production, the difference of production rates is nearly negligible. This is because more fractures only expedite hydrocarbon production within the high permeability zones in the SRV. Once the SRV is largely depleted, denser fractures are not able to facilitate the depletion outside the SRV. Based on the cumulative production results, the difference between the lowest and highest results at 300 days does not change much as it proceeds to 653 days (the end of the simulation time). The change is from 3.1×10^4 m^3 to 3.3×10^4 m^3.

Although Figure 3.16 and Figure 3.17 intuitively show that more fractures lead to faster hydrocarbon depletion, in the field, the maximum number of fractures that can be stimulated along the horizontal well is limited by the stress shadow effect (Roussel and

Sharma 2011; Nagel et al. 2013). Therefore, in order to have a comprehensive understanding of the optimum fracture spacing, hydraulic fracturing modeling should also be considered if the optimum fracture number needs to be determined in field cases. Further analysis of fracturing interference is provided in Section 5.

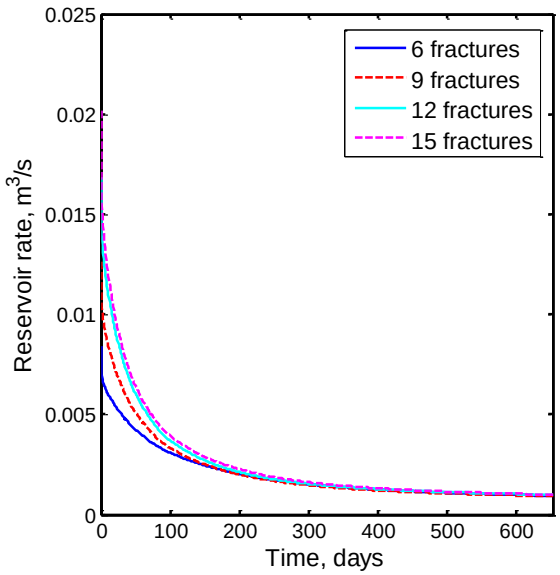

Figure 3.16. Gas rates with different fracture numbers (reprinted with permission from Guo et al. 2018a)

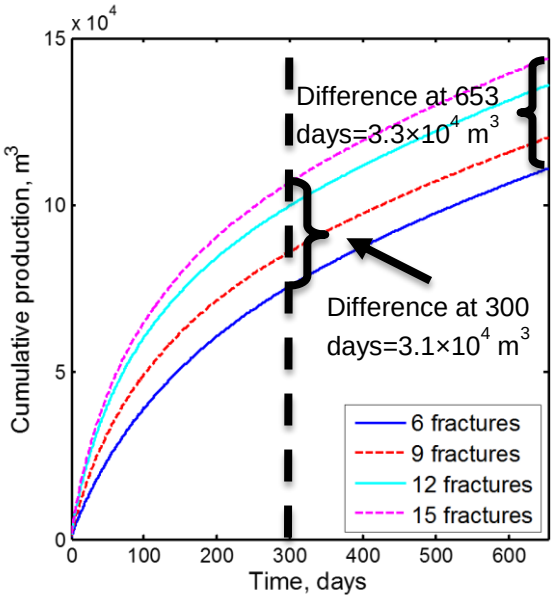

Figure 3.17. Cumulative production with different fracture numbers (reprinted with permission from Guo et al. 2018a)

Figure 3.18 shows the 1D pressure distribution along the horizontal wellbore for various fracture numbers at the end of the simulation time. Sharp decreases of pressure represent the producing intervals. Cases with denser fractures have lower pressure profiles within the SRV. Pressure outside the SRV is generally identical to the initial reservoir pressure for cases with 6, 9, and 12 fractures, while the case with 15 fractures has lower pressure outside the SRV, with pressure decreasing from the initial value of 26.9 MPa to 25 MPa. This pressure decrease is caused by the boundary condition: since no flow boundaries are used, the strong pressure depletion caused by the 15 fracture within the SRV leads to a sharp pressure gradient, which decreases the pressure outside the SRV.

Figure 3.19 further shows the 2D maps of pressure contours for cases with various fracture numbers. For fracture number of 6, pressure contours can still identify the shapes of the hydraulic fractures. As fracture number increases, pressure is further decreased in the SRV. Average pressure in the shown 2D rectangles is calculated for the quantification of this trend: as fracture number increases from 6 to 15, average pressure decreases from 14.11 MPa to 11.71 MPa.

How fracture number correlates with geomechanical effects on reservoir response is shown in Figure 3.20. For each fracture number case, the comparison of cumulative productions from the coupled simulation and the decoupled simulation is made. For cases with six and nine fractures, the difference is the lowest with a value of 12.8%. The 12-fracture case has a difference of 14.7%. The largest difference is obtained in the case with 15 fractures, with a value of 14.9%. This result indicates that denser fractures lead to greater geomechanical effects on reservoir response. This is because denser fractures lead to greater pressure depletion, which results in greater geomechanical effects on pressure decrease as concluded before.

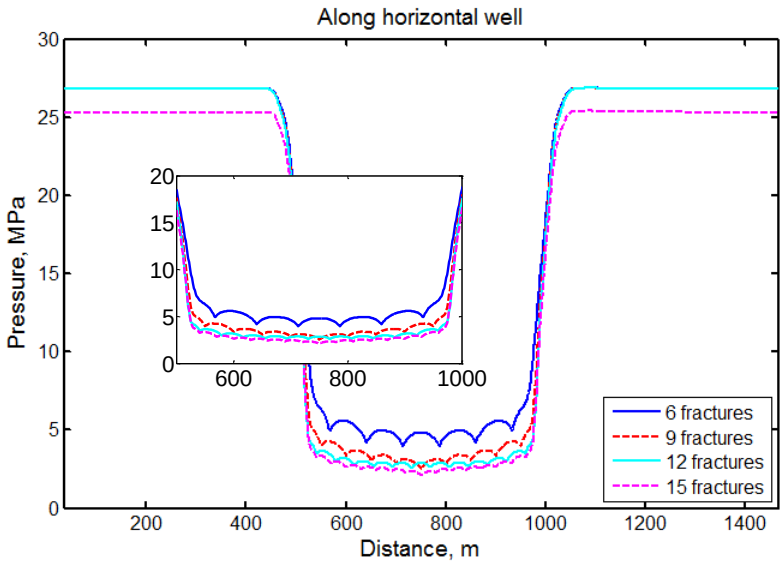

Figure 3.18. 1D pressure distribution along the horizontal well for various fracture number cases (reprinted with permission from Guo et al. 2018a)

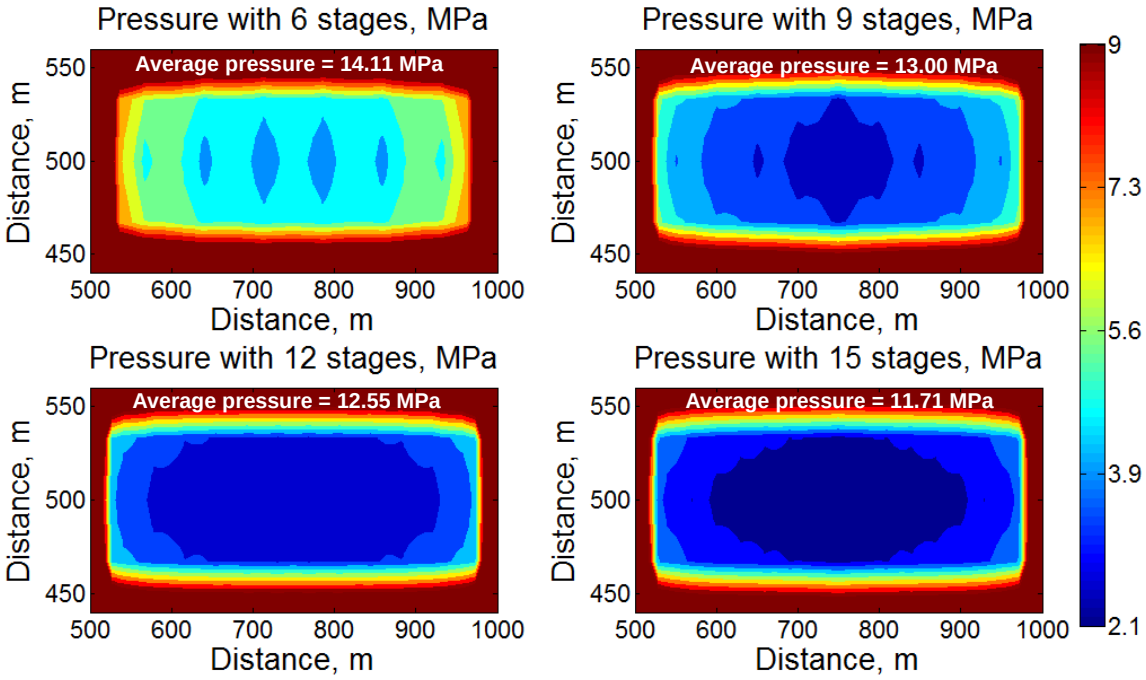

Figure 3.19. Pressure contours and average pressure for different fracture numbers at the end of the simulation time (reprinted with permission from Guo et al. 2018a)

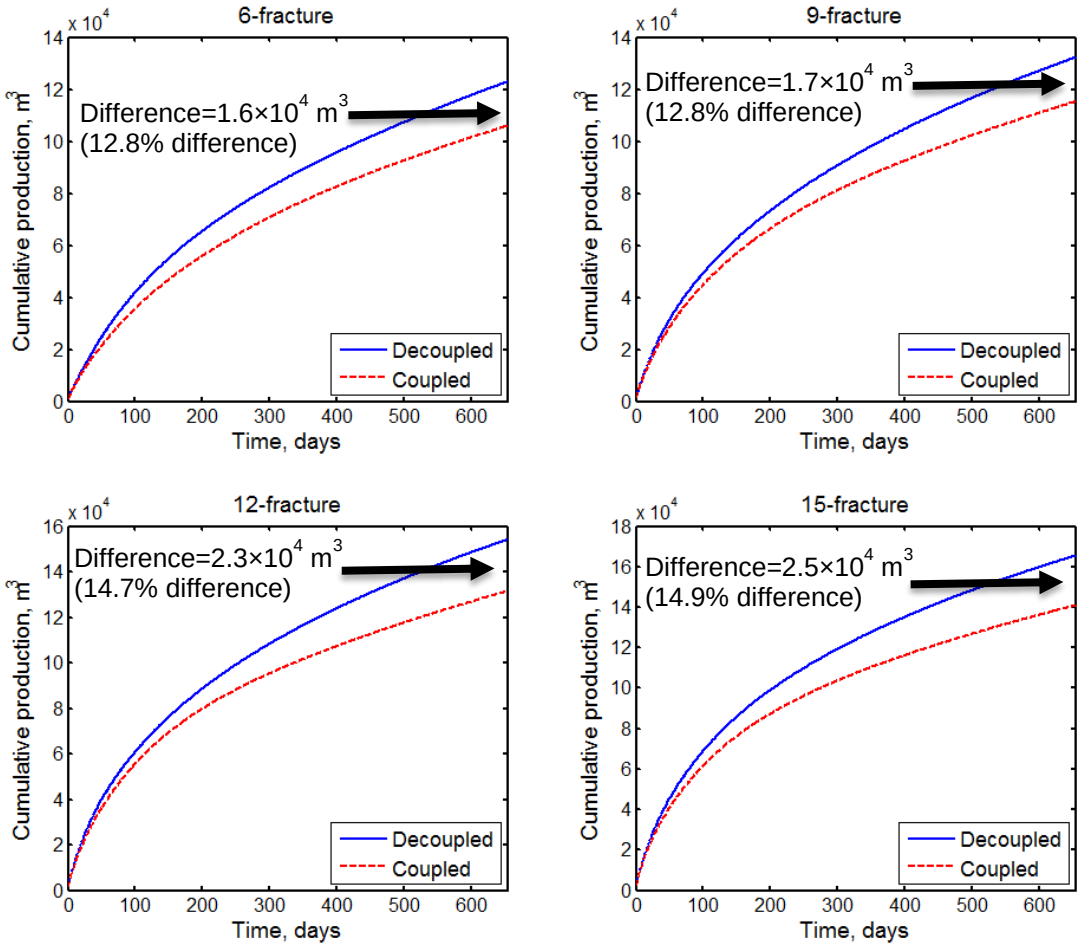

Figure 3.20. Cumulative production with various fracture numbers compared to decoupled simulations (reprinted with permission from Guo et al. 2018a)

3.3.4 Fracture Length

Another key parameter for fracture geometry is fracture length (or fracture half-length). Except for the half-length of 46 m in the base case, another two half-lengths of 23 m and 69 m are investigated. The fracture number is always six in this analysis. The width

of SRV is also changed as fracture half-length changes so that the SRV can fully cover the hydraulic fractures. Decoupled simulations with various fracture half-lengths are also run for comparison.

Figure 3.21 shows the pressure distribution along the horizontal well for different fracture half-lengths at the end of the simulation. Pressure distributions from the coupled simulation are compared to results from the decoupled simulation. Then, the coupled simulations are compared. The pressure difference between coupled and decoupled simulation results at the third fracture is shown. Fracture half-length of 23 m has the smallest pressure difference of 0.427 MPa, while fracture half-length of 69 m leads to the largest pressure difference of 0.681 MPa. This indicates that greater fracture half-length corresponds to greater geomechanical effects on reservoir's pressure response. Besides, greater fracture half-length leads to higher pressure profile. The average pressure along the 1D line along the horizontal well for fracture half-length of 23m is 19.43 MPa. The average pressure for fracture half-length of 46 m is 19.53 MPa. The average pressure for fracture half-length of 69 m is 19.73 MPa.

In a similar way, cumulative productions are plotted in Figure 3.22. Intuitively, the greatest fracture half-length leads to the highest cumulative production curve. Increasing the fracture half-length from 23 m to 69 m can increase the cumulative production in 653 days for 3.7×10^4 m^2. However, the correlation between fracture half-length and geomechanical effects on production response is not uniform: the greatest difference between production results from coupled and decoupled simulations is obtained as 12.8%

with the intermediate fracture half-length of 46 m, while the differences are lower for cases with fracture half-lengths of 23 m and 69 m.

Although greater fracture half-length leads to higher overall cumulative production, the largest fracture half-length that can be obtained in field applications is actually limited by the effect of stress shadow (Roussel and Sharma 2011; Nagel et al. 2013), and fracturing interference analysis should be conducted for more comprehensive understanding. Fracturing interference is discussed in Section 5.

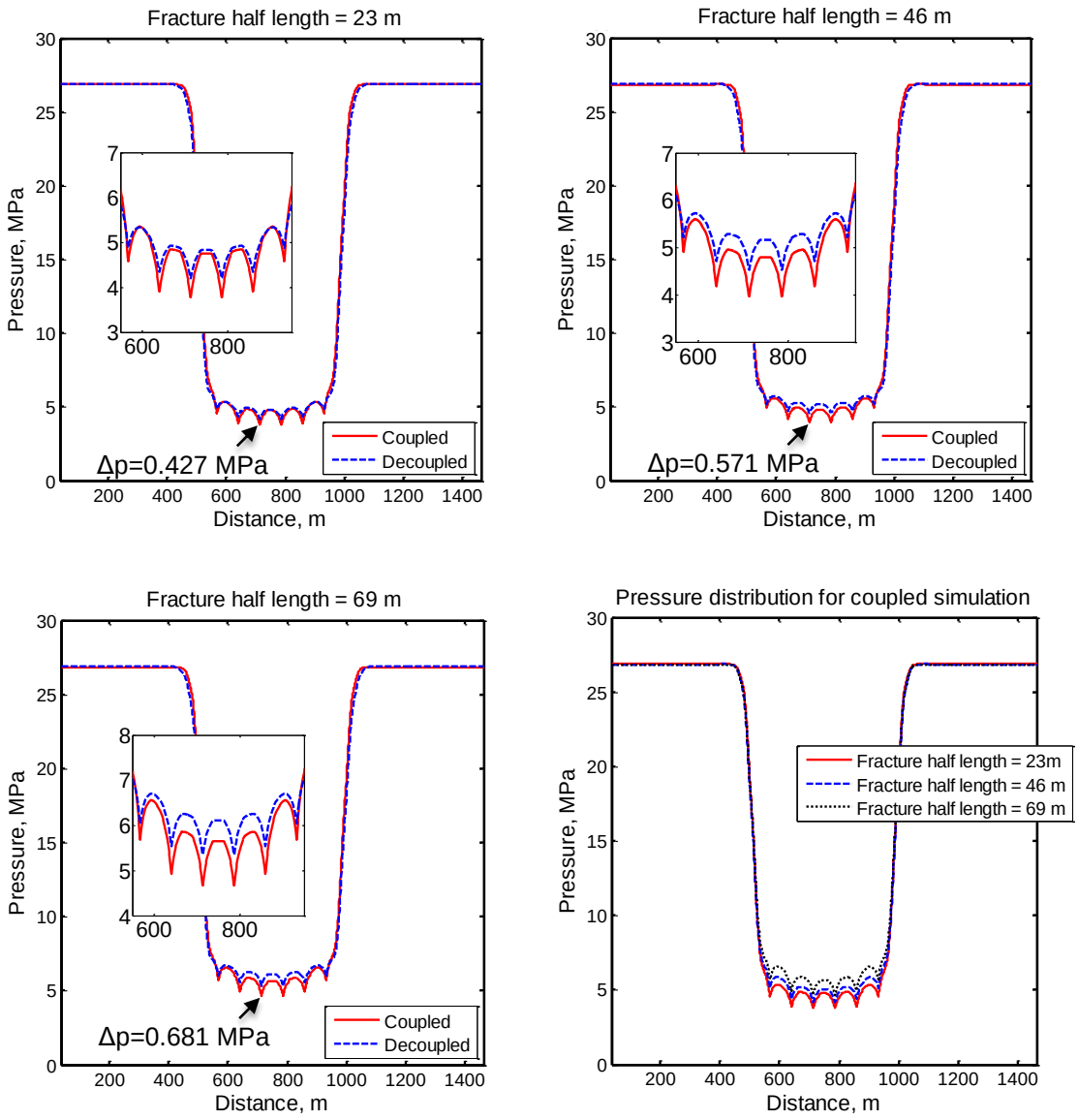

Figure 3.21. 1D pressure distribution along the horizontal well for different fracture half-lengths compared to decoupled simulation results (reprinted with permission from Guo et al. 2018a)

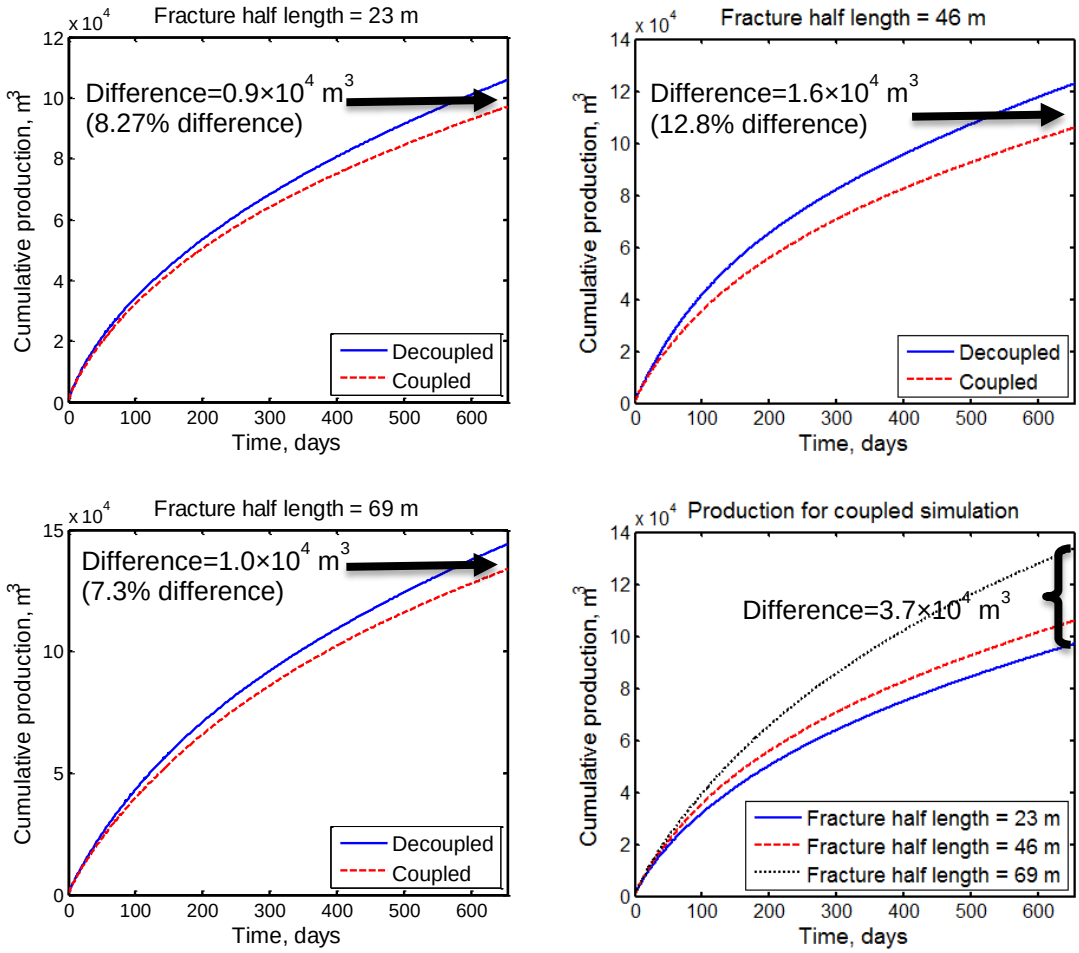

Figure 3.22. Cumulative production for different fracture half-lengths compared to decoupled simulation results (reprinted with permission from Guo et al. 2018a)

3.3.5 Rank of Effects

After the quantitative study of several relevant parameters, the relative importance of each parameter is listed in a ranking so that one can identify the most important parameter and the least important parameter considering geomechanical effects on reservoir response. Following the discussion in Guo et al. (2018a), the analysis is made

based on the cumulative gas production over 653 days. ΔQ in % is first defined to denote the difference between the maximum and minimum cumulative productions in the coupled simulation results in the sensitivity analysis of a certain parameter. As an example, in Section 3.2.2, in the study of effects of Young's modulus (Figure 3.8),

$$\Delta Q = \frac{11.78\times10^4 - 10.01\times10^4}{11.78\times10^4} = 15.03\%, \tag{3.7}$$

where 11.78×10^4 is the maximum cumulative production obtained at E of 85 GPa and 10.01×10^4 is the minimum cumulative production obtained at E of 20 GPa.

Then, Δn in % is defined to denote the difference between the maximum and minimum values of the investigated parameter in the specific sensitivity analysis. As an example, in the study of Young's modulus,

$$\Delta n = \frac{85-20}{85} = 76.47\%, \tag{3.8}$$

where 85 is the maximum value and 20 is the minimum value of the investigated Young's moduli.

Thus, the relative influence of a parameter can be determined by $\Delta Q/\Delta n$, which stands for the change of simulated cumulative production in % corresponding to every 1% change of the value of the investigated parameter in a specific sensitivity analysis. A large $\Delta Q/\Delta n$ indicates that the investigated parameter has great effects on cumulative production based on the fully coupled flow and geomechanics modeling while a small $\Delta Q/\Delta n$ indicates that the parameter has less influence. Detailed analysis is in Table 3.2. Based on the rank of $\Delta Q/\Delta n$, the influences of the parameters can be listed from the

greatest to the smallest as fracture number > fracture length > Young's modulus > Poisson's ratio > Biot's coefficient.

Studied parameter	Difference between the maximum and the minimum cumulative productions (ΔQ), %	Difference between the maximum and the minimum values of the studied parameter (Δn), %	Change of cumulative production (in %) for every 1% change of the value of the studied parameter ($\Delta Q/\Delta n$)
Young's modulus	15.03%	76.47%	0.197
Biot's coefficient	3.02%	66.67%	0.045
Poisson's ratio	3.79%	62.50%	0.061
Fracture number	24.49%	40.00%	0.612
Fracture length	27.41%	66.67%	0.411

Table 3.2. Quantitative rank of effects of investigated parameters (reprinted with permission from Guo et al. 2018a)

3.4 Conclusion

Based on numerical results, it is indicated that the effects of incorporating geomechanical effects with fluid flow are generally not significant. From the engineering perspective, the difference between coupled and decoupled simulation results below 10% is deemed as insignificant in this specific numerical study. In such insignificant cases, it is proposed that the direct usage of decoupled flow only simulation can evaluate the pressure and production responses from the reservoir. When the difference is greater than

10%, coupled flow and geomechanics simulation should be used to account for geomechanical effects on reservoir response as these effects can no longer be ignored.

Using the criterion of 10%, in this study, decoupled simulation can be directly used for cases with Young's modulus greater than 35 GPa, with Biot's coefficients greater than 0.6, and with Poisson's ratios ranging from 0.12 to 0.32. However, the exception is obtained for cases with Young's modulus less than 35 GPa which indicates rocks with lower stiffness. Here, Young's modulus less than 35 GPa indicates significant geomechanical effects on pressure and production. If pressure and production are the primary concerns, the coupled simulation should be used in the evaluation. It is noted that the critical value of 35 GPa for Young's modulus is valid in this specific numerical study and cannot be generalized. In a different reservoir geomechanics case, new numerical analyses should be conducted to determine the proper criteria for the selection of the appropriate simulation model.

The numerical results provide complementary analyses to the literature. Numerical results here are based on fully coupled flow and geomechanics modeling, which is an extension of the work presented by Yu and Sepehrnoori (2014) where geomechanics is simplified to the usage of a stress-sensitive compaction table. Besides, the general trends of geomechanical effects on the decrease of production rates observed in this study are in accordance with Yu and Sepehrnoori (2014) and An et al. (2017). This study also investigates parameters that were not considered in the coupled flow and geomechanics modeling by Moradi et al. (2017) and An et al. (2017). In conclusion:

(1) The consideration of linear elasticity in the model decreases the simulated production rates compared to decoupled flow only simulation.

(2) Simulated gas rates increase with the increase of Young's modulus. A sufficiently large Young's modulus representing essentially non-deformable reservoir rock leads to simulated gas rates that are very close to the rates simulated by the decoupled flow only model.

(3) Effects of rock mechanics on reservoir response are the most significant at the center of the well, and are insignificant at two far ends of the well and outside the SRV where pressure depletion is insignificant.

(4) The influences on reservoir response of the studied parameters can be ranked from the largest to the smallest as fracture number > fracture length > Young's modulus > Poisson's ratio > Biot's coefficient.

4 PRODUCTION-INDUCED STRESS STATE CHANGES*

4.1 Introduction

In this section, detailed analysis of production-induced stress state changes at the infill location is carried out. The study is based on an Eagle Ford model with oil and water production. History match is used for the calibration of the parameters in the reservoir model. After the parameterization, sensitivity analyses are conducted to investigate the effects of parent well and rock mechanics on infill zone stress evolution. The model presented in Section 2.1 is used.

*Part of this section is reprinted with permission from "Investigation of Production-Induced Stress Changes for Infill Well Stimulation in Eagle Ford Shale" by X. Guo, K. Wu, and J. Killough. SPE Journal, Copyright [2018] by Society of Petroleum Engineers.

4.2 Model Calibration

Field data from Eagle Ford Shale are used to construct the reservoir model. Hydrocarbon production was first obtained in Eagle Ford in 2008 and hydraulic fractures were used for the commercial development of hydrocarbons in the low permeability reservoirs. It has two formations: Upper Eagle Ford and Lower Eagle Ford. Lower Eagle Ford is the primary target for hydrocarbon production due to its organic rich nature (Simpson et al. 2016). Based on the Lower Eagle Ford data, a reservoir model including a single stage of a completed horizontal well is shown in Figure 4.1 for history matching. Four fractures with non-uniform half-lengths are represented.

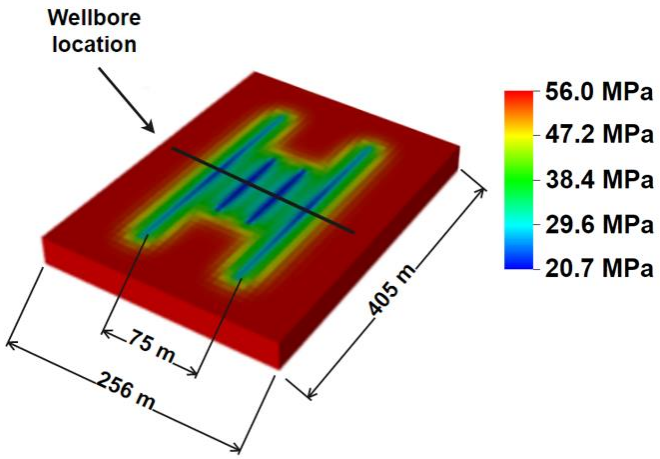

Figure 4.1. Single stage horizontal well in the Lower Eagle Ford formation (reprinted with permission from Guo et al. 2018b)

The fractures along the wellbore in Figure 4.1 are not uniform, with two outer fractures longer than inner fractures. The geometry is determined by field observations (Webster et al. 2013; Wheaton et al. 2014; Ugueto et al. 2016), fracture modeling results (Wu and Olson 2015; Wu and Olson 2015b; Wu et al. 2016), and available microseismic data. The stress shadow effect in fracturing propagation is also used to explain the shorter inner fractures: the growth of the two outer fractures inhibits the growth of the two inner fractures.

The mesh of the reservoir model has two layers in the vertical direction, and only the lower layer is produced to denote the production from the Lower Eagle Ford layer. This assumption is based on the fact that the physical properties in the Upper Eagle Ford layer indicate low hydrocarbon production potential. Besides, it is assumed that the hydraulic fracture height fully covers the Lower Eagle Ford layer, which will later be validated by history matching.

History matching is then carried out to calibrate parameters used in the model. For more efficient finite element modeling efficiency, production data from only the single stage well with four hydraulic fractures are used. The constraint used in the history matching is bottomhole pressure, and oil and water production rates are the objective functions for matching. Figure 4.2 shows the inputs for BHP for five years. Permeability, compressibility, porosity, and fracture lengths are adjusted. In addition, since no relative permeability data are available, a calibrated relative permeability curve is also constructed. The initial guesses for relative permeabilities are

$$k_{rw} = (S_w - S_{wi})^2, \tag{4.1}$$

$$k_{ro} = (1 - S_w - S_{oi})^2, \tag{4.2}$$

and they are adjusted based on matching with production rates and available connate water saturation data. The relative permeability curves are calibrated with final forms in Figure 4.3. The history matched oil and water production rates are shown in Figure 4.4 and Figure 4.5. History matched parameters for the reservoir model are shown in Table 4.1.

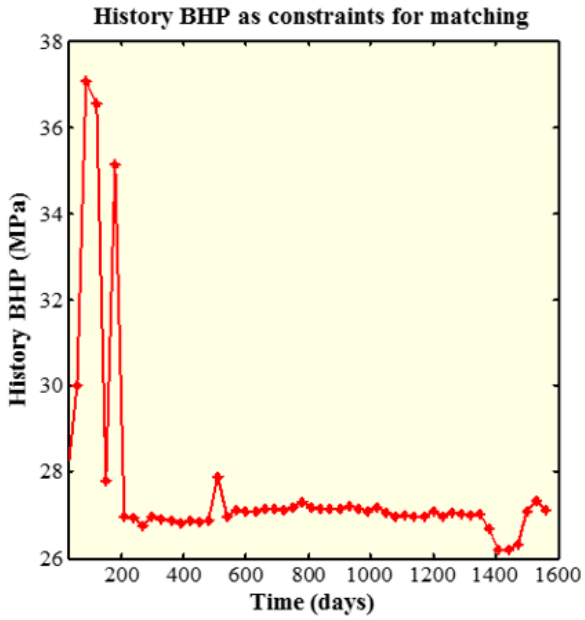

Figure 4.2. Bottomhole pressure as matching constraint (reprinted with permission from Guo et al. 2018b)

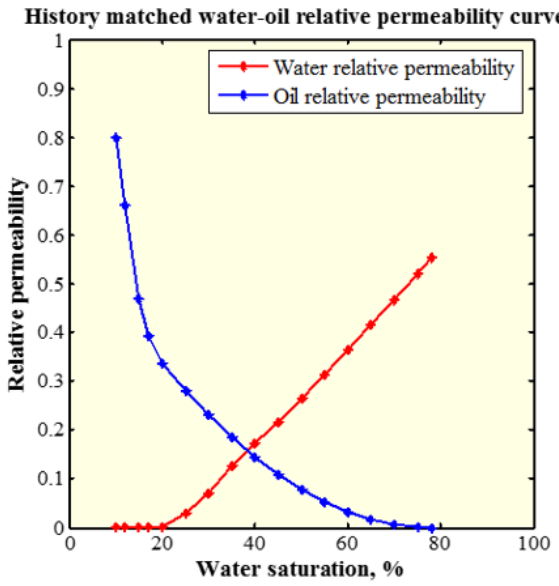

Figure 4.3. Calibrated relative permeability curves (reprinted with permission from Guo et al. 2018b)

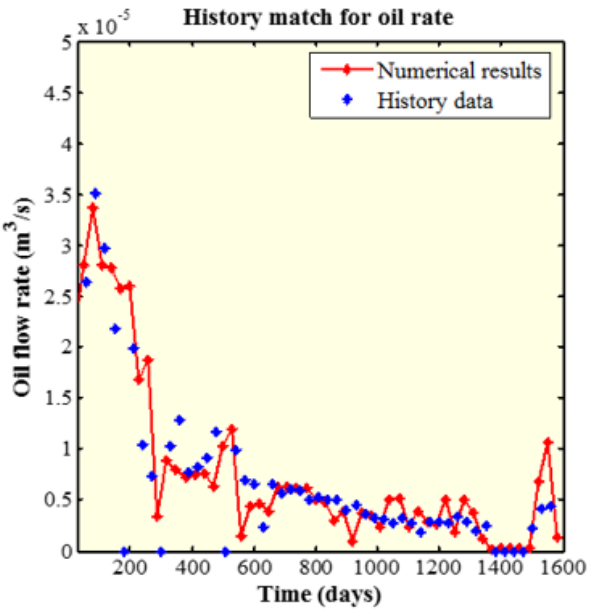

Figure 4.4. History matched oil production rates (reprinted with permission from Guo et al. 2018b)

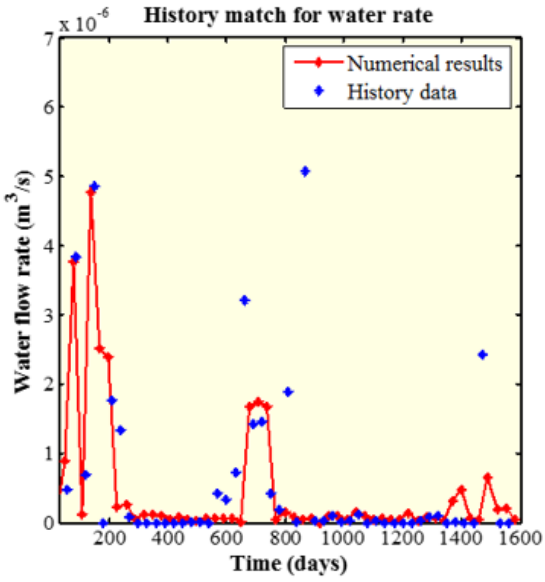

Figure 4.5. History matched water production rates (reprinted with permission from Guo et al. 2018b)

Parameter	Value
Numerical model setup	
Dimensions	405 m × 256 m × 30 m
Grid numbers	65 × 82 × 2
Calibrated reservoir parameters	
Permeability, m^2	4.7×10^{-19}
Fracture conductivity, m^2-m	8.06×10^{-13}
Porosity, %	12
Longer fractures' half length, m	150
Shorter fractures' half length, m	50
Fracture height, m	15
Fracture spacing, m	25
Young's modulus, GPa	20
Poisson's ratio	0.22
Biot's coefficient	1.0
Initial pressure, MPa	56.02
Differential stress, MPa	3
Initial S_{Hmax}, MPa	68
Initial S_{hmin}, MPa	65

Table 4.1. History matched parameters for the reservoir model (reprinted with permission from Guo et al. 2018b)

4.3 Analysis of Stress Evolution

Sensitivity analyses are then presented to study the detailed correlations between infill zone stress state changes and relevant reservoir and geomechanical parameters. The

calibrated model in Figure 4.1 is duplicated as in Figure 4.6 so that an infill zone is obtained for the analyses. The well spacing is 400 m. Other parameters for the base case are in Table 4.1. The only exception is BHP: instead of using the noisy BHP data in history matching, a constant BHP of 20.7 MPa (3000 psi) is prescribed for parent well productions.

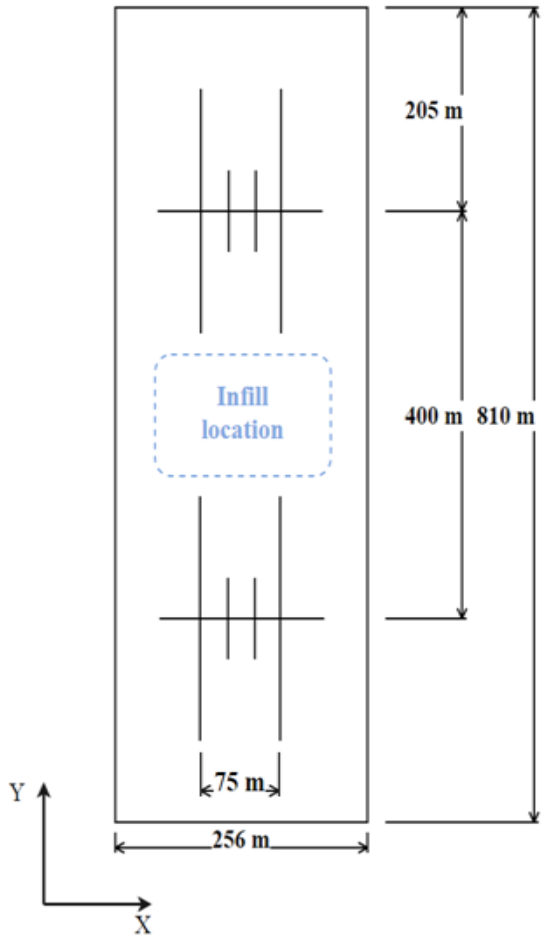

Figure 4.6. Setup of completed parent wells and the infill zone (reprinted with permission from Guo et al. 2018b)

Table 4.2 shows the values of parameters investigated in the base case and in the five sensitivity analyses. In each sensitivity analysis, another two values except for the base case value are investigated using the numerical model. The corresponding results and then presented and the discussions are provided.

	Base case	**BHP**	**Fracture geometry**	**DS**	**Well spacing**	**Young's modulus**
BHP	20.7 MPa (3000 psi)	13.79 MPa 27.58 MPa	Base	Base	Base	Base
Fracture geometry outer x_f – inner x_f	150m –50m (492ft – 164ft)	Base	50m – 150m 70m – 70m	Base	Base	Base
DS	3 MPa (435 psi)	Base	Base	0 MPa 6 MPa	Base	Base
Well spacing	400m (1312ft)	Base	Base	Base	300m 350m	Base
Young's modulus	20 GPa (2900 ksi)	Base	Base	Base	Base	10 GPa 30 GPa

Table 4.2. Parameters and their values investigated in the sensitivity analyses (reprinted with permission from Guo et al. 2018b)

Base case 2D results of pressure, S_{Hmax} orientation (white dashed lines), S_{Hmax}, and S_{hmin} after 5 years of parent well production are shown in Figure 4.7. Pressure at fractured reservoir volume is largely depleted due to the high permeability in fractures. Pressure outside the fractured reservoir volume and at the infill zone location is not significantly depleted due to the low matrix permeability. Significant stress reorientation for S_{Hmax} is observed around hydraulic fractures (purple circles) and at the infill location. Specifically

at the infill location, totally reversed S_{Hmax} is observed in the X direction. Although pressure depletion is insignificant at the infill location, production-induced rock deformation and stress changes are significant in the infill location (S_{Hmax} and S_{hmin} 2D maps), which leads to the reorientation and reversal. 2D maps of S_{Hmax} and S_{hmin} indicate that stress magnitudes at the center of the infill location are smaller. Also, stress magnitudes at fractured reservoir volumes are smaller due to the largely depleted reservoir pressure.

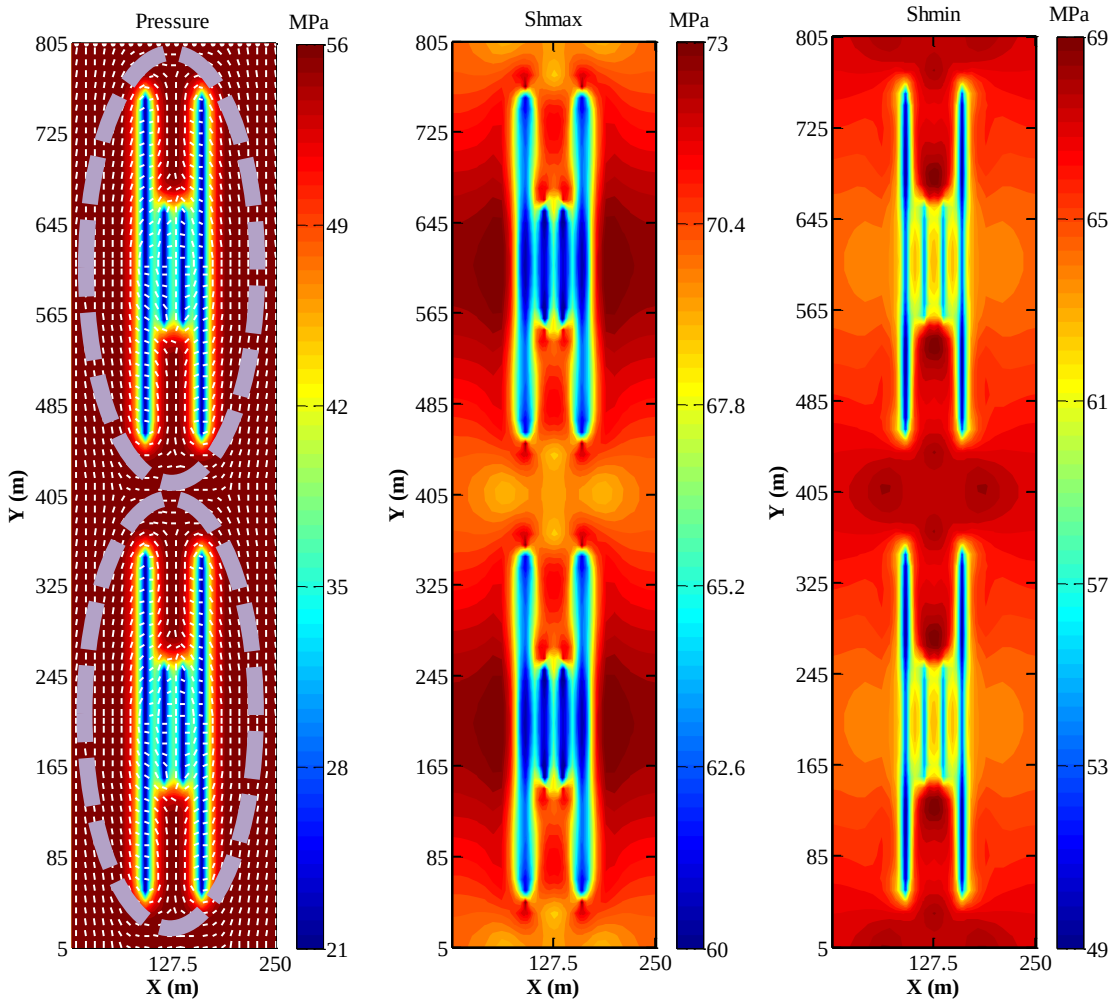

Figure 4.7. 2D Base case numerical results of pressure mounted with S_{Hmax} orientation (white dashed lines), S_{Hmax}, and S_{hmin} at 5 years of production (reprinted with permission from Guo et al. 2018b)

4.3.1 Parent Well Bottomhole Pressure

The effect of bottomhole pressure in parent wells on stress evolution is first investigated. It is a key parameter for reservoir development using tightly spaced

horizontal wells. Except for the base case value of 20.7 MPa, another two values of 13.79 MPa and 27.58 MPa are simulated. After 5 years of parent well production simulation, pressure and S_{hmin} results for BHP of 13.79 MPa are shown in Figure 4.8 and the results for BHP of 27.58 MPa are shown in Figure 4.9. Results show that increased parent well BHP leads to less pressure depletion and stress disturbance in the reservoir after 5 years of parent well production.

In order to provide more detailed analysis of how stress changes with the change of parent well BHP, 1D spatial distributions along the infill line (Y=405 m) for angle change of S_{Hmax} and S_{hmin} after 5 years of production are plotted as in Figure 4.10. Similarly, stress temporal evolution at an observation point at the center of the infill zone (X=127.5 m and Y=405 m) during the 5 years of parent well production is plotted as in Figure 4.11.

Figure 4.12 shows the 1D distributions of S_{Hmax} reorientation and S_{hmin} at 5 years along Y=405 m. Smaller parent well BHP leads to greater stress reorientation and lower S_{hmin} distribution curve. This is explained by the fact that lower BHP results in more pressure depletion and greater rock deformation, indicating greater stress state changes. Figure 4.13 indicates that the decrease of parent well BHP decreases the parent well production time it requires to reach the beginning of stress reversal. The beginning of stress reversal is 1.3 years for the base case, 1 year for the decreased BHP case, and 2.1 years for the increased BHP case. Besides, the decreased BHP case has the lowest S_{hmin} evolution curve due to the large pressure depletion in this case.

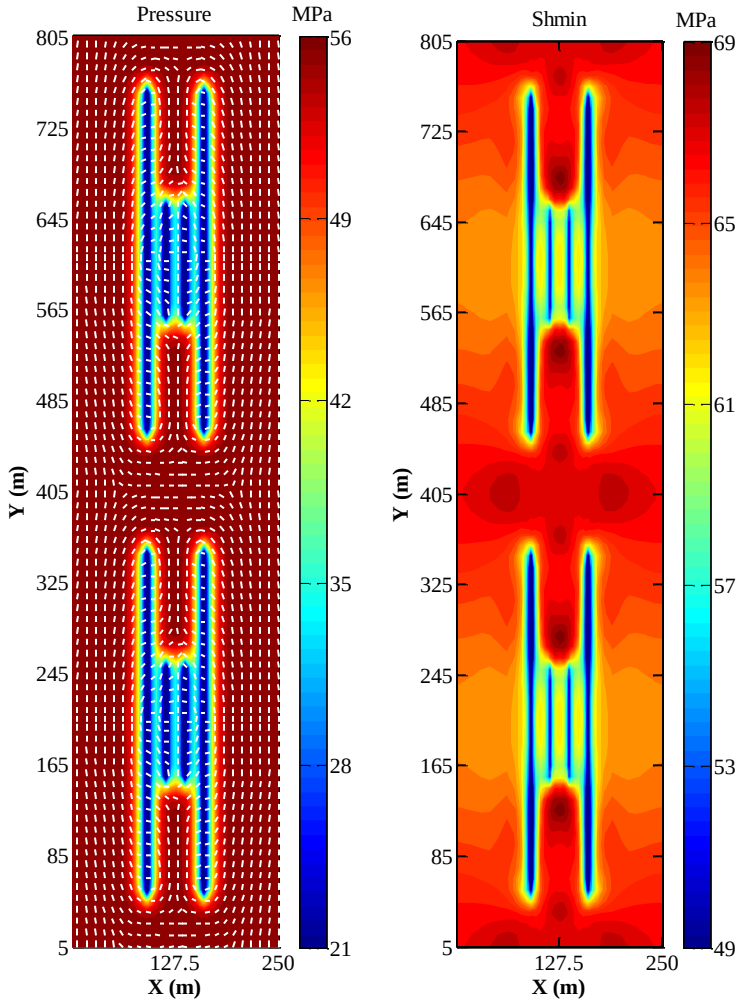

Figure 4.8. Pressure, S_{Hmax} orientation and S_{hmin} for BHP of 13.79 MPa (reprinted with permission from Guo et al. 2018b)

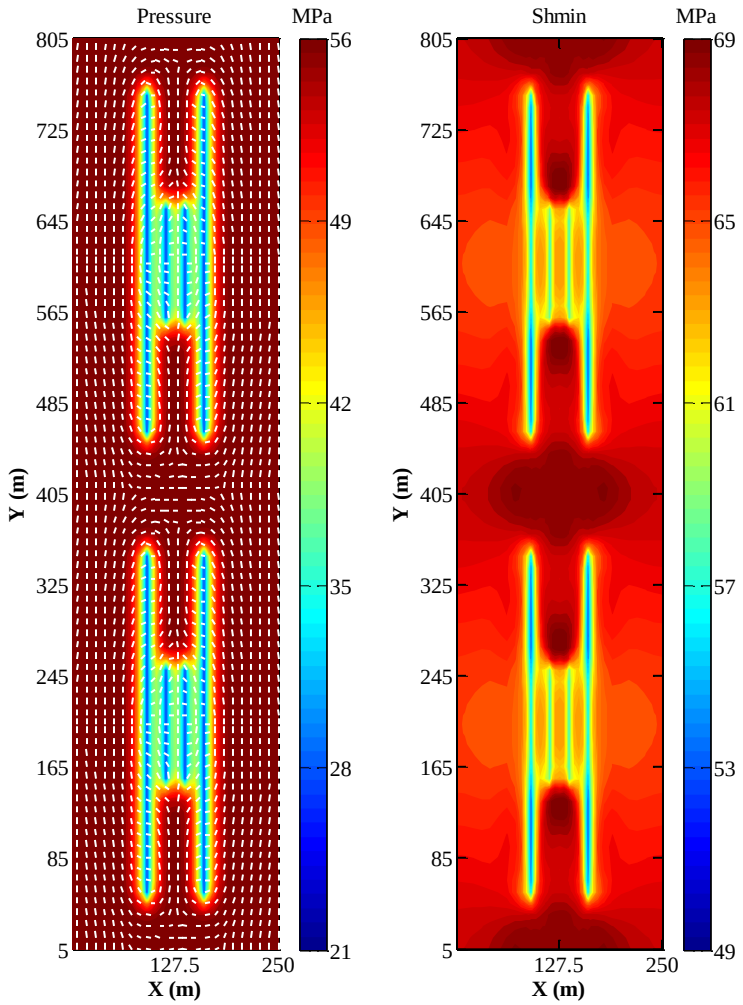

Figure 4.9. Pressure, S_{Hmax} orientation and S_{hmin} for BHP of 27.58 MPa (reprinted with permission from Guo et al. 2018b)

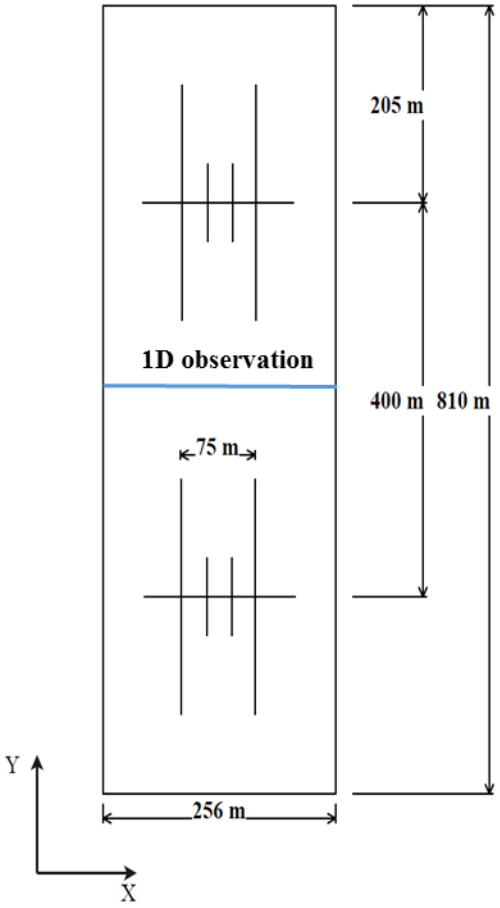

Figure 4.10. 1D monitoring scheme for properties along the infill line at Y=405 m

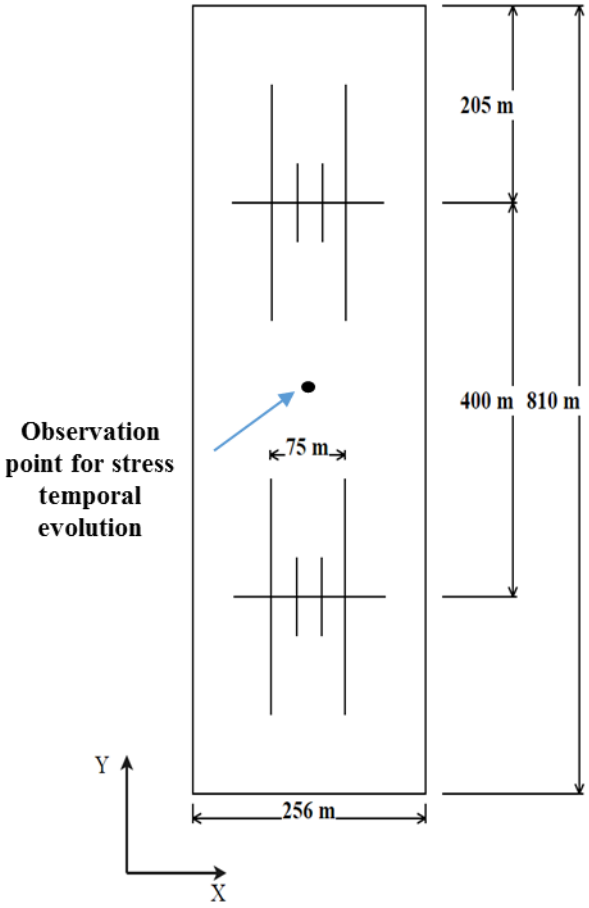

Figure 4.11. Observation point for the temporal evolution of stress

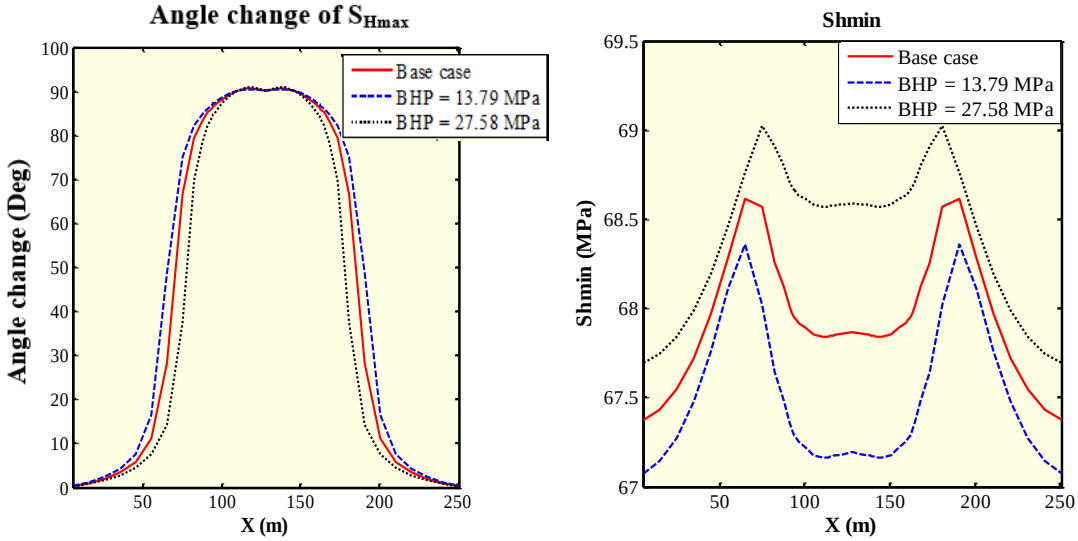

Figure 4.12. S_{Hmax} reorientation and S_{hmin} along Y=405 m at 5 years for BHP sensitivity (reprinted with permission from Guo et al. 2018b)

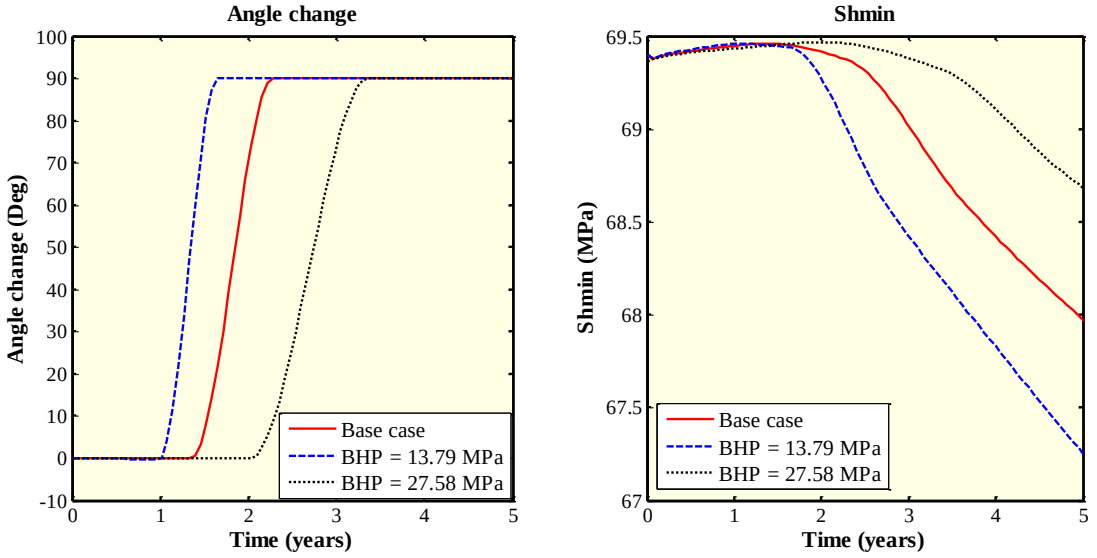

Figure 4.13. Temporal evolution monitored at X=127.5 m and Y=405 m for S_{Hmax} reorientation and S_{hmin} for BHP sensitivity (reprinted with permission from Guo et al. 2018b)

4.3.2 Parent Well Fracture Geometry

Fracture geometry along parent wells is another key parameter determining stress evolutions within the reservoir. Field data show that fracture geometry is very complex and has uncertainty (Webster et al. 2013; Ugueto et al. 2016). In order to take into account such uncertainty, several parent well fracture geometries are studied. Except for the base case geometry where the half-lengths of 150 m, 50 m, 50 m, and 150 m from left to right, another two geometries are used. The first geometry switches the locations of the shorter fractures and the longer fractures, and two inner fractures are longer. The second geometry assumes uniform fracture half-length along parent wells, and the half-length is 70 m.

Figure 4.14 shows the 2D maps of pressure, S_{Hmax} orientation and S_{hmin} for the first fracture geometry after 5 years of parent well production. Figure 4.15 shows the 2D maps of pressure, S_{Hmax} orientation and S_{hmin} for the second fracture geometry after 5 years of parent well production. The shape of the areas experiencing the most significant pressure depletion changes is altered by the change of parent well fractures. Since the S_{Hmax} orientation is always circled around the producing fractures, the orientation is also altered. Different infill location stress state changes are also observed.

Using the monitoring schemes in Figure 4.10 and Figure 4.11, 1D distributions of S_{Hmax} reorientation and S_{hmin} at 5 years along Y=405 m for three different fracture geometry cases are compared in Figure 4.16. Results show that stress is always totally reversed right at the center of the infill line, which is not affected by fracture geometry. However, the base case geometry leads to the highest overall 1D distribution of S_{Hmax} reorientation. Intermediate S_{Hmax} reorientation is obtained for the case with geometry 2 of

uniform fracture half-length. S_{hmin} at and near the center of infill line is largely decreased by geometry 2, as this geometry has longer inner fractures which lead to more pressure depletion at the center of the infill line. Geometry 2 with uniform fracture half-length leads to the highest S_{hmin} profile, as the 70 m uniform length decreases the effect of parent well production on the geomechanical behaviors along the infill line compared to the effects of fractures with half-length of 150 m. Temporal evolutions are then compared in Figure 4.17. At the observation point of X=127.5 m and Y=405 m, geometry 1 leads to the earliest beginning of stress reversal, as geometry 1 has the longest inner fractures which result in the most significant production-induced geomechanical effects at the center of the infill line. Base case has the intermediate beginning time of stress reversal. Geometry 2 has the latest beginning of stress reversal, as geometry 2 has shorter inner and outer fractures along parent wells, indicating fewer effects on geomechanical behaviors along the infill line. In addition, geometry 1 leads to a significant increase of S_{hmin} magnitude at the observation point. This is because the longer inner fractures in geometry 1 lead to increased rock deformation (increased effective stress) in the beginning when the pressure depletion caused by parent well fracture production has not affected the pore pressure at the observation point. Once parent well depletion starts to have an impact (after 1.1 years), the S_{hmin} curve starts to decline rapidly and eventually drops below the curves in the other two geometry cases. S_{hmin} curves in the other two geometry cases have similar trends. However, the base case curve is slightly lower than that of geometry 2 starting from year 3. This is because the base case has longer outer fractures (150 m) compared to geometry

2 (70 m) and the longer outer fractures contribute more to depletion once the production time is long enough.

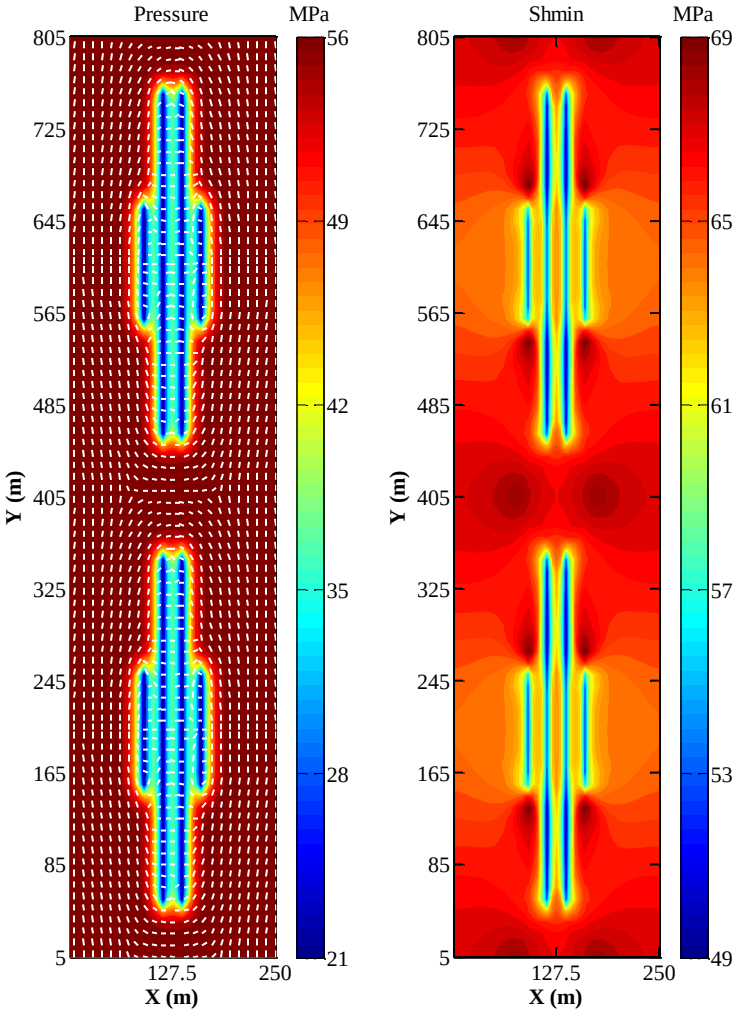

Figure 4.14. Pressure, S_{Hmax} orientation and S_{hmin} for the first geometry (reprinted with permission from Guo et al. 2018b)

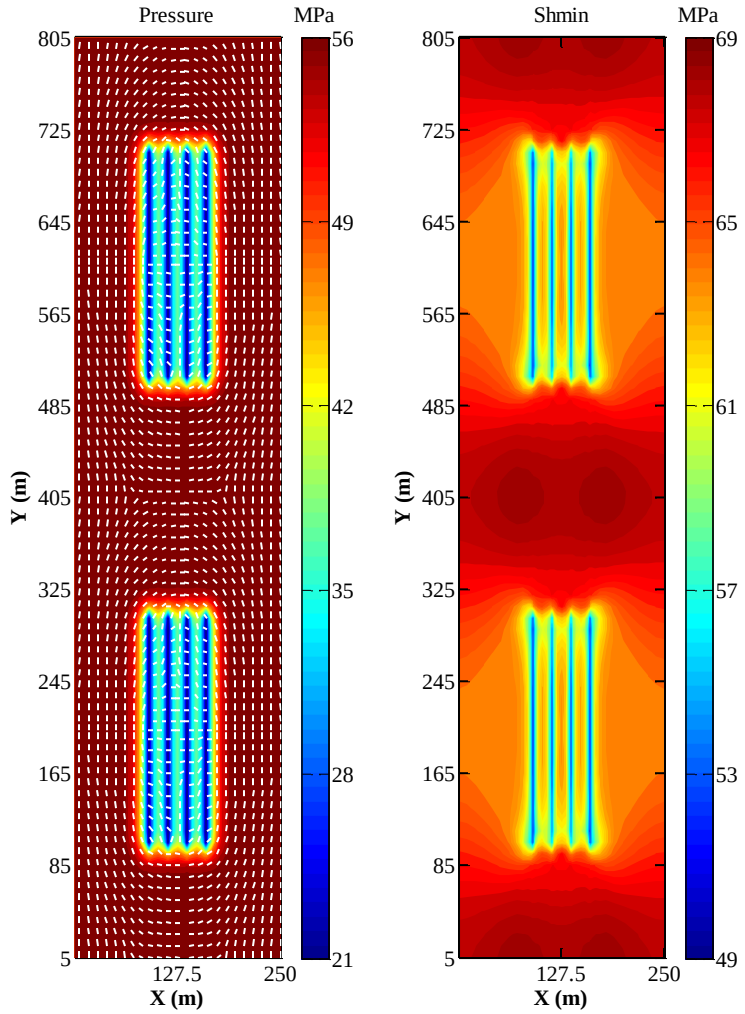

Figure 4.15. Pressure, S_{Hmax} orientation and S_{hmin} for the second geometry (reprinted with permission from Guo et al. 2018b)

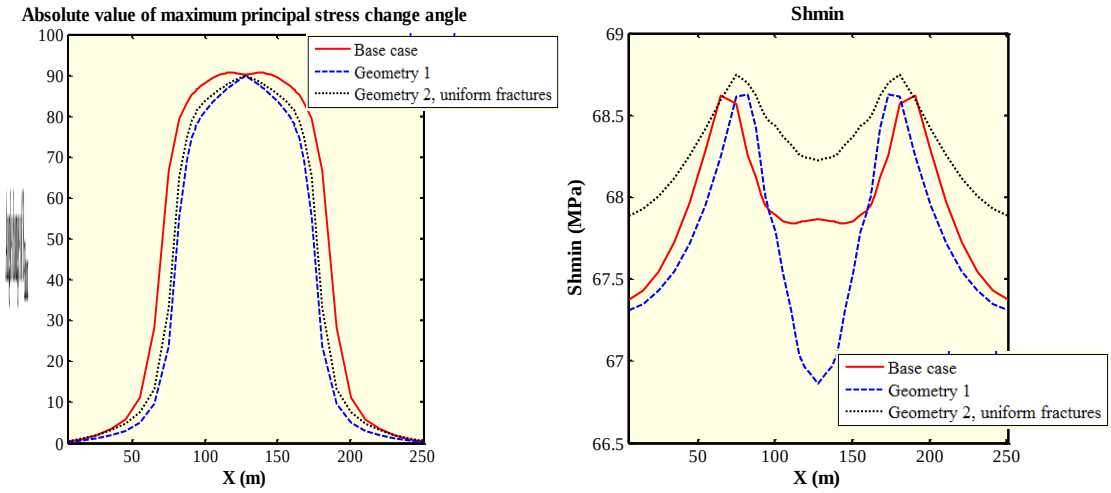

Figure 4.16. S_{Hmax} reorientation and S_{hmin} along Y=405 m at 5 years for fracture geometry sensitivity (reprinted with permission from Guo et al. 2018b)

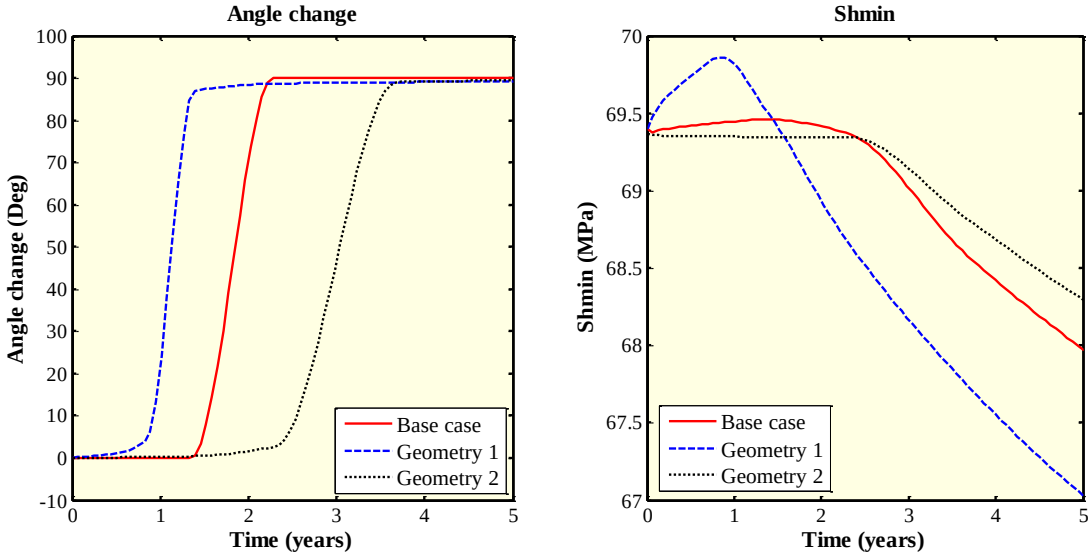

Figure 4.17. Temporal evolution monitored at X=127.5 m and Y=405 m for S_{Hmax} reorientation and S_{hmin} for fracture geometry sensitivity (reprinted with permission from Guo et al. 2018b)

4.3.3 Differential Stress

As mentioned in Section 3.2, the in-situ stress is not a key parameter for the evaluation of reservoir pressure response and well production. However, it is a key factor if stress state is the focus of the study. Therefore, the sensitivity of differential stress is analyzed in terms of how DS relates to production-induced stress changes. Here, differential stress is the stress contrast for the maximum and minimum principal stresses in the horizontal plane, or the difference between S_{Hmax} and S_{hmin}. Except for the DS of 3 MPa in the base case, another two values of 0 MPa and 6 MPa are simulated. Results after 5 years parent well production are presented.

Figure 4.18 shows that the case without any stress contrast leads to more significant stress reversal at the infill location compared to cases with stress contrast. Besides, obvious stress reversal is observed around fracture tips of the shorter inner fractures along parent wells. The S_{hmin} map indicates that the minimum principal stress magnitude becomes lower, especially in the fractured zones. This decrease is caused by the fact that the initial S_{Hmax} in this zero stress contrast case is decreased to be equal to S_{hmin}, leading to the decreased S_{hmin} magnitude updated by production-induced stress changes. Figure 4.19 shows the results for the case with DS increased to 6 MPa. It is noticed that the increased DS inhibits the reversal of stress caused by parent well production, and the S_{Hmax} orientation is still in the initial direction along the infill line. The areas experiencing stress reversal are limited to fractured zones and the adjacent areas around the producing fractures.

The 1D distributions of relevant properties at 5 years and the temporal evolution during 5 years of history are presented in Figure 4.20 and Figure 4.21. Figure 4.20 shows that zero stress contrast (DS=0 MPa) leads to the highest stress reversal profile, with the entire infill line having angle changes above 80°. It is also noted that, along the infill line, strong stress reversal is even observed near the left and right boundaries of the reservoir model. In contrast, stress reversal is insignificant for the case with DS of 6 MPa. Reorientation for this case is always below 10°. The lowest S_{hmin} curve is observed for DS of 0 MPa and the highest curve is observed for DS of 6 MPa. This is because when DS is varied in the sensitivity analysis, the initial S_{hmin} is kept constant and S_{Hmax} is changed, and the magnitude of the principal stress for DS of 6 MPa consequently becomes the largest. In Figure 4.21, property changes over time are plotted at X=127.5 m and Y=405 m. DS of 0 MPa leads to angle change from the beginning, as slight pressure disturbance can generate stress reversal if the initial in-situ stress state has no stress contrast. DS of 6 MPa leads to no stress reversal, as the magnitude of shear stress required for stress reversal is higher when the stress contrast is large. The evolution of the magnitude of S_{hmin} is also presented, with DS of 6 MPa having the highest evolution curve and DS of 0 MPa having the lowest evolution curve.

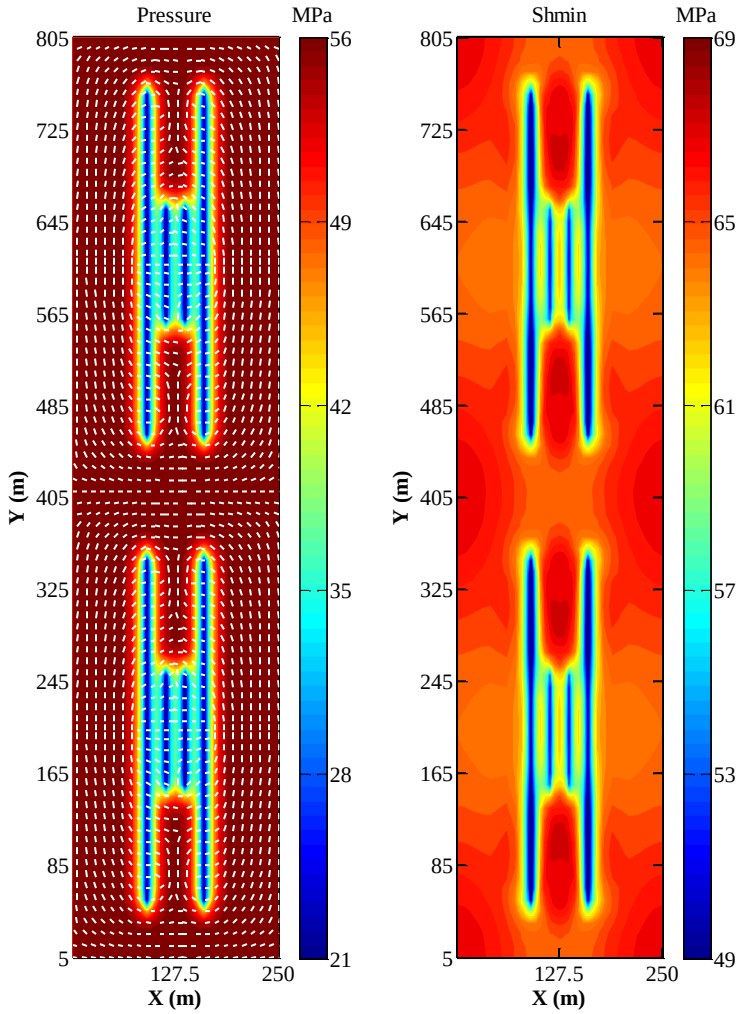

Figure 4.18. Pressure, S_{Hmax} orientation and S_{hmin} for 0 MPa DS (reprinted with permission from Guo et al. 2018b)

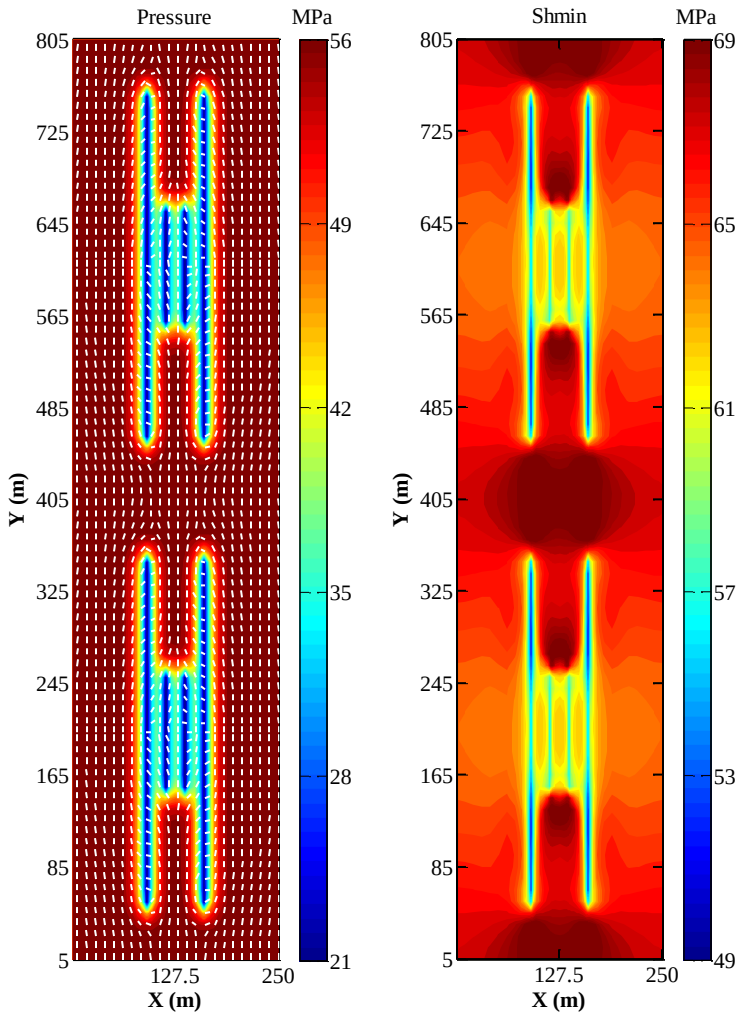

Figure 4.19. Pressure, S_{Hmax} orientation and S_{hmin} for 6 MPa DS (reprinted with permission from Guo et al. 2018b)

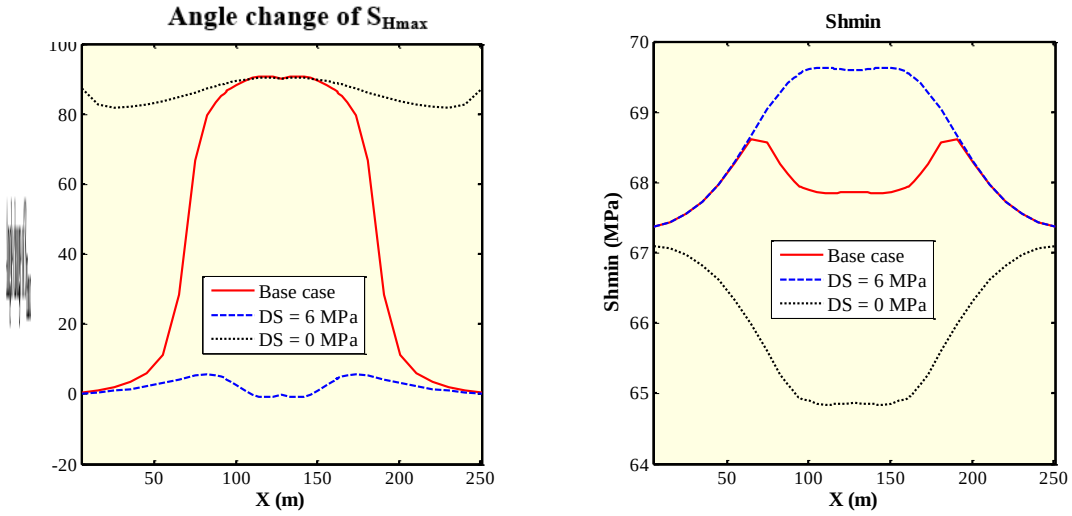

Figure 4.20. S_{Hmax} reorientation and S_{hmin} along Y=405 m at 5 years for DS sensitivity (reprinted with permission from Guo et al. 2018b)

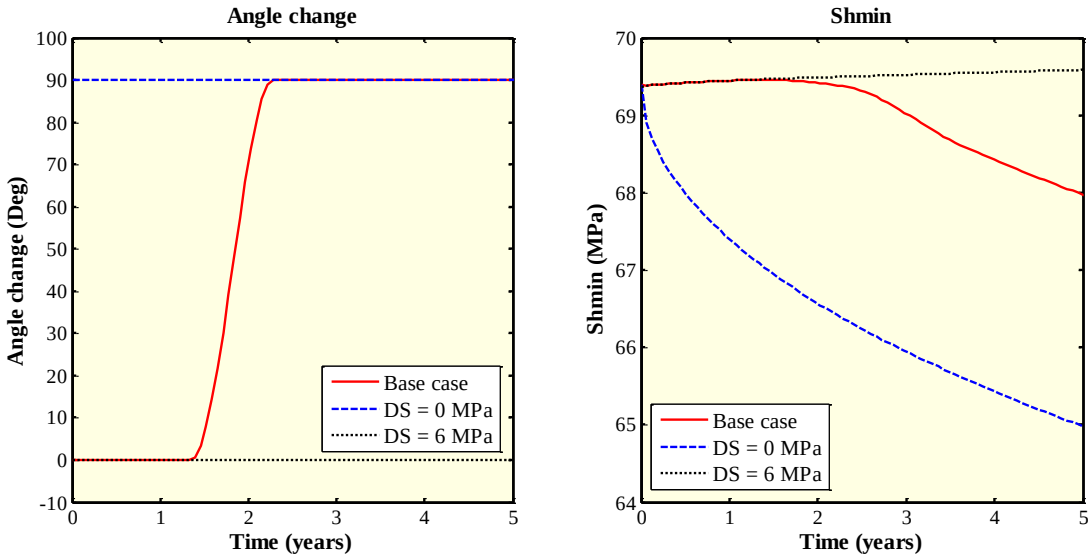

Figure 4.21. Temporal evolution monitored at X=127.5 m and Y=405 m for S_{Hmax} reorientation and S_{hmin} for DS sensitivity (reprinted with permission from Guo et al. 2018b)

4.3.4 Well Spacing

Well spacing determines the density of horizontal wells and interwell interference in a reservoir. Except for the base case well spacing of 400 m, another two values of 300 m and 350 m are simulated. Note that the longer parent well fractures' half-length is 150 m, and in the 300 m well spacing case the longer fractures of the two parent wells actually connect and form two high permeability channels connecting two parent wells.

Figure 4.22 and Figure 4.23 present the pressure, S_{Hmax} reorientation, and S_{hmin} distributions for cases with well spacing of 300 m and 350 m respectively. In Figure 4.22, the connected hydraulic fractures are clearly identified by the pressure depletion areas. Stress reorientation is obvious within the fractures. However, it is noted that along the infill line, stress is not reversed by parent well production except for the fractured zones. This is because the unfractured infill zone has highly symmetric depletion due to the enclosed fractures, reducing the degree of stress reorientation. This is in accordance with the unreversed stress reorientation between the longer outer fractures of the parent wells in the pressure and orientation results in Figure 4.7. In Figure 4.23, stress reversal is again observed along the infill line.

Figure 4.24 records the 1D distributions of S_{Hmax} reorientation and S_{hmin} magnitude along the infill line of Y=405 m after 5 years of parent well production. The temporal evolutions of S_{Hmax} reorientation and S_{hmin} magnitude at the center of the infill zone at X=127.5 m and Y=405 m are documented in Figure 4.25. The avoided stress reversal along the infill line for the case with well spacing of 300 m is further expressed by the 1D distribution: only the fractured areas and their adjacency has 90° stress reorientation, while

the rest along the infill line has zero reorientation. The case with 300 m well spacing also documents two largely depleted pressure areas due to the depletion by connected hydraulic fractures. The temporal evolution of S_{Hmax} reorientation indicates that the base case with the largest well spacing of 400 m has the earliest stress reversal. As well spacing decreases to 350 m, the beginning time of stress reversal is delayed. This is because the degree of symmetric depletion at the center of the infill zone is increased by the closer fractures. As well spacing further decreases to 300 m and parent well hydraulic fractures connect, stress reversal at the observation point is suppressed as highly symmetric pressure and stress evolutions are induced.

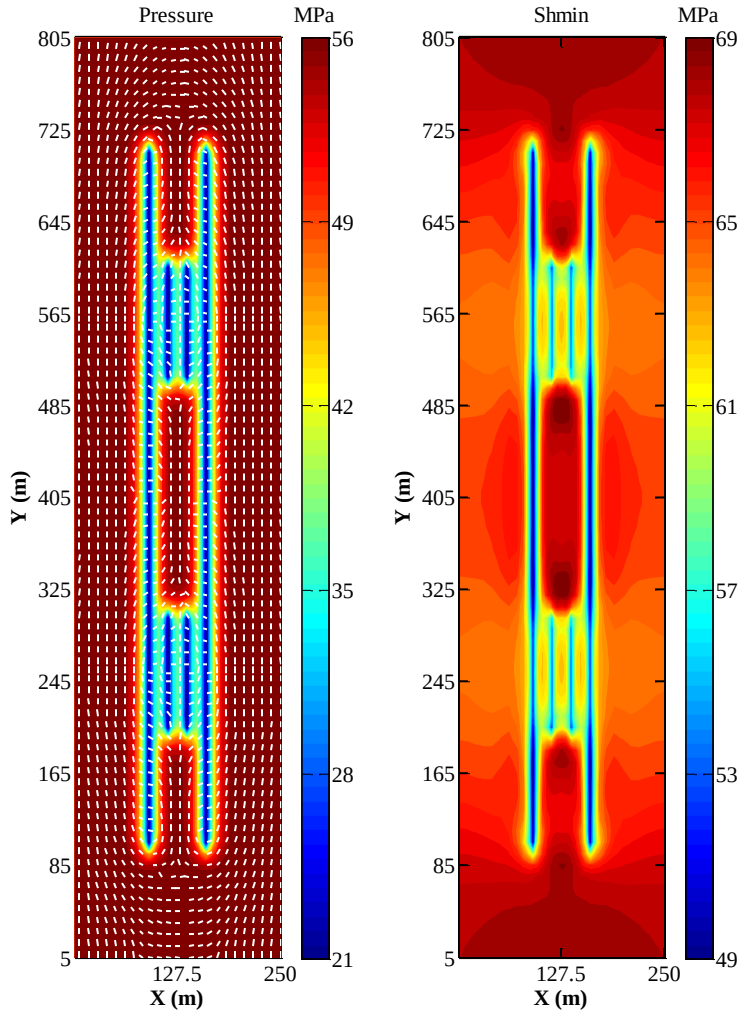

Figure 4.22. Pressure, S_{Hmax} orientation and S_{hmin} for 300 m well spacing (reprinted with permission from Guo et al. 2018b)

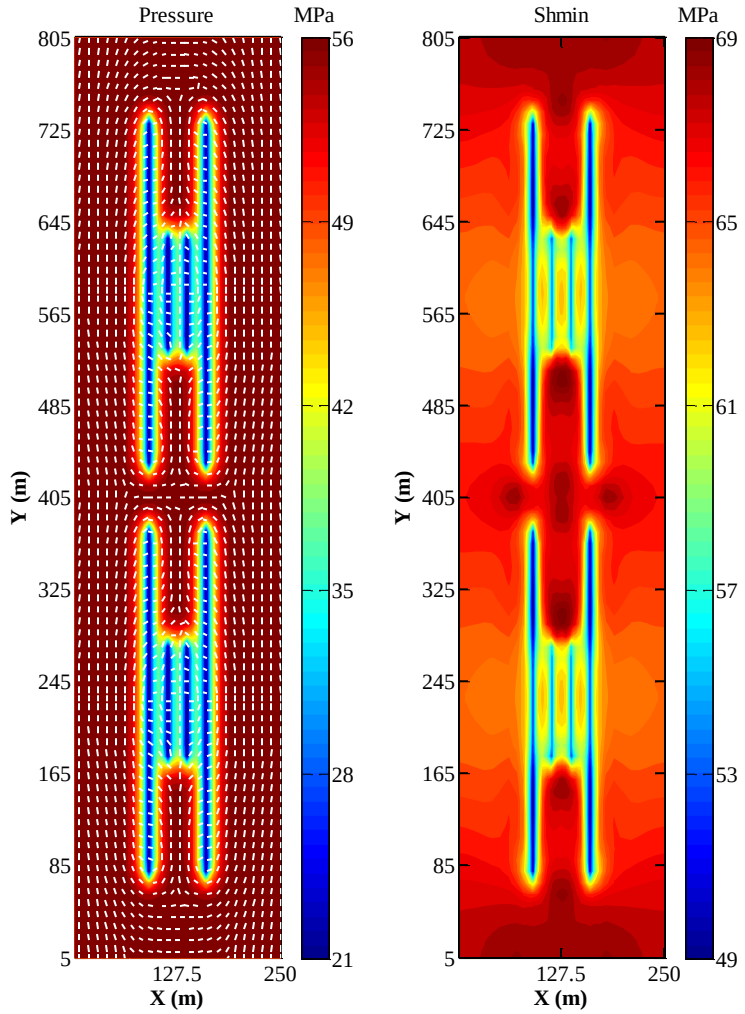

Figure 4.23. Pressure, S_{Hmax} orientation and S_{hmin} for 350 m well spacing (reprinted with permission from Guo et al. 2018b)

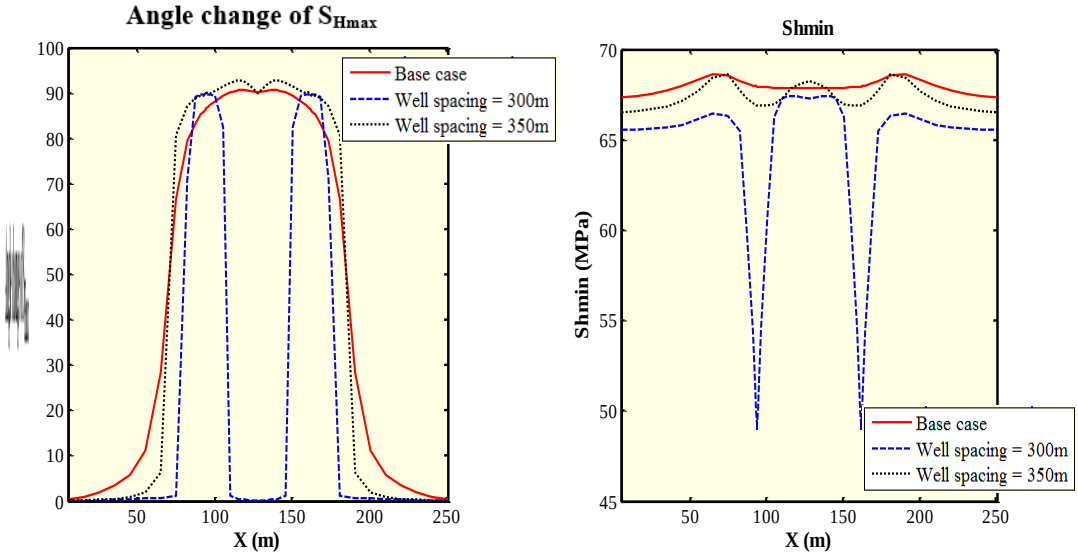

Figure 4.24. S_{Hmax} reorientation and S_{hmin} along Y=405 m at 5 years for well spacing sensitivity (reprinted with permission from Guo et al. 2018b)

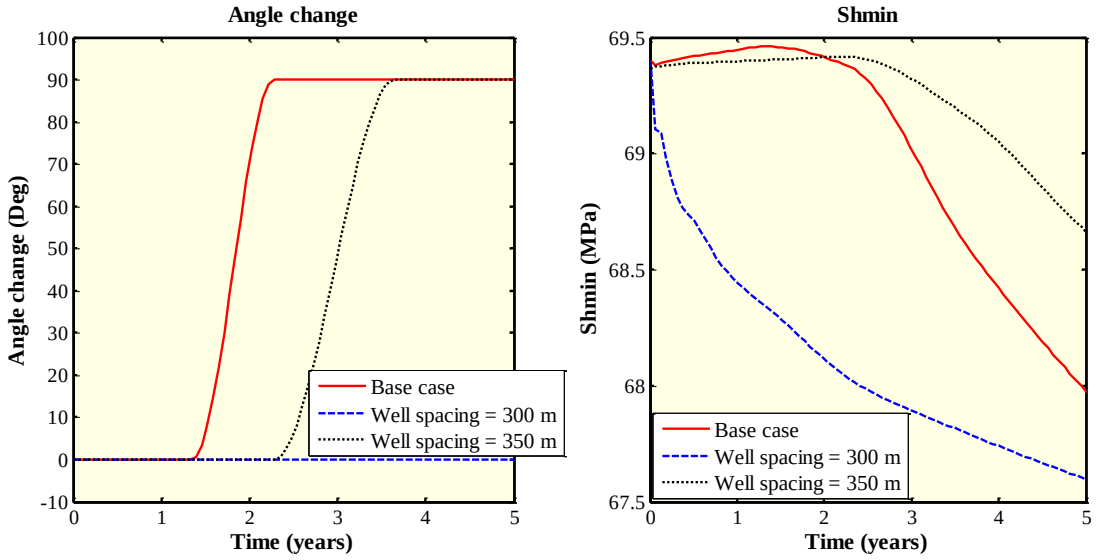

Figure 4.25. Temporal evolution monitored at X=127.5 m and Y=405 m for S_{Hmax} reorientation and S_{hmin} for well spacing sensitivity (reprinted with permission from Guo et al. 2018b)

4.3.5 Young's Modulus

Young's modulus is the last parameter that is investigated. Apart from the base case value of 20 GPa, another two values of 10 GPa and 30 GPa are simulated. Using the same observation scheme for 1D distribution and temporal evolution, Figure 4.26 shows the results of this sensitivity analysis. Young's modulus has insignificant effects on the stress reversal and stress magnitude evolution in this study.

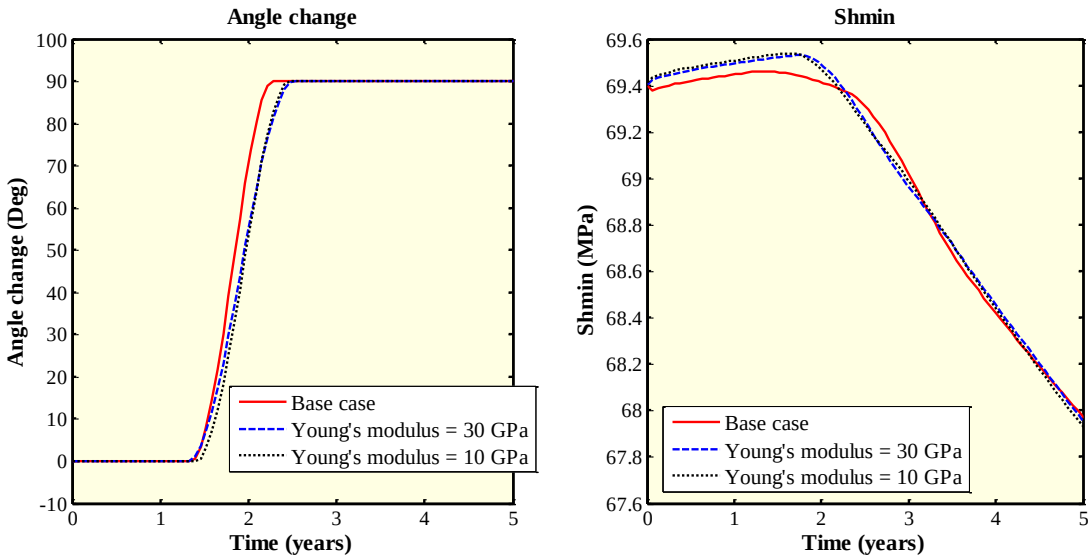

Figure 4.26.S_{Hmax} reorientation and S_{hmin} along Y=405 m at 5 years for Young's modulus sensitivity (reprinted with permission from Guo et al. 2018b)

4.4 Conclusions and Recommendations

Hydraulic fracture propagation in the infill location can be largely affected by pressure, S_{Hmax} reorientation, and S_{hmin} magnitude. This study indicates that certain

parameters can remediate or aggravate stress reversal at infill locations. Strong stress reversal can lead to largely longitudinal fractures in the completion of the infill well, decreasing interwell interference between parent and infill wells. Weak stress reversal leads to the transverse growth of hydraulic fracture in the completion of the infill well. This generates strong interwell interference. Further investigation including detailed hydraulic fracture modeling is considered in the next section so that interwell interference can be studied based on the interwell fracture networks.

Based on the fully coupled flow and geomechanics modeling and the numerical results presented in this section, some conclusions are drawn as follow.

(1) Parent well operation and reservoir properties are key parameters influencing the magnitude and orientation of principal stresses around producing fractures and at the infill location.

(2) Significant stress reversal at the infill location can be obtained by decreasing the parent well BHP. Decreased differential stress leads to faster stress reversal at the infill location.

(3) Along the infill line, areas closer to parent well fracture tips experience faster stress reversal and greater S_{hmin} decrease.

(4) If the well spacing is small enough and the parent well fractures connect, S_{Hmax} orientation is totally reversed in the fractured zones and it is not reversed outside fractured zones along the infill line.

Some recommendations are presented based on the numerical results in this section. However, they should not be generalized as they are based on the data and model in this study.

In the first place, stress reversal at the observation point is usually completed in the first 5 years of parent well production. To decrease the effect of production-induced stress reversal at the infill location, the completion of the infill well can be conducted before the total stress reversal. For the base case in the numerical study, infill well should be completed before 2 years of parent well production since stress is totally reversed after 2 years of parent well production. This critical time for stress reversal changes if values of relevant parameters change.

Second, when frac hits occur as the longer parent well fractures connect, stress reversal in the unfractured areas along the infill line is inhibited and suppressed. If the infill well is completed, these areas would expect transverse fractures which can contact the unproduced interwell zones. This is also the desirable fracture geometry with fractures growing in the direction of initial S_{Hmax}. This implies that the completion quality at an infill location with known fracture communication can be good.

Finally, the initial placement of parent wells and their spacing are key parameters affecting interwell interference and field performance. Very large parent well spacing decreases the influence of parent well production on stress changes at the infill location. However, the numerical results show that small spacing is also acceptable if there are known fracture communication between parent wells. Furthermore, small well spacing

indicates high well density and great depletion potential of the reservoir, which is good for the improvement of the economics of the project.

5 INTERWELL FRACTURING INTERFERENCE

5.1 Introduction

In this section, in addition to the modeling of stress and pressure evolution at the infill location, hydraulic fracturing modeling is carried out so that the interwell hydraulic fracturing interference can be characterized by the fracture network consisting of parent well fractures and hydraulic fractures propagated along the infill well based on updated infill zone stress states. The study in this section is the continuation of the study presented in Section 4, as Section 4 does not consider the modeling of hydraulic fractures along the infill well while Section 5 considers hydraulic fractures along the infill well in the sensitivity analyses. This study provides insights on the infill well completion designs based on simulation of Eagle Ford scenarios. The coupled flow and geomechanics modeling is based on the model in Section 2.1.

A numerical modeling workflow is established and used in this section to examine the role reservoir geomechanics plays in the determination of infill well completion quality. The numerical modeling workflow consisting of reservoir, geomechanics, and fracturing is shown in Figure 5.1.

Inputs for the reservoir and geomechanics model are first incorporated. Parent well information is also used for the establishment of the model. Then, history production of parent wells is used for history matching as in Section 4.2. Once the reservoir geomechanics model is calibrated, 3D coupled simulation is carried out to provide the pressure and stress fields updated by parent well production. These updated pressure and

stress fields are then used as inputs for the hydraulic fracture model so that hydraulic fractures along the infill well are characterized. The interwell hydraulic fractures are the final output of the numerical modeling workflow which can be used to examine interwell fracturing interference in the reservoir developed by tightly spaced horizontal wells.

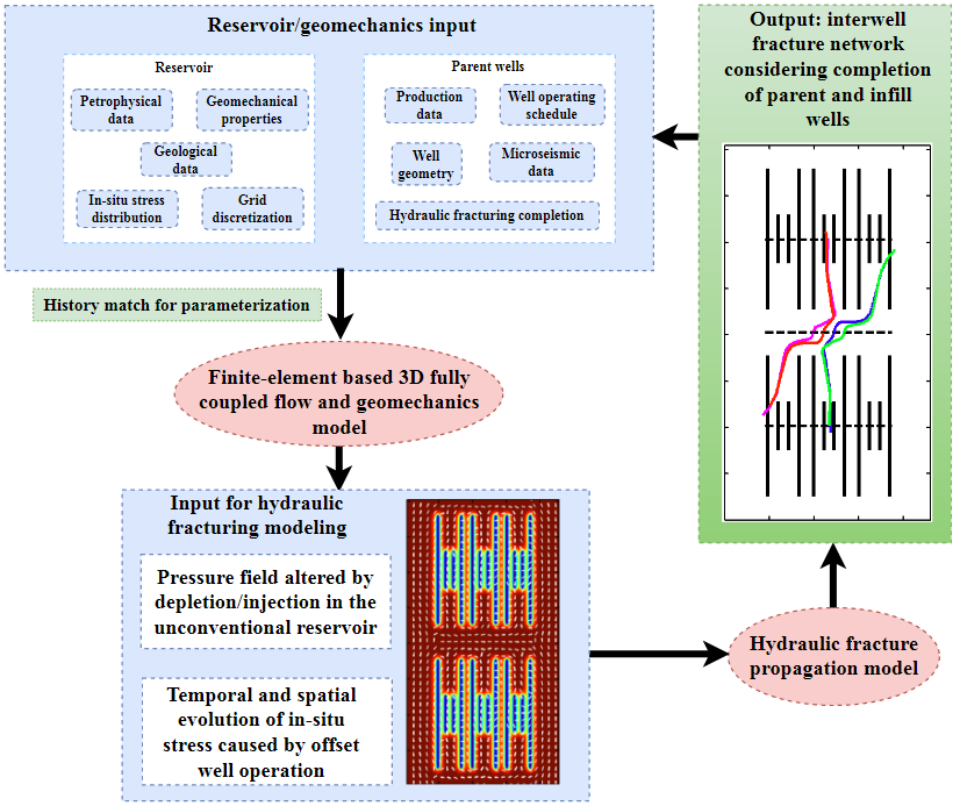

Figure 5.1. Workflow of the reservoir-geomechanics-fracturing numerical modeling workflow

5.2 Hydraulic Fracture Model

Proper modeling for the growth of hydraulic fractures along the infill well in the updated heterogeneous pressure and stress fields is a key component of the numerical modeling workflow presented in Figure 5.1.

In this study, an in-house fracture propagation model is used (Wu and Olson 2015a). The model can simulate the simultaneous growth of multiple fractures and it couples rock deformation with fluid flow in the horizontal wellbore and hydraulic fractures. The numerical model uses a simplified 3D displacement discontinuity method to calculate fracture opening, shearing, and stress shadow effects for single-fracture and multiple-fracture growth cases (Wu and Olson 2015b). The fluid flow in the fracture and the pressure drop caused by this fluid flow are modeled by the lubrication theory, with the assumption that the fracture is analogous to a slot between parallel plates and that the fluid is non-Newtonian. Another assumption made in this fracture model is that the total fracturing fluid injection into the horizontal wellbore is constant, and the distribution of flow rates in each fracture is dynamically calculated. In the calculation pressure in wellbore gradually decreases along the wellbore lateral due to the wellbore friction. The analysis of induced stresses at fracture tips is incorporated so that the interaction of hydraulic and natural fractures is modeled. If natural fractures are considered in the model, stochastic realizations are generated for the description of natural fracture patterns. This model is validated with known analytical solutions for the growth of single hydraulic fractures (Olson and Wu 2012). The model is also validated with numerical solutions from

Wu et al. (2012) for the physical processes of fracture interaction in multiple fracture propagation cases.

Two Eagle Ford reservoir models are constructed for the numerical analysis in this section. Reservoir parameters are calibrated in history matching in Section 4. The first reservoir model conceptually shows the parent wells using constant fracture half-length and SRV treatment for grid blocks within fractures. Fractures are sparsely distributed along wellbores. The second reservoir model has denser fractures along parent wells and fracture half-lengths are not uniform. Dense fractures explicitly represent parent well completion and no SRV is used in the mesh.

Five parameters are covered: parent well fracture geometry (uniform or non-uniform fracture half-lengths), timing of infill well completion (after 1, 5, or 10 years of legacy production), differential stress (1, 3, and 5 MPa), fracturing interference, and perforation cluster location.

5.3 Uniform Parent Well Fractures

The geometry of the first model conceptually showing the parent well completion is sketched in Figure 5.2. The parameters used for this model are in Table 5.1. Figure 5.2 shows that each parent well has six sparsely distributed fractures with a spacing of 100 m. Parent well spacing is 400 m. Overburden and sideburden stresses are exerted as indicated. Correspondingly, the detailed fluid, reservoir, and geomechanics parameters are in Table 5.1

Parameter	Value
Reservoir size	2100 m × 1062 m × 15 m
Fracture half-length	100 m
Fracture spacing	100 m
Well spacing	400 m
Fracture number of each parent well	6
Matrix permeability	4.6×10^{-19} m^2 (470 nD)
SRV permeability	2.3×10^{-18} m^2 (2350 nD)
Porosity	0.12
Young's modulus	20 GPa
Poisson's ratio	0.22
Biot's coefficient	0.7
Initial pore pressure	56.02 MPa
Well BHP	20.7 MPa
Oil viscosity	3×10^{-4} Pa·s
Water viscosity	6×10^{-4} Pa·s
Overburden stress	75 MPa
Maximum horizontal stress	68 MPa
Minimum horizontal stress	65 MPa
Differential stress (base case)	3 MPa

Table 5.1. Parameters for the first reservoir model with constant fracture half-length

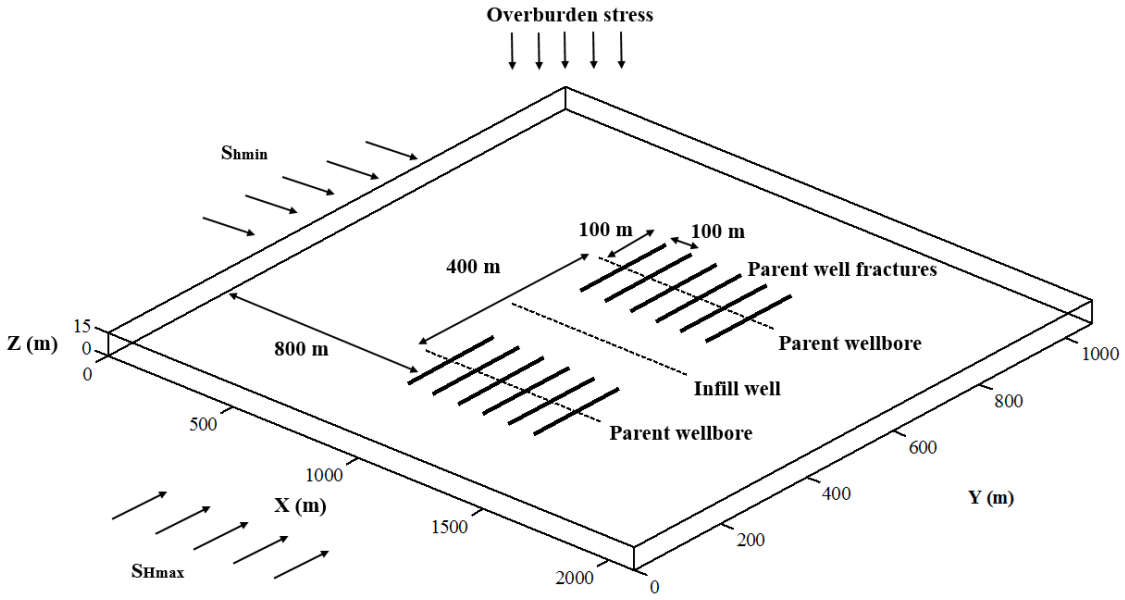

Figure 5.2. Geometry of the first reservoir model

5.3.1 Effects of Legacy Production and Differential Stress

Three parent well legacy production times (1, 5, and 10 years) and three different DS values (1, 3, and 5 MPa) are simulated. These times also indicate the timings of infill well completion. Figure 5.3 shows the pressure and S_{Hmax} orientation distributions at three different production times under DS of 1 MPa, and the corresponding S_{Hmax} reorientation angle along the infill line at Y=531 m. Figure 5.4 shows the same results under DS of 3 MPa. Figure 5.5 shows the results under DS of 5 MPa.

Figure 5.3 shows that the small DS leads to significant S_{Hmax} reversal at the infill location. Three different legacy production cases all obtain largely reversal S_{Hmax} at the infill location. The line plot shows that the increase of legacy production from 1 year to 5 years leads to a greater increase of S_{Hmax} reorientation profile than the increase of legacy

production from 5 years to 10 years. The increase of legacy production time in parent wells increases the degree of S_{Hmax} reversal at the infill location.

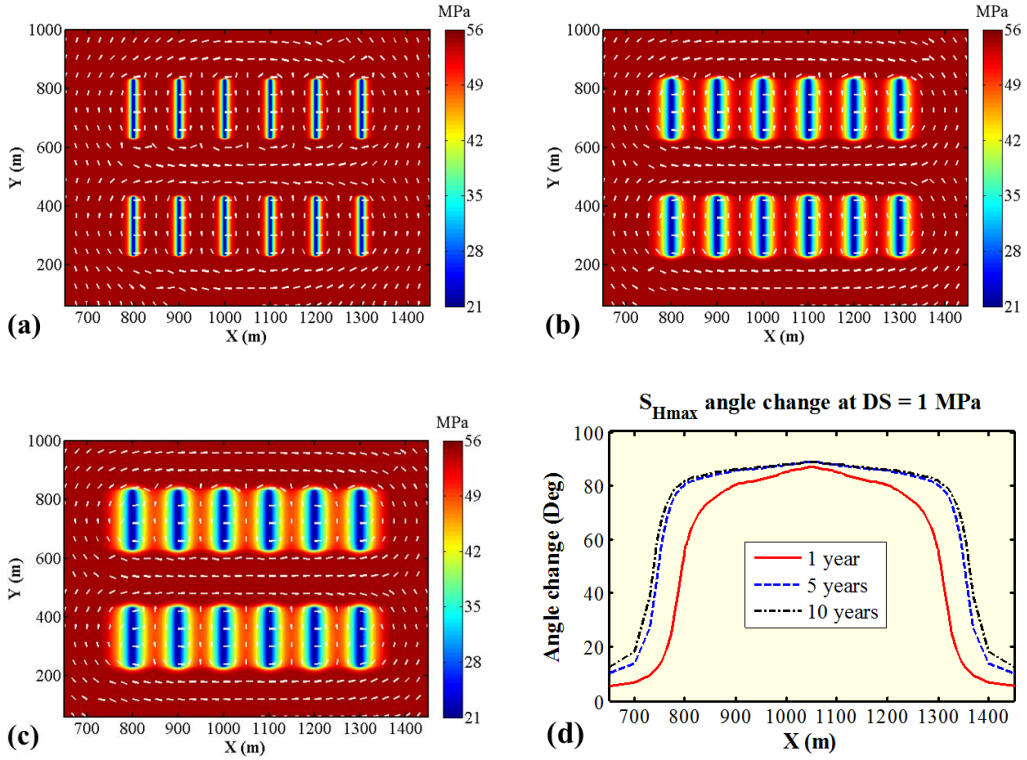

Figure 5.3. Pressure and S_{Hmax} orientation at (a) 1 year, (b) 5 years, and (c) 10 years for differential stress = 1 MPa; (d) S_{Hmax} angle change along the infill line at Y = 531 m

Figure 5.4 shows that the intermediate DS alleviates the stress reversal of S_{Hmax} for the case with 1 year legacy production. In the 1 year legacy production result, stress reversal can be hardly observed and S_{Hmax} is generally in the initial direction. When the legacy production of parent wells increases to 5 years, S_{Hmax} reorientation becomes more

significant in the infill zone. As it further increases to 10 years, largely reversed S_{Hmax} is again obtained at the infill location. This is substantiated by the line plot comparing the three S_{Hmax} reorientation profiles along the infill line. Compared to the line plot in Figure 5.3d, the greatest difference is observed for the 1 year profile: its maximum reorientation in Figure 5.3d is above 80° while it is lower than 10° in Figure 5.4d due to the increased DS.

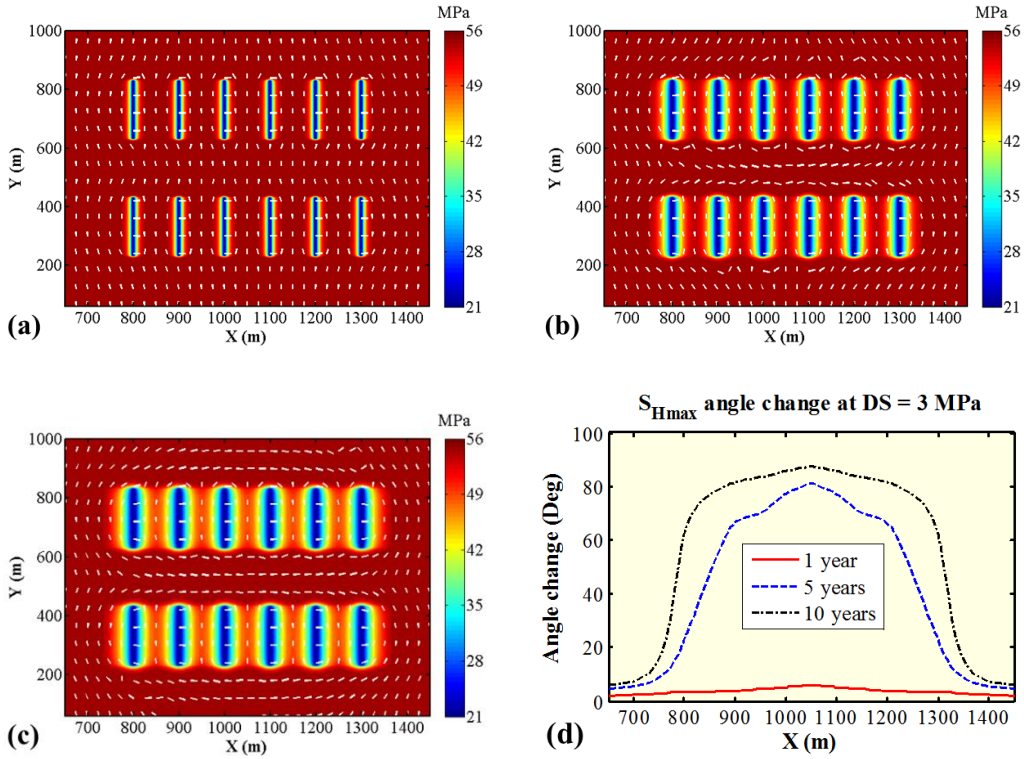

Figure 5.4. Pressure and S_{Hmax} orientation at (a) 1 year, (b) 5 years, and (c) 10 years for differential stress = 3 MPa; (d) S_{Hmax} angle change along the infill line at Y = 531 m

Figure 5.5 shows the results with large DS. The increased DS significantly inhibits the stress reversal caused by parent well production. Even in the case with 10 years of parent well legacy production, the maximum recorded S_{Hmax} reorientation angle along the infill line is still below 40°.

Based on Figure 5.3 to Figure 5.5, some general trends are observed. Large DS and small parent well legacy production time both help to suppress stress reversal. Additionally, the effects of legacy production and DS on stress reversal at the infill location are primarily limited to the width between 750 m and 1350 m in X direction which corresponds to the completion width of parent wells.

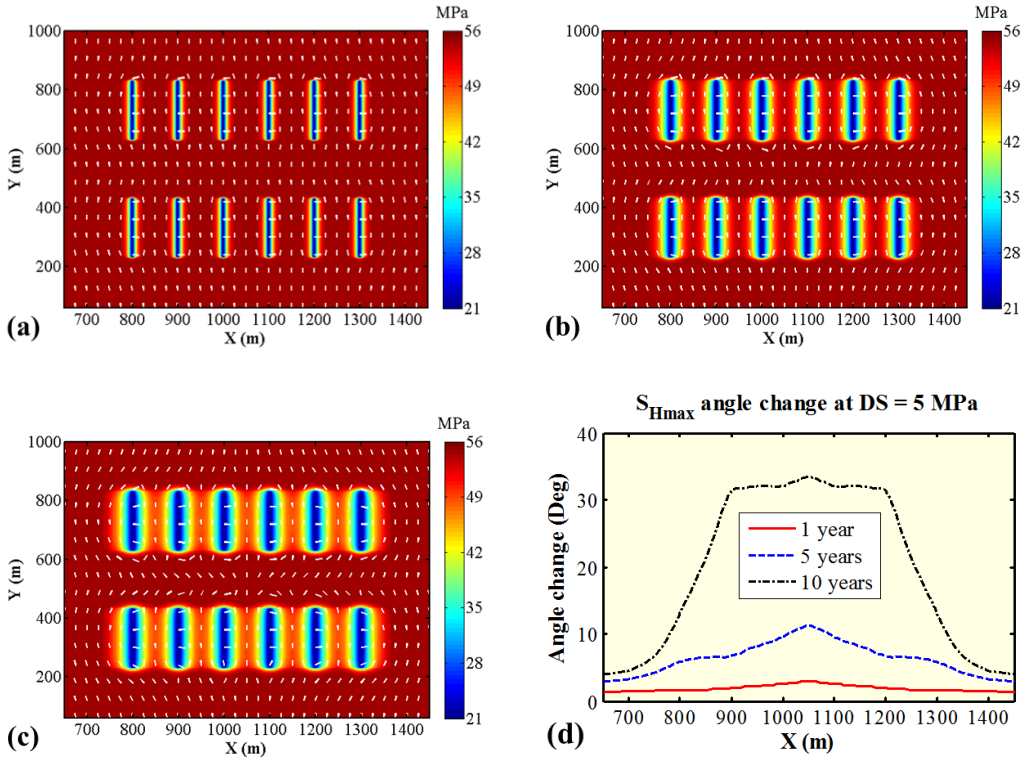

Figure 5.5. Pressure and S_{Hmax} orientation at (a) 1 year, (b) 5 years, and (c) 10 years for differential stress = 5 MPa; (d) S_{Hmax} angle change along the infill line at Y = 531 m

5.3.2 Modeling of Interwell Fractures

Heterogeneous stress updating obtained in Section 5.3.1 is then used as inputs for the hydraulic fracture model to simulate the fracture propagation along the infill well. It is usually assumed that the S_{Hmax} orientation (white dashed lines in the figures) can be used as a proxy for hydraulic fracture propagation path (Safari et al. 2017). However, the use of a robust fracture model for the simulation of fracture propagation path can provide detailed numerical results for comprehensive analysis.

Two types of fracture modeling are included here: the first type of analysis only considers the propagation of individual fractures, excluding the effect of fracturing interference. Thus, the effect of perforation cluster location on propagation path can be better presented. The second type of analysis considers the simultaneous propagation of multiple fractures along the infill well and emphasizes on the interference between infill well fractures during the completion.

Table 5.2 records the parameters for the pumping of fractures along the infill well in the hydraulic fracture model. Note that there is an 80° angle between the initial fracture and the horizontal wellbore. This practice is used to ensure the simulated fracture can be diverted by the stress reversal at the infill location. If 90° is used, the totally reversed stress can have no effects on diverting the fracture to longitudinal directions. This practice is also used in Roussel et al. (2013) and Safari et al. (2017). A spacing of 50 m is used to separate fractures along the infill well.

Parameter	**Value**
Pumping time	15 minutes
Injection rate	0.159 m^3/s
Leak-off coefficient	0.00001 $m/s^{0.5}$
Angle between initial fracture and wellbore	80°
Slurry density	1010 g/cm^3

Table 5.2. Parameters for the hydraulic fracture model

In order to quantify the effects of relevant parameters on infill well completion quality, a value called transverse percentage is defined as $\frac{l_t}{l_f}$ where l_t is the infill well fracture growth in the transverse direction (Y direction), and l_f is the total length of an infill well fracture. A large $\frac{l_t}{l_f}$ close to one indicates a very transverse fracture and large interference between parent and infill well productions. A small $\frac{l_t}{l_f}$ indicates a longitudinal fracture, less parent/infill well interference, and low hydrocarbon extraction potential for the infill well.

The fracture simulation results considering only individual fracturing are shown in Figure 5.6 (based on stress and pressure in Figure 5.3), Figure 5.7 (based on stress and pressure in Figure 5.4), and Figure 5.8 (based on stress and pressure in Figure 5.5).

Figure 5.6 indicates that under differential stress of 1 MPa, infill well fractures become more longitudinal as the legacy production time of parent wells increases. The infill fractures still have partial transverse growth for 1 year of legacy production, while infill fractures are totally longitudinal as legacy production increases to 5 years and 10 years. The highly longitudinal fractures in Figure 5.6b and Figure 5.6c imply very limited stimulation effectiveness of the infill well and insignificant interwell interference between parent wells and the completed infill well. The transverse percentages of the five infill well fractures drop from around 45% to around 10% as legacy production increases from 1 year to 10 years. Perforation cluster locations (fractures 1-5) do not have a significant effect on the transverse percentage. Note that the drop between 5-year and 10-year legacy productions is insignificant, which is in accordance with the observations in Figure 5.3d.

This accordance proves that although the S_{Hmax} orientation denoted by white dashed lines in the results of this study could not provide accurate fracture propagation path, they can approximately demonstrate the general trend and quality for the fracturing paths.

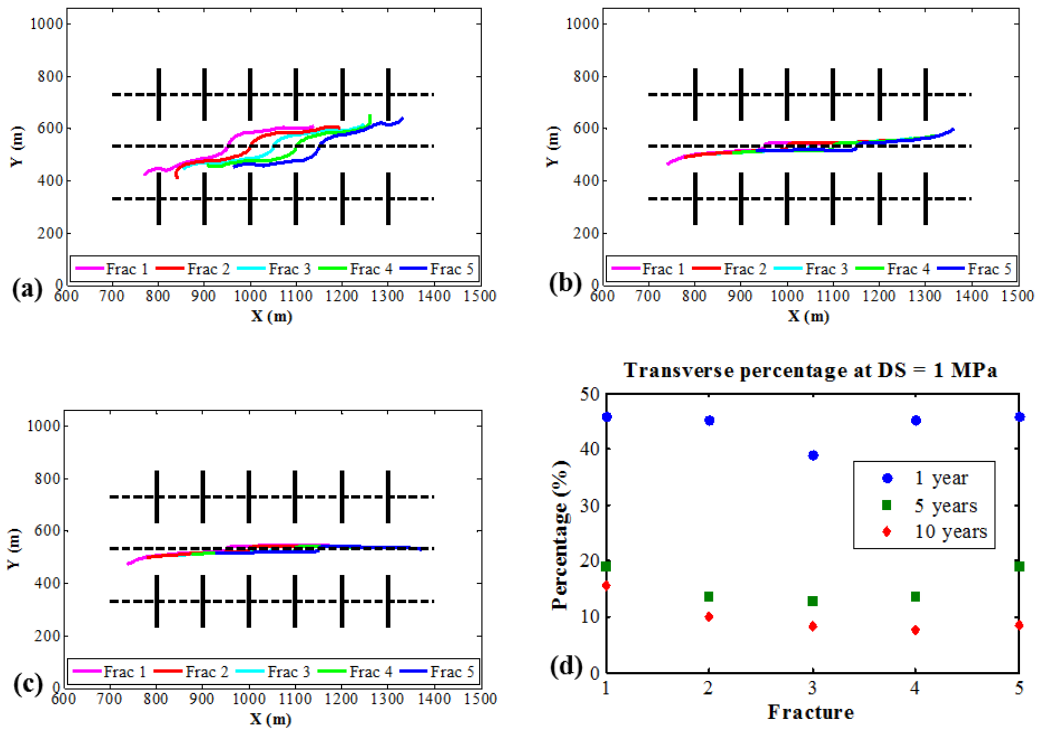

Figure 5.6. Infill well fracture propagation paths after legacy production in parent wells for (a) 1 year, (b) 5 years, and (c) 10 years with differential stress of 1 MPa; (d) the transverse percentages of infill well fractures; infill well fractures are individually modeled

Figure 5.7 shows that if DS increases to 3 MPa, infill well fractures become more transverse. 1-year and 5-year legacy production cases both have transverse growth of infill well fractures, and only the 10-year legacy production case leads to largely longitudinal

infill well fractures. Transverse percentages increase significantly compared to those in Figure 5.6: infill well fractures for 1-year and 5-year legacy production cases have transverse percentages around 100% and around 90% respectively. In Figure 5.7d, the decrease of transverse percentages from 1-year to 5-year legacy production is insignificant compared to this decrease from 5-year to 10-year legacy production, which does not entirely follow the trend for S_{Hmax} reorientation decreases in Figure 5.4d. It is because Figure 5.4d focuses on the stress reversal state along the infill line and does not cover the areas outside the infill zone. However, infill well fractures actually grow outside the infill location and propagate to areas adjacent to parent well fractures. Since stress is not largely reversed near parent well fractures, transverse propagation is obtained which increases the transverse percentages for the five fractures in Figure 5.7b. Additionally, in Figure 5.7a, infill well fractures are nearly ideally transverse except for fractures 2 and 4. This is because fractures 2 and 4 propagate near parent well fracture tips, and tips of producing hydraulic fractures usually serve as fracture diverters (Gupta et al. 2012; Roussel et al. 2013; Safari et al. 2017). Figure 5.7a and Figure 5.7b also show that varying the location of perforation cluster has an impact on the resulting shape of the infill well fracture in certain cases.

Figure 5.8 shows that as DS is increased to 5 MPa, infill well fractures in all three legacy production cases are largely transverse with transverse percentages greater than 90%. This indicates a decreased effect of legacy production time on infill well fracture shapes compared to those in Figure 5.6 and Figure 5.7.

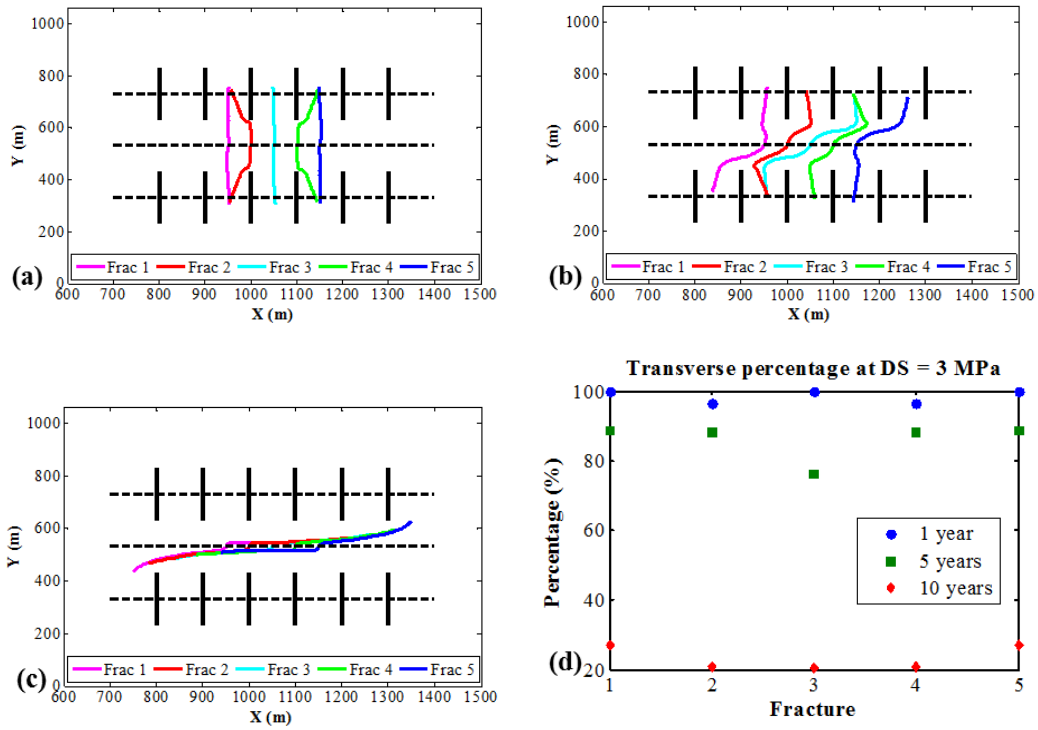

Figure 5.7. Infill well fracture propagation paths after legacy production in parent wells for (a) 1 year, (b) 5 years, and (c) 10 years with differential stress of 3 MPa; (d) the transverse percentages of infill well fractures; infill well fractures are individually modeled

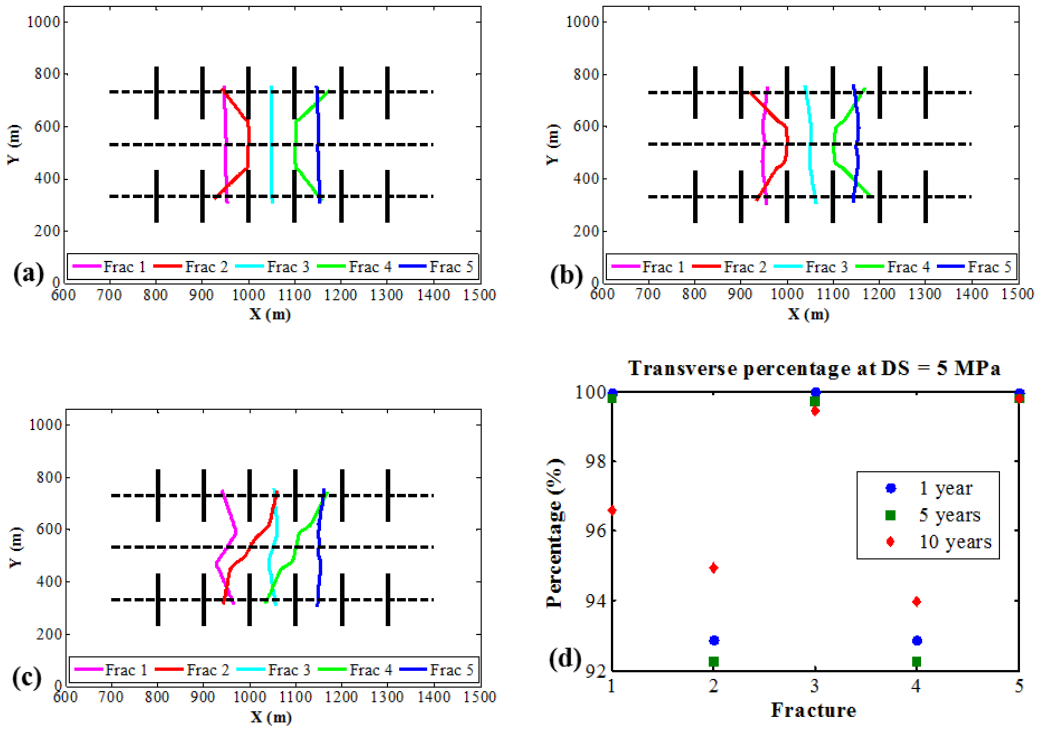

Figure 5.8. Infill well fracture propagation paths after legacy production in parent wells for (a) 1 year, (b) 5 years, and (c) 10 years with differential stress of 5 MPa; (d) the transverse percentages of infill well fractures; infill well fractures are individually modeled

After the investigation of individually propagated infill well fractures, the effect of fracturing interference is studied in the modeling of simultaneously growing multi-fracture propagation along the infill well. Here, the effect of fracture spacing is the only parameter that is considered. In this investigation, the legacy production time of parent wells is 1 year and the differential stress is 1 MPa (Figure 5.3a). Three fractures are simultaneously propagated along the infill well, with three fracture spacing values of 10 m, 30 m, and 50 m simulated. The fracturing results are in Figure 5.9, Figure 5.10, and Figure 5.11 respectively. In each simulation, the multi-fracture propagation results are

compared to results of individual fracture simulation. The comparison helps to better present the effect of fracturing interference on infill well fractures.

Based on the results, the growth of the center fracture is limited by the growths of the two adjacent fractures. A greater fracture spacing allows for more growth of the central fracture. The central fracture becomes more transverse as fracture spacing increases, which is caused by the decreased stress shadow effect. Besides, since the growth of the central fracture is terminated as it hits the two adjacent fractures, injection fluid goes to the adjacent fractures and increases their length. Thus, two outer fractures hit parent wellbores. Note that when outer fractures propagate near parent well fractures, they propagate in the initial S_{Hmax} direction due to the unreversed local stress states.

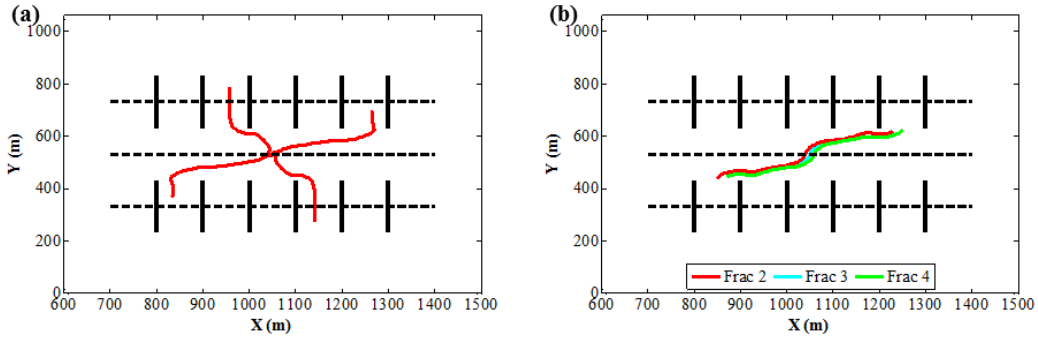

Figure 5.9. Infill well fracturing comparison between (a) multi-fracture propagation and (b) individual fracture propagation as a reference for 1 year parent well legacy production and 1 MPa differential stress for a fracture spacing of 10 m along the infill well

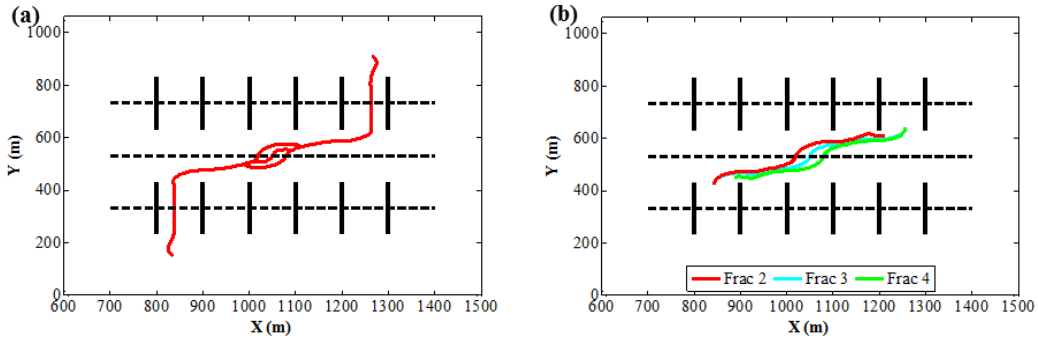

Figure 5.10. Infill well fracturing comparison between (a) multi-fracture propagation and (b) individual fracture propagation as a reference for 1 year parent well legacy production and 1 MPa differential stress for a fracture spacing of 30 m along the infill well

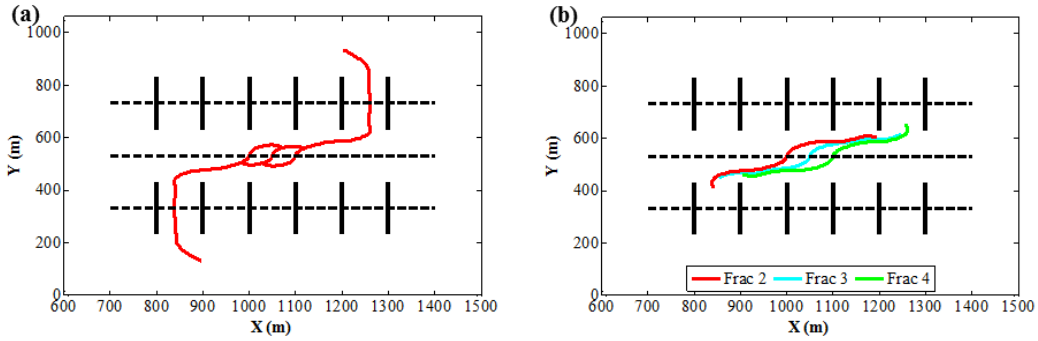

Figure 5.11. Infill well fracturing comparison between (a) multi-fracture propagation and (b) individual fracture propagation as a reference for 1 year parent well legacy production and 1 MPa differential stress for a fracture spacing of 50 m along the infill well

5.4 Non-Uniform Parent Well Fractures

The non-uniform parent well fracture half-lengths are then considered in the second reservoir model (Figure 5.12). This model considers denser parent well fractures

with non-uniform fracture half-lengths. Fractures are explicitly represented by LGR cells and no SRV modification is used.

There are two motivations for the consideration of the second model. First, field data and relevant modeling studies suggest that parent well fractures usually have very complex shapes, and the stress shadow contributes to these shapes in realistic cases (Webster et al. 2013; Wheaton et al. 2014; Ugueto et al. 2016). As a result, it makes more sense to incorporate such non-uniform fracture geometries to reflect the realistic observations from field data. Second, the capture of the occurrence of frac hits is important for a modeling workflow consisting of reservoir, geomechanics, and fracturing. However, as noted in the study in Section 5.3 assuming uniform parent well fractures, no frac hits can be captured by the modeling setup. The assumption of uniform parent well fractures also makes it hard to capture frac hits in other works (Rezaei et al. 2017a; Rezaei et al. 2017b). Consequently, the assumption of uniform fractures is excluded in this model as an attempt to capture frac hits in the numerical results.

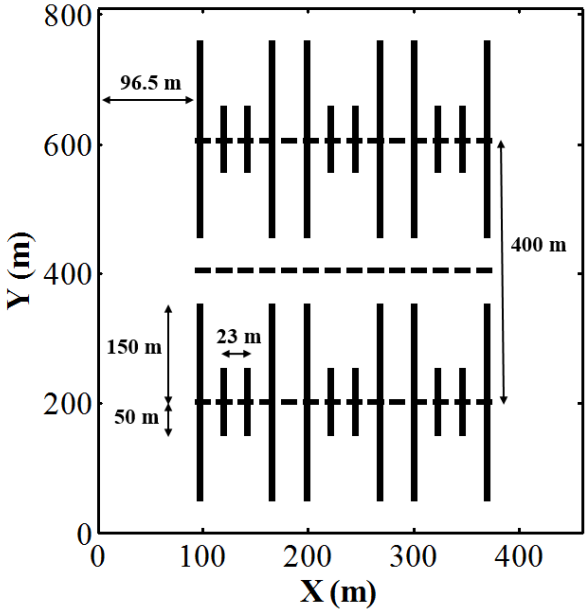

Figure 5.12. Geometry of the second reservoir model with non-uniform fracture half-lengths

5.4.1 Effects of Legacy Production and Differential Stress

Similar to the analysis in the first model, pressure and stress reorientation results for various parent well legacy production times and differential stresses are simulated. Figure 5.13 shows the pressure and S_{Hmax} orientation after 1 year, 5 years, and 10 years of legacy productions under differential stress of 1 MPa. Figure 5.14 shows these results under differential stress of 3 MPa. Figure 5.15 shows these results under differential stress of 5 MPa.

In Figure 5.13, when DS is as low as 1 MPa, the effect of legacy production is not very significant as the stress reorientation profiles along the infill line do not have a great

discrepancy. At the infill location, total stress reversal (90°) for S_{Hmax} is obtained for all three legacy productions. Beyond the infill location, S_{Hmax} is generally in the initial direction in the unfractured reservoir volume, with noticeable reorientation primarily observed around and within producing fractures. In Figure 5.13d, the three profiles are nearly the same. After 1 year of parent well production, the stress at the infill location is already largely reversed.

In Figure 5.14, when DS is intermediate with a value of 3 MPa, the effect of legacy production increases. Stress at the infill location is not reversed after 1 year of parent well production. When the legacy production increases to 5 or 10 years, stress is again totally reversed at the infill location. This trend is better presented in Figure 5.14d. After 1 year of legacy production, the greatest stress reversal is obtained between X=200 m and X=280 m with the values around 15°. However, as legacy production increases to 5 years, the profile is increased to 90°, indicating totally reversed stress. The further increase to 10 years does not significantly increase the stress reversal profile. Besides, the peaks of the reorientation profiles are not obtained right at the center of the infill line. This is because the center corresponds to the shorter inner fractures along parent wells, and shorter fractures are not as effective as longer fractures in reorienting stress at the infill location.

In Figure 5.15, DS is increased to 5 MPa. Since large DS prevents stress from significantly reorienting, the stress reversal in this case is not as significant as in Figure 5.13 and Figure 5.14. For example, after 1 year of legacy production, the S_{Hmax} reorientation profile along the infill line is nearly zero (Figure 5.15d). The increases of S_{Hmax} reorientation profiles from 1-year legacy production to 5-year legacy production and

from 5-year legacy production to 10-year legacy production are more significant than those in the 1 MPa case (Figure 5.13d) and the 3 MPa case (Figure 5.14d). Also, the expansion of the width of the stress reversal profiles in Figure 5.15d caused by increasing legacy production time is more significant than the other two cases. Thus, it is proposed that the increased DS increases the effects of legacy production on stress reversal at the infill location.

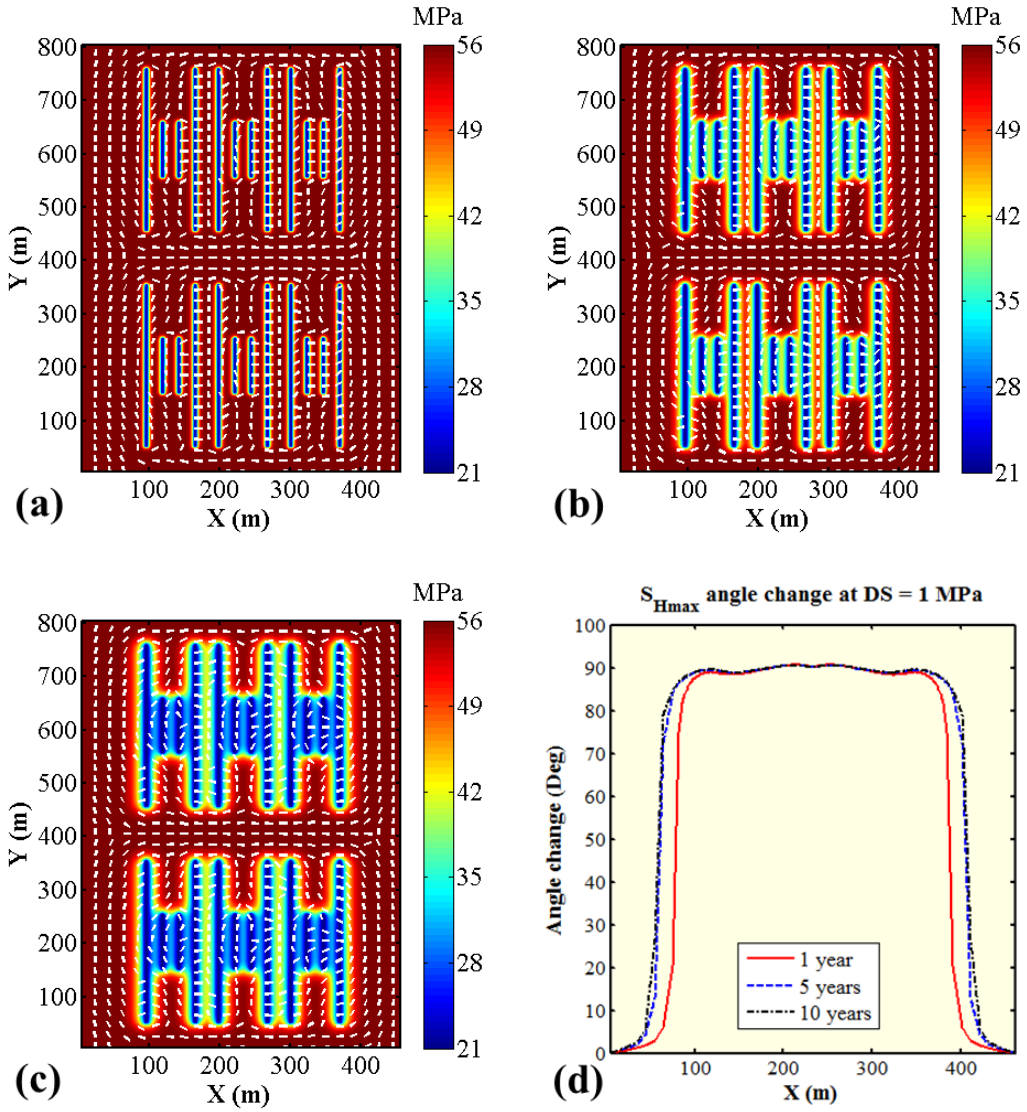

Figure 5.13. Pressure and S_{Hmax} orientation at (a) 1 year, (b) 5 years, and (c) 10 years for differential stress = 1 MPa; (d) S_{Hmax} angle change along the infill line at Y = 405 m

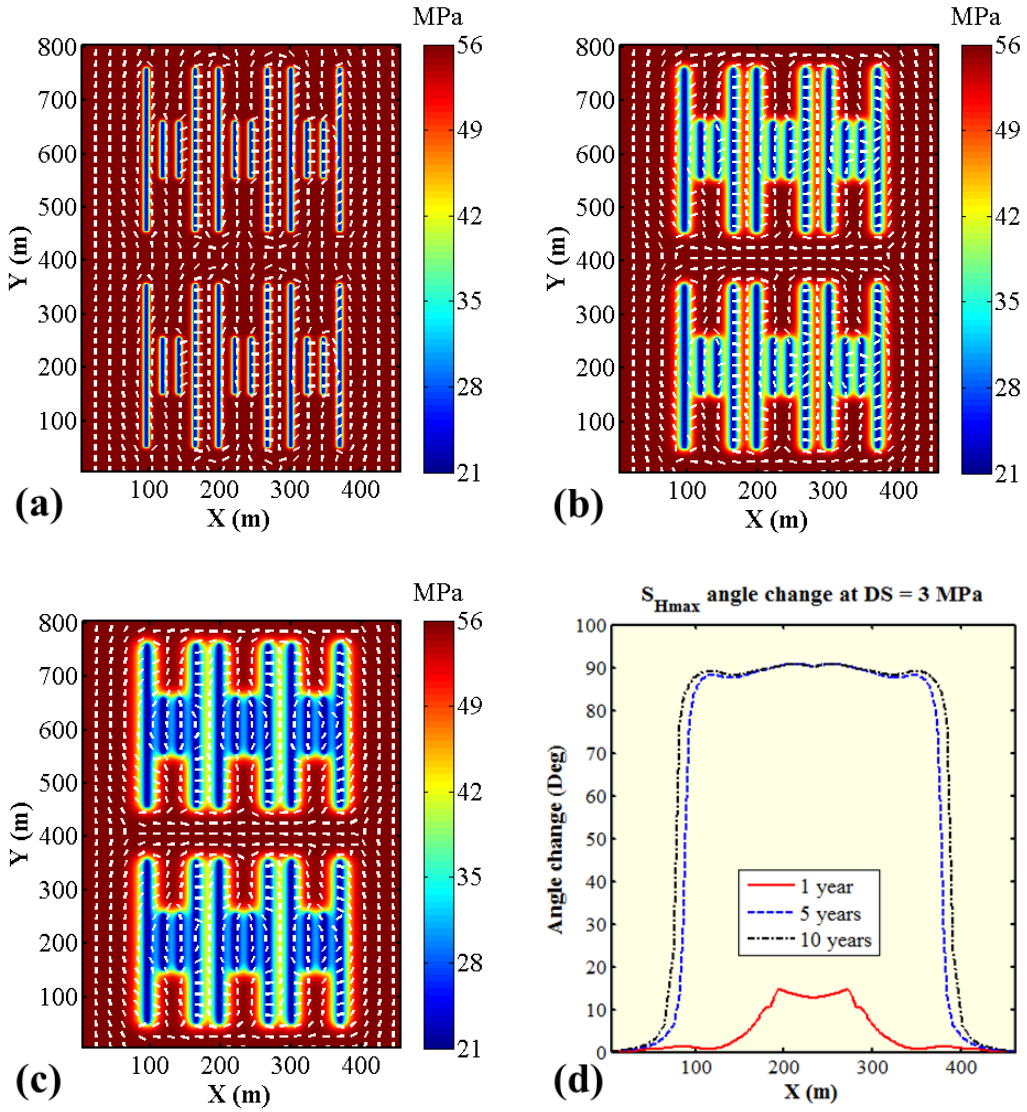

Figure 5.14. Pressure and S_{Hmax} orientation at (a) 1 year, (b) 5 years, and (c) 10 years for differential stress = 3 MPa; (d) S_{Hmax} angle change along the infill line at Y = 405 m

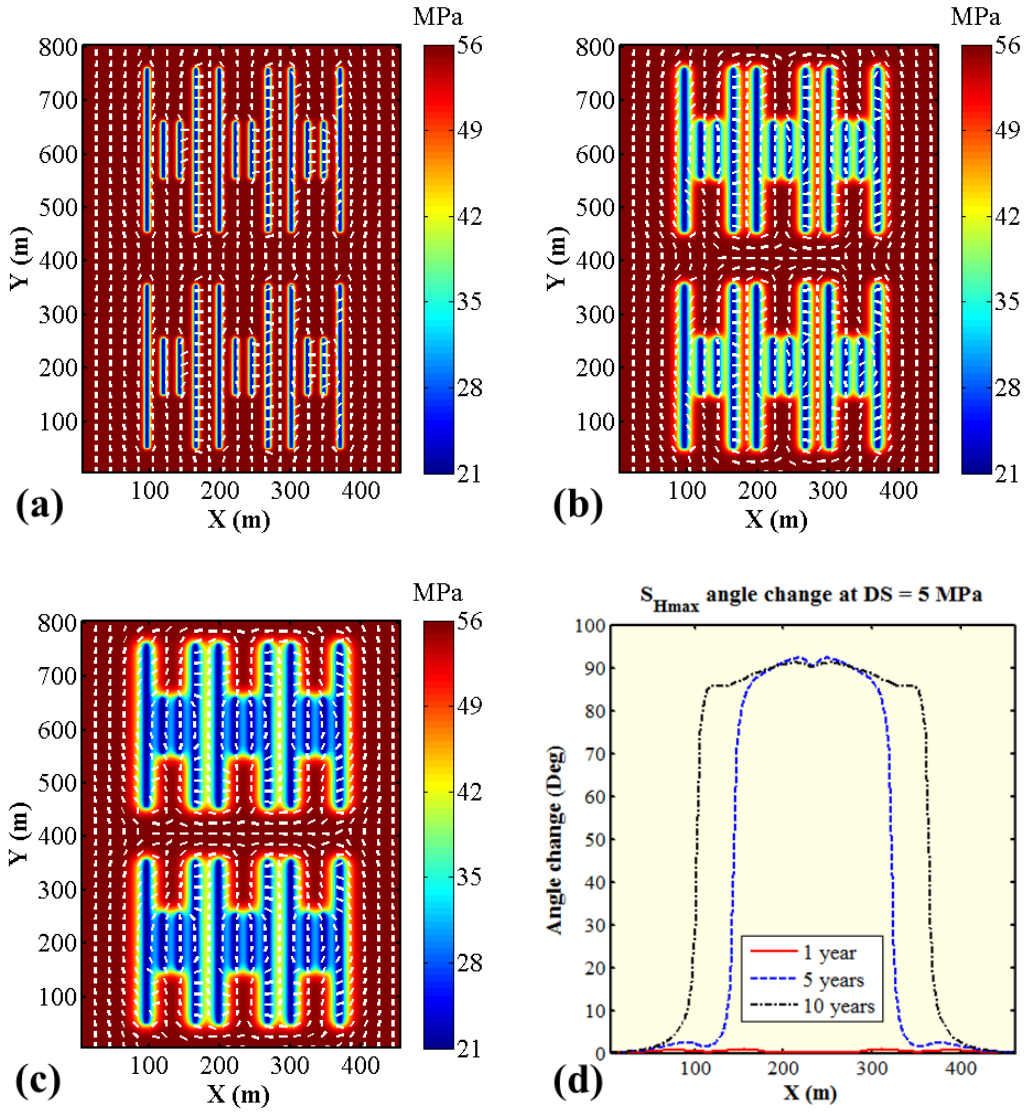

Figure 5.15. Pressure and S_{Hmax} orientation at (a) 1 year, (b) 5 years, and (c) 10 years for differential stress = 5 MPa; (d) S_{Hmax} angle change along the infill line at Y = 405 m

5.4.2 Modeling of Interwell Fractures

The hydraulic fracture model is again used for the characterization of the completion quality of the infill well in cases with different DS values and legacy

production times. The completion parameters are in Table 5.2. Individual fracture propagation is considered and no fracturing interaction in simultaneous fracturing is covered. A fracture spacing of 23 m is used in this study, and four different perforation cluster locations are prescribed along the infill well.

Figure 5.16 shows the infill well fracture geometries for 1 MPa DS (based on simulation results in Figure 5.13). Since infill zone stress is totally reversed, the infill well fractures are longitudinal. These highly longitudinal infill well fractures imply insignificant interwell interference as the potential of production competition between parent and infill wells is low. They also imply bad infill well completion quality and low production potential of the infill well as the longitudinal fractures do not help to effectively increase the contact area with the low permeability reservoir. These observations are valid for all three legacy production cases. In Figure 5.16d, the four infill well fractures' transverse percentages are around 39% for the 1-year legacy production case. They drop to around 35% for the 5-year legacy production case. For the 10-year legacy production case, the percentages drop to 33.5%. Besides, it is noted that varying the perforation cluster location for infill well completion does not largely affect the resulting fracture geometry, as the transverse percentage does not change much for the same legacy production time.

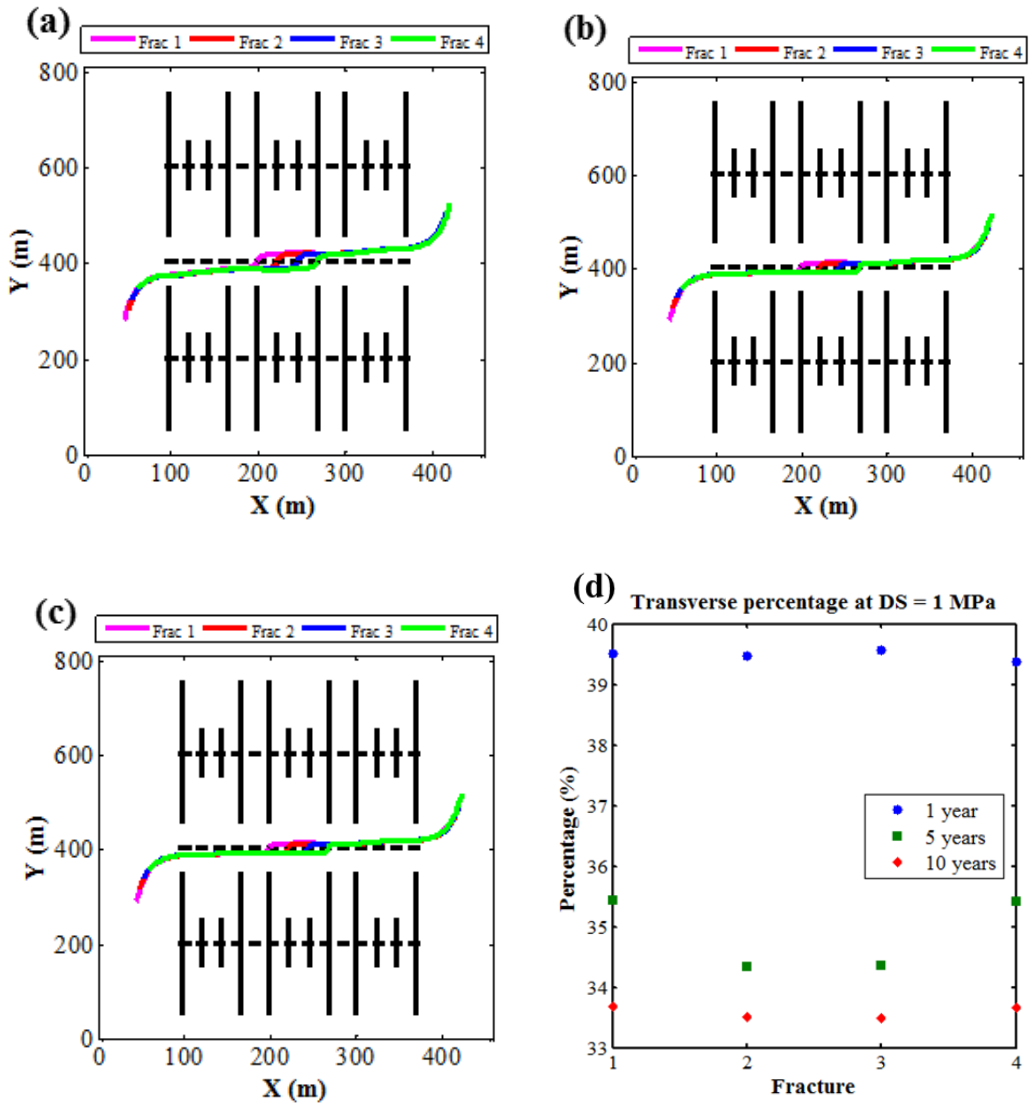

Figure 5.16. Infill well fracture propagation paths in the non-uniform geometry model after legacy production in parent wells for (a) 1 year, (b) 5 years, and (c) 10 years with differential stress of 1 MPa; (d) the transverse percentages of infill well fractures; infill well fractures are individually modeled

Figure 5.17 presents infill well fractures propagated under 3 MPa stress at three different infill well completion timings (or legacy production times). For 3 and 5 years of

legacy production, highly longitudinal fractures are obtained along the infill well. However, after only 1 year of legacy production, the resulting infill well fractures are transverse. These results correspond to stress reversal profiles in Figure 5.14d. For the 1 year legacy production case, stress reorientation is only around 20° between X=200 m and X=280 m. This is not a significant stress reversal which leads to an insignificant diversion of infill well fractures as they initially propagate away from the wellbore in Figure 5.17a. As they further propagate near parent well fracture tips, their propagation paths are diverted by the reoriented S_{Hmax} circled around parent well fractures. When they propagate to areas near parent wells, the upper wings of fractures 1-3 and the lower wings of fractures 2-4 are bounced back by the parent well fractures, which avoids possible frac hits. This is caused by the local stress state as in Figure 5.18: S_{Hmax} is in the initial direction at locations where infill well fractures are bounced, and S_{Hmax} orientations are observed to be guiding the infill well fractures away from parent well fractures at areas immediately adjacent to the bouncing locations. The overall trends for transverse and longitudinal growths of infill well fractures in different legacy production cases can be seen in Figure 5.17d.

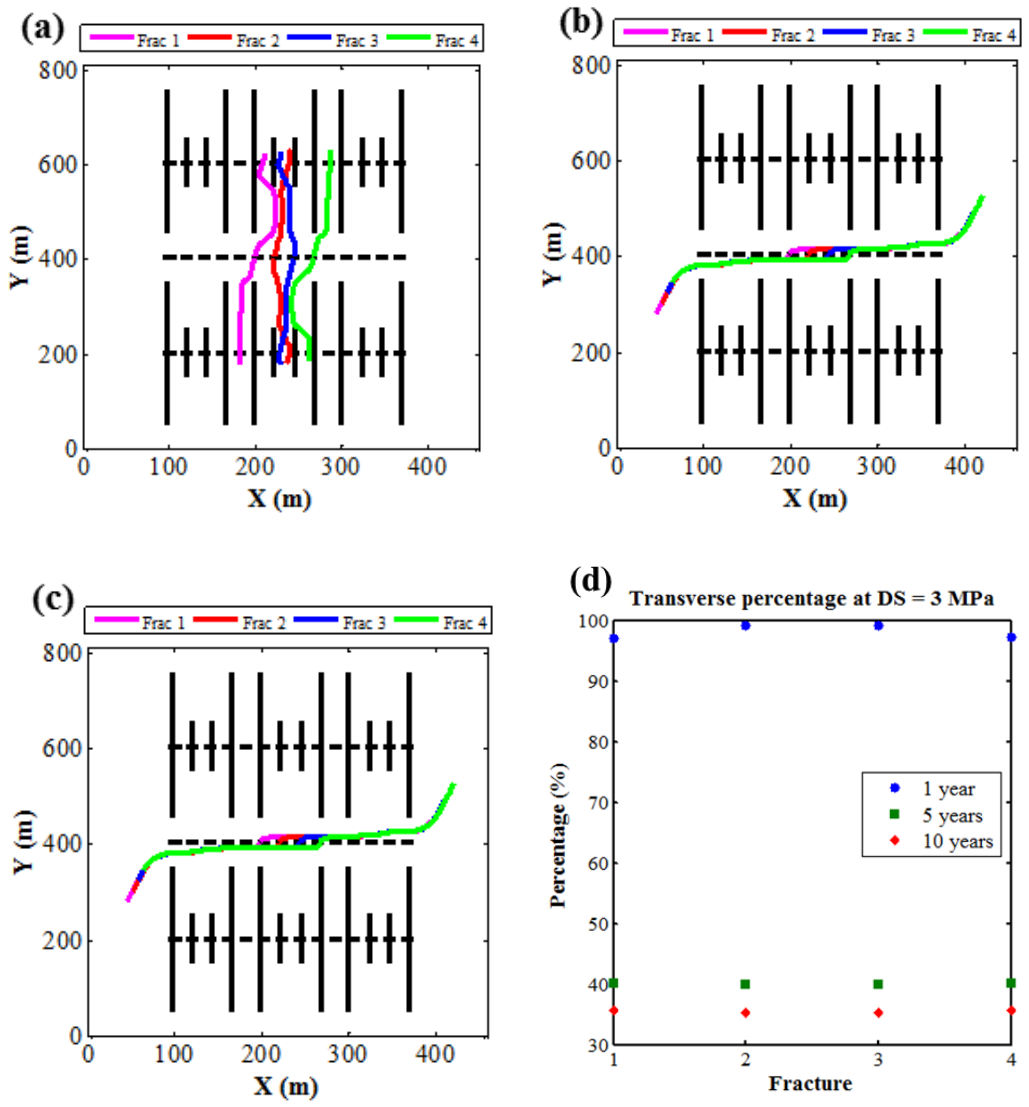

Figure 5.17. Infill well fracture propagation paths in the non-uniform geometry model after legacy production in parent wells for (a) 1 year, (b) 5 years, and (c) 10 years with differential stress of 3 MPa; (d) the transverse percentages of infill well fractures; infill well fractures are individually modeled

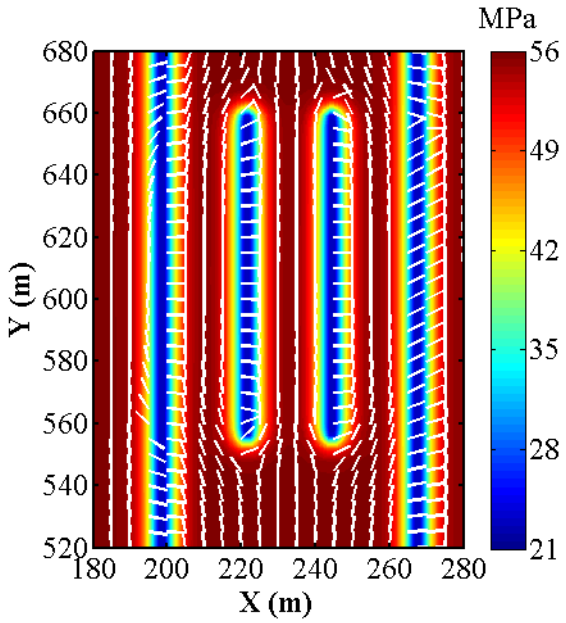

Figure 5.18. Local S_{Hmax} orientation causing fracture bounces for 1 year legacy production under 3 MPa differential stress (for Figure 5.17a)

Figure 5.19 presents the infill well fracturing results under 5 MPa differential stress. Since S_{Hmax} is not totally reversed at the infill location under 5 MPa DS, the resulting infill well fractures are more transverse with more complex shapes. In Figure 5.19a, stress reorientation along the infill line is insignificant. Therefore, infill well fractures grow ideally transversely in the infill zone. Once they propagate outside the infill zone and approach parent well fracture tips, they are slightly diverted due to the stress reorientation around parent well fracture tips. In Figure 5.19b, infill zone has more stress reversal, leading to the initial longitudinal growth of infill well fractures in the X direction. As they continue to propagate to infill zones without stress reversal, they start to turn to parent wells due to the local stress orientations. For the lower wings of fractures 1 and 2 and the

upper wings of fractures 3 and 4, they continue to propagate to the adjacency of the inner shorter fractures of stages along parent wells, leading to a local longitudinal growth of these wings hitting the adjacent longer parent well fractures. Thus, frac hits are captured in this specific case. Then, in Figure 5.19c, stress reversal at the infill zone becomes more significant, leading to more complexity of infill well fracture shapes. Curvatures of infill well fractures are observed in this case around parent well fracture tips, and frac hits are observed for the lower wings of fractures 1 and 2 and the upper wings of fractures 3 and 4. In Figure 5.19d, the average transverse percentage of the four fractures decrease with the increase of legacy production time. However, the transverse percentages of fractures 1 and 4 do not decrease as legacy production time increases from 5 years to 10 years. Transverse percentages of fractures 2 and 3 uniformly decrease from 100% to 64% as legacy production increases from 1 year to 10 years.

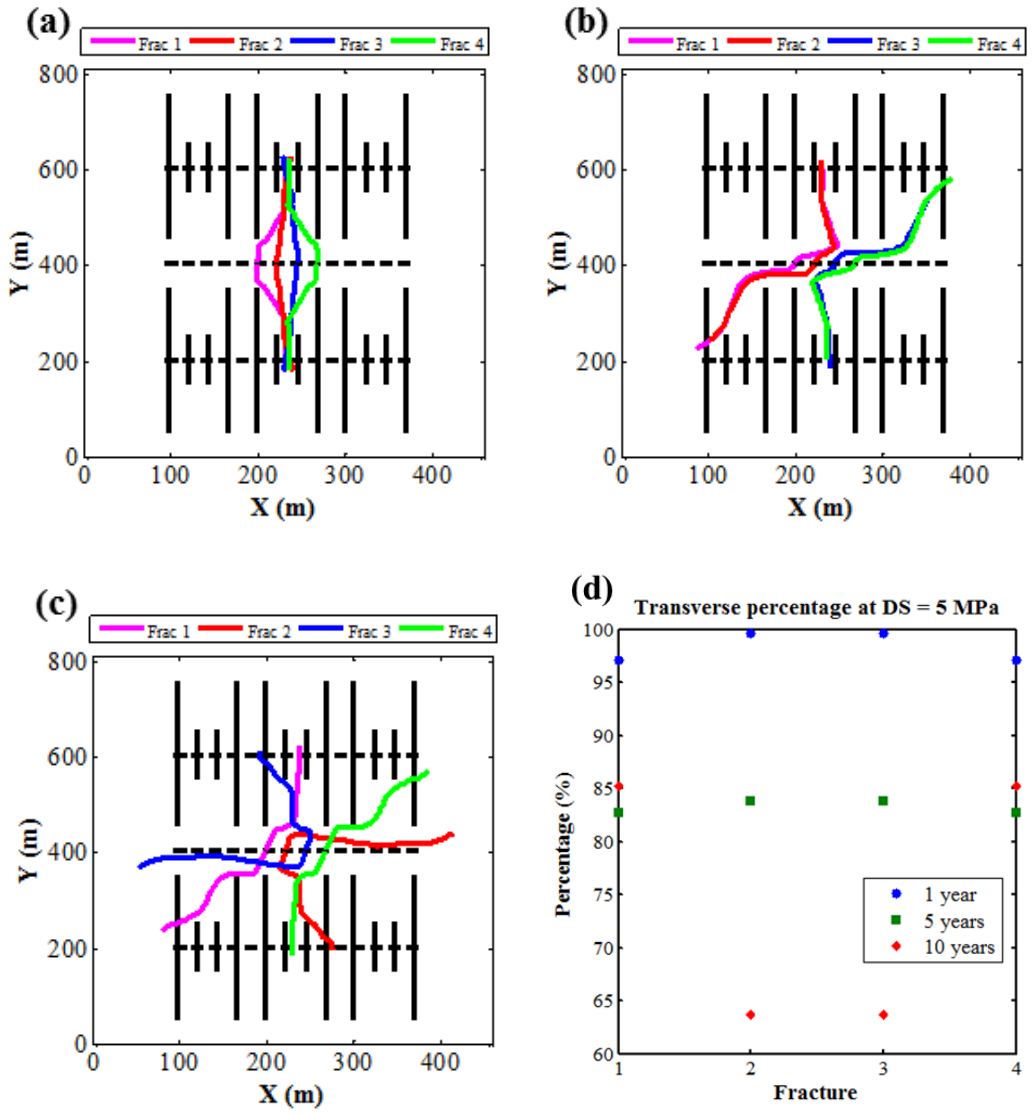

Figure 5.19. Infill well fracture propagation paths in the non-uniform geometry model after legacy production in parent wells for (a) 1 year, (b) 5 years, and (c) 10 years with differential stress of 5 MPa; (d) the transverse percentages of infill well fractures; infill well fractures are individually modeled

5.5 Comparison Between the Two Studies

A difference is noticed comparing the stress reversal profiles in the uniform fracture half-length study and the non-uniform fracture half-length study. When parent well fractures are uniform, the peaks of the stress reversal profiles (maximum S_{Hmax} reorientation along the infill line) are always obtained right at the center of the infill line (Figure 5.3d, Figure 5.4d, and Figure 5.5d). When parent well fractures are not uniform, the peaks of the stress reversal profiles are not at the center of the infill line (Figure 5.13, Figure 5.14, and Figure 5.15). This is because when parent wells have uniform fractures, the symmetric depletion leads to the occurrence of stress reversal peaks at the center of the reservoir. However, when parent well fractures are not uniform, longer parent well fractures tend to have a greater influence on infill location stress reorientation and shorter parent well fractures tend to have less influence. Since locations of shorter fractures correspond to the center of the infill line and locations of longer fractures are correspond to other locations along the infill line, peaks of stress reorientation profiles are always placed at locations other than the center.

Then, the effects of several relevant parameters on infill well fracture geometry are ranked. The characteristic to evaluate infill well fracture geometry is the transverse percentage. Figure 5.20a shows the tornado chart for the uniform fracture half-length reservoir model conceptually describing the parent well completion and Figure 5.20b shows the tornado chart for the non-uniform fracture half-length reservoir model. Vertical lines in green are the base case transverse percentages. Changing the fractures from uniform to non-uniform decreases the base case transverse percentage from 0.76 to 0.39.

Blue bars indicate how transverse percentage changes due to the decrease of a certain parameter, and the decrease of transverse percentage can be caused by decreased DS or by the increase of legacy production. In the uniform fracture half-length case, DS has the greatest effect. In the non-uniform fracture half-length case, legacy production has the greatest effect. Although perforation cluster location always has the smallest effect, it affects the stress path an infill well fracture propagates through and contributes to the occurrence of frac hits.

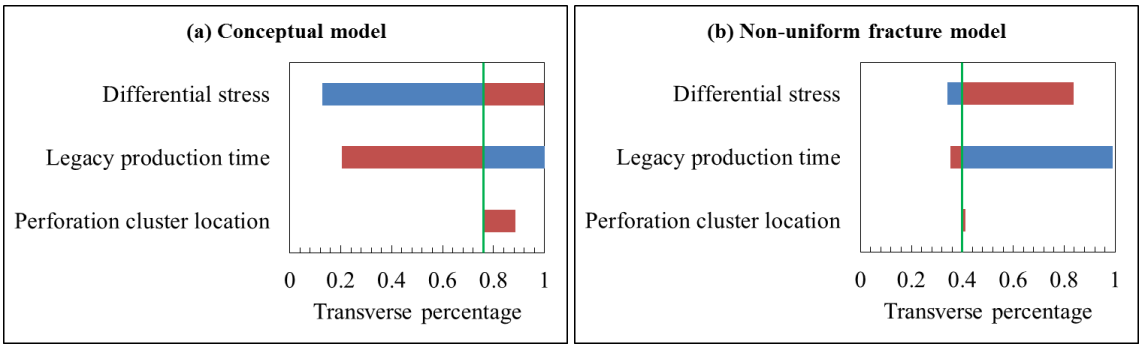

Figure 5.20. Tornado charts for the conceptual model (a) and the non-uniform fracture model (b)

5.6 Conclusion

This section presents the use of a numerical modeling workflow for the investigation of production-induced pressure and stress changes and the resulting hydraulic fracture geometries. The reservoir models are constructed based on Eagle Ford

data. A parameter called transverse percentage is introduced for the evaluation of the infill well completion quality. In conclusion:

(1) The assumption of uniform fracture half-length for parent wells in this study and in previous studies (Rezaei et al. 2017a; Rezaei et al. 2017b) is not efficient in capturing frac hits. The usage of non-uniform parent well fracture helps to capture the phenomenon of frac hits during the completion of the infill well.

(2) The stress reversal around the shorter inner fractures' tips in scenarios with non-uniform fracture half-lengths is the important cause of frac hits. This local stress reversal diverts the growth of infill well fractures in the longitudinal direction and induces the hit with the neighboring longer fractures along parent wells.

(3) Based on tornado charts, DS and legacy production both have great influences on infill well fracture growth, while perforation cluster location along the infill well has insignificant influence. Parent well fracture geometry also impacts the growth of infill well fractures. The complexity of interwell fracture fractures increases as parent well fractures become more complex/non-uniform.

(4) In the simultaneous propagation of multiple fractures along the infill wellbore, the growth of the central fracture is inhibited by the growth of adjacent fractures. The degree of this interference decreases with the increase of fracture spacing.

(5) Legacy production leads to heterogeneous S_{Hmax} orientations at and around parent well fractures. This heterogeneity does not always contribute to frac hits. It helps to avoid frac hits in certain cases

6 PARALLEL PERFORMANCE*

6.1 Introduction

This section presents the parallel simulation performance based on the runs of the sequentially coupled simulator in Section 2.2. Note that this section is not related to the fully coupled flow and geomechanics simulator presented in Section 2.1 and it is not related to any of the numerical results presented in Sections 3-5.

The parallel performance of the simulator in Section 2.2 is presented in this section. A reservoir mesh with one million gridblocks is used for the simulation. Three case studies are presented to test the parallel efficiency and scalability of the simulator developed by the portable scheme.

Liquid injection and production is first simulated so that the parallel performance of the overall simulator and specific subroutines can be profiled. Plasticity is then simulated to examine its effect on workload imbalance in the parallel system. Finally, several matrix decomposition schemes are tested to examine their effects on solver efficiency.

*Part of this section is reprinted with permission from "Hybrid MPI-OpenMP Scalable Parallelization for Coupled Non-Isothermal Fluid-Heat Flow and Elastoplastic Geomechanics" by X. Guo, J. Kim, and J. Killough. SPE Proceedings, Copyright [2017] by Society of Petroleum Engineers.

6.2 Parallel Environment

The Ada supercomputer of Texas A&M University is used in this parallel study. It has a mixed memory architecture with both distributed memory and shared memory. In this machine, the compute nodes are IBM NeXtScale nx 360 M4 dual-socket servers with Intel Xeon 2.5GHz E5-2670 v2 10-core processors. In the 10-core processor, each core (each CPU) has its own on-chip L1 and L2 caches. Each processor has its own L3 cache.

The distributed memory improves the efficiency in solving large-scale problems. The shared memory reduces overheads for localized iterations without any data communication between neighboring gridblocks. They help to improve the computational efficiency of solving linear systems, speed up array assembly, and reduce overheads.

6.3 Liquid Injection/Production

A 3D synthetic reservoir model is first constructed to test the non-isothermal fluid injection and production coupled with geomechanics. In this case, single phase decane is injected in one injection well with fixed injection rate and constant specific enthalpy. The single phase fluid is also produced at another production well with a constant rate. In geomechanics, linear elasticity is considered. The rock properties are in Table 6.1. The fluid properties are in Table 6.2. The reservoir model setup is in Table 6.3. The model is sketched in Figure 6.1.

Property	**Value/specification**
Porosity	0.15
Grain density	2600 $\mathrm{kg/m^3}$
Saturated heat conductivity	3.1 W/(m K)
Desaturated heat conductivity	0.5 W/(m K)
Rock compressibility	5×10^{-9} 1/Pa
Grain specific heat	1000 J/kg/K
Permeability	1.5×10^{-13} $\mathrm{m^2}$
Young's modulus	0.6 GPa
Shear modulus	0.3 GPa

Table 6.1. Rock properties (reprinted with permission from Guo et al. 2017)

Property	**Value/specification**
Fluid type	Decane
Reference density	728.3 $\mathrm{kg/m^3}$
Compressibility	1×10^{-9} 1/Pa
Reference pressure	0.1 MPa
Reference temperature	25°C
Reference viscosity	$8.632 \times 10^{-4}\mathrm{Pa \cdot s}$
Expansivity	1×10^{-5} 1/K
Reference thermal conductivity	0.1322 W/(m K)
Reference specific heat	313.72 J/kg/K
Mole weight	142.3 g/mol

Table 6.2. Fluid properties (reprinted with permission from Guo et al. 2017)

Property	Value/specification
Dimension	320 by 320 by 10
Cell size	5m by 5m by 5m
Injector cell location	(1,1,1)
Producer cell location	(320,320,10)
Injection rate	0.5 kg/sec
Injection specific enthalpy	2.263×10^{-5} J/kg
Production rate	0.5 kg/sec
Initial temperature	30°C
Initial pressure	30 MPa
Simulation time	365 days
Overburden stress	30 MPa

Table 6.3. Reservoir model parameters (reprinted with permission from Guo et al. 2017)

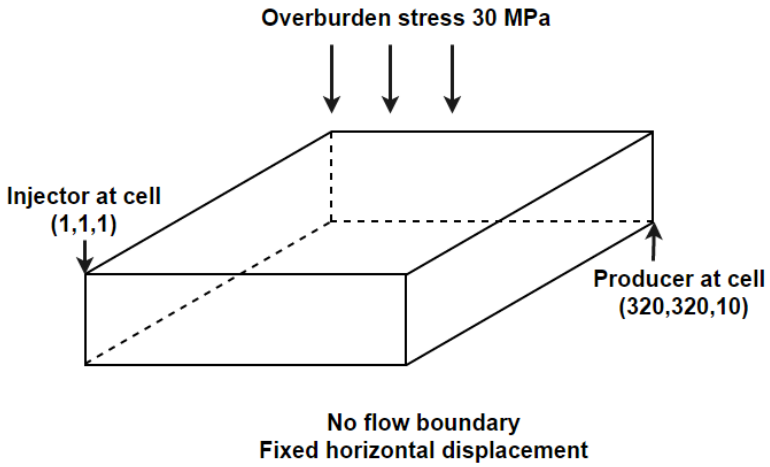

Figure 6.1. Reservoir for the liquid injection production simulation (reprinted with permission from Guo et al. 2017)

Several Newton iterations are required at each time step due to the nonlinearity of the fluid-heat flow. One Newton iteration is required at each time step for the geomechanics problem since linear elasticity is considered in this case. Therefore, although the size of the fluid-heat flow problem is smaller than the geomechanics problem, it is still meaningful to obtain speedup for the flow problem since multiple iterations are required at each time step. GMRES solver is used for matrix solution, with restart of 30. For the single core simulation, ILU(0) preconditioning is used. For multi-core parallel simulations, block Jacobi method is used for preconditioning (Balay et al. 2014). Note that the usage of the block Jacobi method can put limitations on the parallel performance when the ratio of unknowns per process to the total unknowns decrease, and domain decomposition preconditioning and multigrid methods could resolve this issue. Other numerical parameters for the simulation are in Table 6.4.

Numerical parameter	**Value**
Initial time step	1 second
Maximum time step	8.64e6 seconds
Convergence criterion for Newton-Raphson method	1e-9
Geomechanical total degree of freedom	3283188
Number of flow problem's primary variables	2048000
Parallel solver convergence criteria	
L2-norm of residual	1e-50
Decrease of L2-norm of residual / L2-norm of right hand side	1e-5

Table 6.4. Numerical parameters for the liquid production injection case (reprinted with permission from Guo et al. 2017)

Simulation results are then presented. Figure 6.2 shows the pressure distribution at the bottom and top layers. Figure 6.3 shows the temperature distribution at the end of the simulation for the top layer. Figure 6.4 shows the temporal evolutions of the volumetric strain at the injection well and at the production well. Based on the results, pressure increase is observed near the injection well and pressure decrease is observed near the production well due to fluid flow diffusion. Temperature change is slow, with only the areas around the injection well experiencing temperature change. The highest temperature is 90°C due to injection. Absolute values of volumetric strain uniformly increase at wells, since the injection and production wells have the greatest flow-induced rock deformation.

Parallel performance is then profiled. The serial input reading time for the flow problem is excluded in timing, since this reading is a one-time reading of gridblock and the associated grid connection data. The reading time for the geomechanics problem is included since the geomechanical grid is structured and generated within the code's own subroutine. This process for geomechanics leads to negligible computational load.

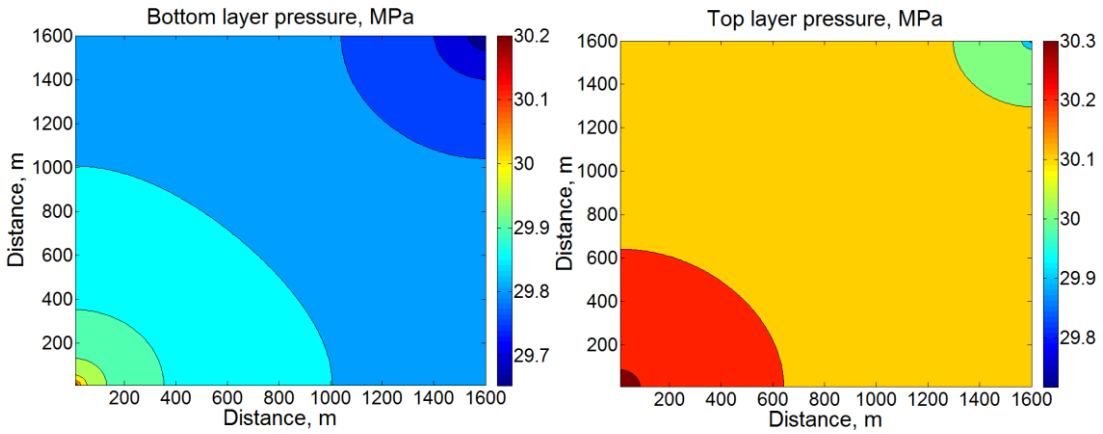

Figure 6.2. Pressure distributions at the end of the simulation for the bottom and top layers (reprinted with permission from Guo et al. 2017)

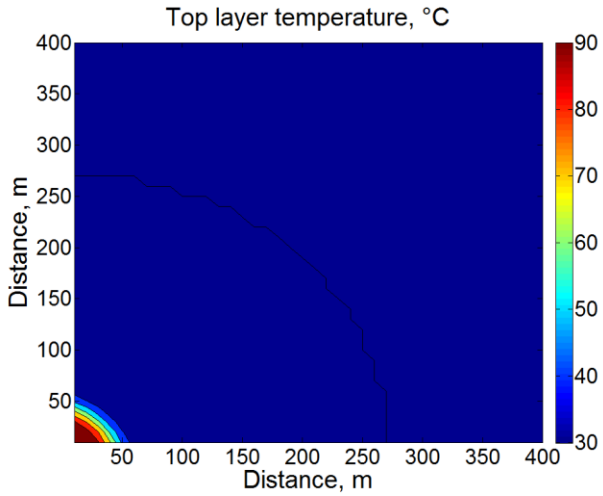

Figure 6.3. Temperature distribution at the top layer at the end of the simulation (reprinted with permission from Guo et al. 2017)

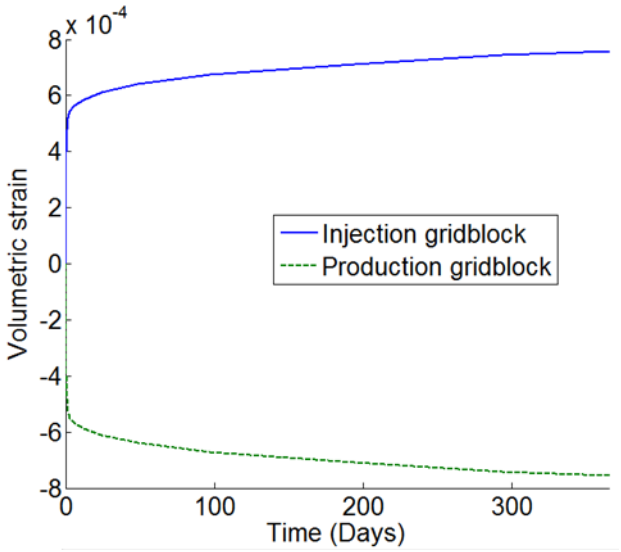

Figure 6.4. Temporal evolutions of volumetric strain at the injection and production wells

The performance for the geomechanics problem is recorded in Figure 6.5 and Table 6.5. Details such as execution time and speedup are presented. Good scalability for the solver is obtained as the process number increases from 1 to 32, and the corresponding matrix solution time is largely decreased. The best speedup for geomechanical matrix solution is 28.4 at 32 processes. However, the speedup is decreased when evaluating the total geomechanics execution time due to the limited parallel efficiency for the non-solver sections of the simulator. The optimum speedup for total geomechanics is obtained with 32 processes at a value of 24.7. Further increasing process number to 64 does not improve the speedup. On the contrary, it significantly decreases the parallel efficiency. Besides, the best speedup for parallel array assembly in geomechanics is 16.9 at 32 processes. The

Krylov iterations per time step generally decrease as process number increases. Miscellaneous execution time decreases due to the use of OpenMP.

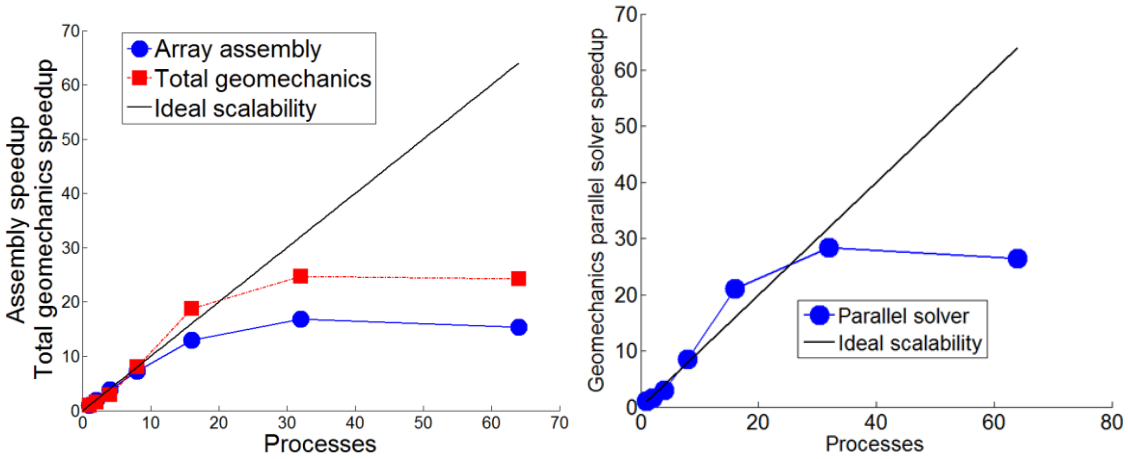

Figure 6.5. Parallel performance of the geomechanics problem (reprinted with permission from Guo et al. 2017)

Processes	1	2	4	8	16	32	64
Assembly, seconds	3478.3	1796.8	920.2	483	268.5	206.2	226.5
Parallel solver, seconds	6303.4	4018.8	2101	739.8	289.4	221.9	238.8
Krylov iterations per time step	141	234	262	127	27	29	31
Miscellaneous, seconds	141.2	113.5	80.9	59.2	43.8	39.2	26.6
Total time, seconds	6444.6	4132.3	2181.9	798.9	342.2	261.1	265.4
Assembly speedup	1	1.9	3.8	7.2	13	16.9	15.4
Solver speedup	1	1.6	3	8.5	21.1	28.4	26.4
Total geomechanics speedup	1	1.6	2.9	8.1	18.8	24.7	24.3
Unknowns per process (rounded)	3283188	1641594	1094396	410398	205199	102599	51299

Table 6.5. Parallel performance of the geomechanics problem (reprinted with permission from Guo et al. 2017)

The performance of the flow problem is shown in Figure 6.6 and Table 6.6. The best overall flow speedup is 10.9 at 32 processes. The best flow matrix solution speedup is 24.8 at 64 processes.

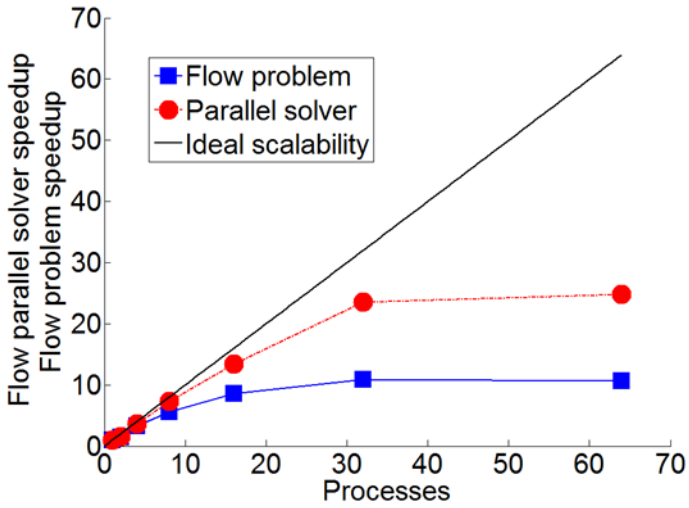

Figure 6.6. Parallel performance of the flow problem (reprinted with permission from Guo et al. 2017)

Processes	1	2	4	8	16	32	64
Total flow simulation time, seconds	7290.6	4948.5	2246.5	1301.4	847.4	667.7	685.3
Parallel solver time, seconds	6991	4646.4	1945.9	957.3	522.5	296.3	281.4
Total flow simulation speedup	1	1.5	3.2	5.6	8.6	10.9	10.6
Parallel solver speedup	1	1.5	3.6	7.3	13.4	23.6	24.8

Table 6.6. Parallel performance of the flow problem (reprinted with permission from Guo et al. 2017)

The overall parallel performance for the coupled flow and geomechanics simulation is shown in Figure 6.7 and Table 6.7. This performance consists of the parallelized flow simulation, the parallelized geomechanics simulation, and the sequential coupling scheme for the updating of flow and geomechanics parameters. In general, the scalability separately observed in the flow and the geomechanics problems is still honored in the coupled simulation. The best overall speedup is 14.8 at 32 processes. Increasing from 32 processes to 64 processes does not lead to improvement of parallel efficiency. The overall scalability is nearly identical to the ideal scalability for up to 16 processes, implying that a parallelized coupled simulation with either 8 or 16 processes has good scalability and optimum cost-effectiveness. Therefore, when the parallel hardware is limited, using this code, the simulation with 8 or 16 processes can provide practical speedups.

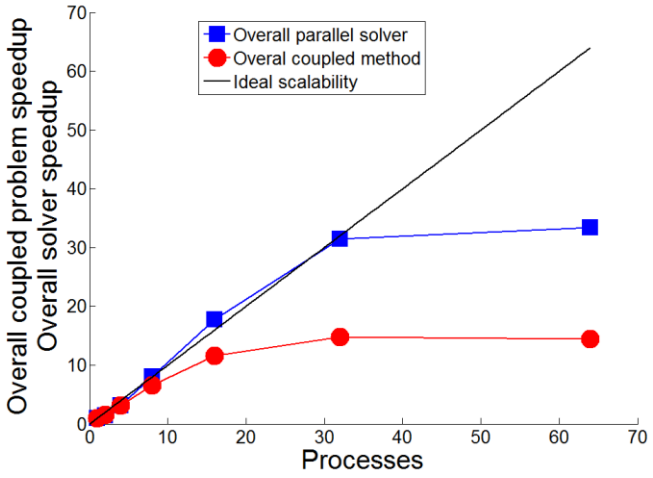

Figure 6.7. Overall parallel performance of the coupled flow and geomechanics simulation (reprinted with permission from Guo et al. 2017)

Processes	1	2	4	8	16	32	64
Solver time, seconds	9816	6868.4	3126.7	1214	552.4	312	293.7
Total simulation time, seconds	13735.2	9080.8	4428.4	2100.3	1189.7	928.8	950.7
Solver speedup	1	1.4	3.1	8.1	17.8	31.5	33.4
Total simulation speedup	1	1.5	3.1	6.5	11.5	14.8	14.4

Table 6.7. Overall parallel performance of the coupled simulation (reprinted with permission from Guo et al. 2017)

6.4 Plasticity

The effect of elastoplasticity on parallel performance is then investigated. In parallel simulations considering elastoplasticity, at a certain time step, some gridblocks are in the plasticity region and the other gridblocks are still in the elasticity regime, leading to workload imbalance in the parallel computation. In this study, the general setup is still the same as the liquid injection production case in Section 6.3. However, there is only one production well with no injection well. The production rate is also increased to 8 kg/s and the simulation time is increased to 1095 days. Thus, the increased production-induced rock deformation can lead to plasticity in certain areas in the reservoir mesh. Some plasticity related geomechanical parameters are in Table 6.8. Figure 6.8 shows the reservoir model used in the plasticity simulation. It also presents the locations of two monitoring points denoting the effective stress evolution. These two points are near the production well

where the production-induced deformation is significant. Figure 6.9 presents the details of the effective stress evolution of the two cells (1, 1, 5) and (5, 1, 1). In the evolution curves, the origin stands for the beginning of the evolution and the top-left parts of the curves are the later stages. Effective stresses increase due to pressure depletion. Since some tolerance is added to ensure that effective stress is in the plastic region, some stress points are located slightly higher than the failure lines.

In the parallel simulation, plasticity computation (return mapping) is localized, not requiring any data communication between neighboring cells and processes. Thus, cells with plasticity calculation are assigned to some processes while other processes only have elasticity calculation. Since plasticity calculation requires additional iterations in the local processes for nonlinearity, processes with plasticity calculations have heavier workloads.

In the assignment of cells, the equal number of continuous gridblocks is assigned to each process. An idle time ratio r_{id} is defined to quantitatively described the imbalance caused by plasticity as

$$r_{id} = \frac{t_{max} - t_{min}}{t_{max}}, \tag{6.1}$$

where t_{max} is the maximum execution time reported among the individual processes. The process reporting t_{max} has the heaviest return mapping computation. t_{min} is the minimum execution time reported among the processes. It represents the lightest return mapping computation load, indicating that the process has entirely elastic computation or insignificant plastic computation. The desirable r_{id} is zero indicating that all processes have the same execution time, and no processes are idle and waiting for other processes

to finish the computation. When $r_{id} > 0$, workloads are assigned to processes with imbalance.

Table 6.9 shows the idle time ratio comparison between the first time step and at the 27th time step (395 days). At the first time step, no plasticity is induced while the 27th time step has plasticity around the production well. Message passing time is excluded from the times used to calculate the idle time ratios.

At the first time step, the workload is balanced. The idle time ratio increases to 14.09% as process number increases to 64. This is because the execution times on processes are reduced to seconds for large process number runs, and small differences in execution time among processes lead to a great increase of idle time ratios. At the 27th time step, increases of idle time ratios are observed, which are caused by the fact that some processes only execute elasticity computation while other processes execute plastic and elastic computations. At the 27th step (395 days), among the 1024000 cells, 44864 cells get in the plasticity region.

This imbalance introduced by plasticity is a well-known issue in parallel simulation. The usage of load balancers can possibly alleviate the imbalance. Since plasticity evolves with the simulation and the initial setup of the simulation model does not always exhibit predictable patterns of plasticity, static load balancers (Guo et al. 2016) have limited effectiveness in improving load balancing. Dynamic load balancers (Wang and Killough 2014) can be a possible solution since they dynamically redistribute workloads as the simulation proceeds, and more computational resources can be reassigned to those cells experiencing heavy plastic computation loads.

Parameter	Value
Initial pressure	30 MPa
Biot's coefficient	1.0
Young's modulus	0.6 GPa
Cohesion	3 MPa
Friction and dilation angles	0.52°
Thermal dilation coefficient	$4.5 \times 10^{-5\circ}\ C^{-1}$

Table 6.8. Plasticity related geomechanical parameters (reprinted with permission from Guo et al. 2017)

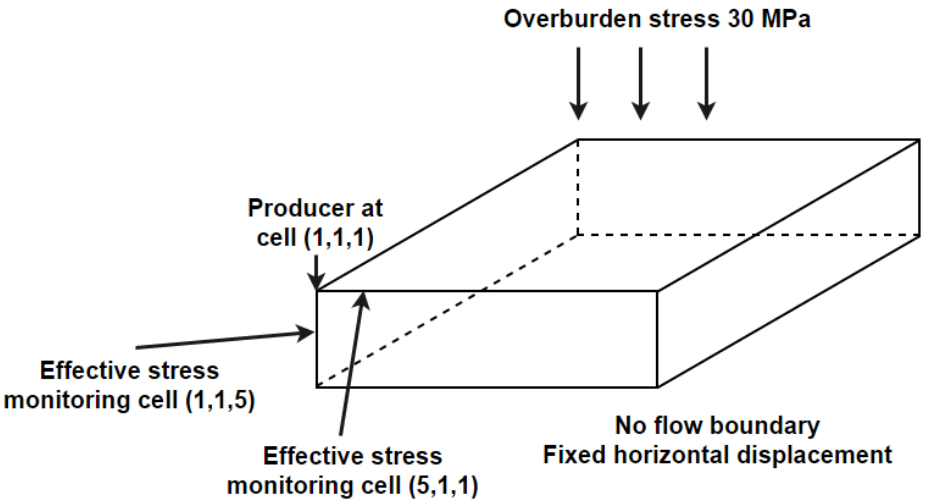

Figure 6.8. Sketch of the reservoir model for the plasticity study (reprinted with permission from Guo et al. 2017)

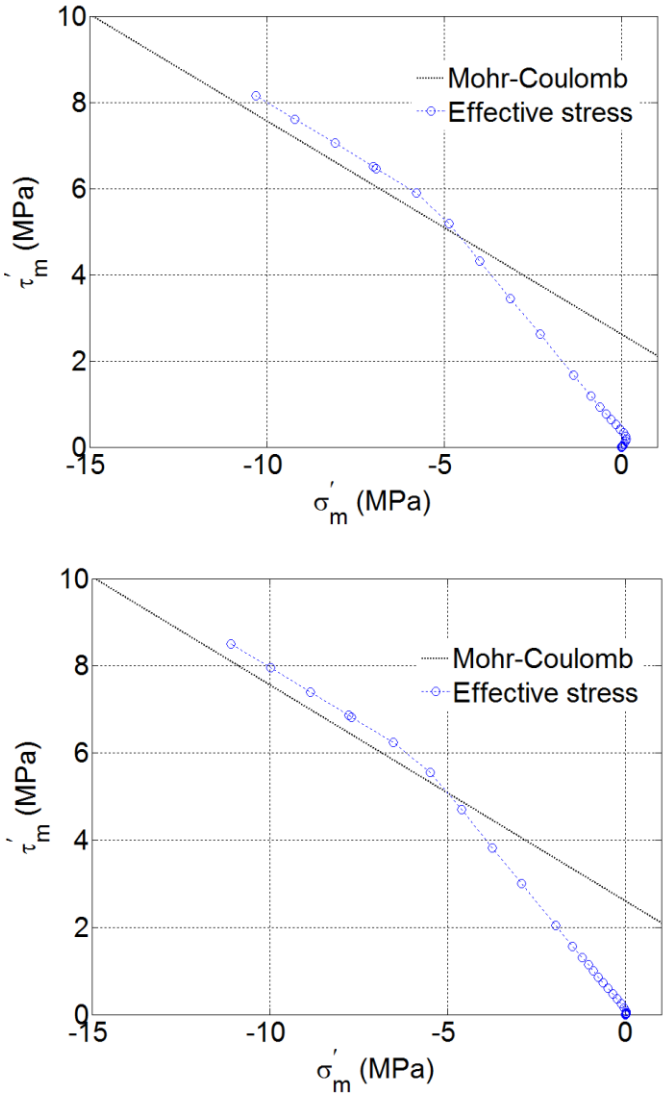

Figure 6.9. Effective stress evolution at monitoring points (5, 1, 1) and (1, 1, 5) near the production well (reprinted with permission from Guo et al. 2017)

	Idle-time ratios at first step	Idle-time ratios at 395 days
2 processes	0.07%	11.98%
4 processes	1.52%	12.48%
8 processes	1.15%	17.92%
16 processes	1.25%	25.32%
32 processes	5.96%	38.24%
64 processes	14.09%	46.67%

Table 6.9. Imbalance introduced by plasticity (reprinted with permission from Guo et al. 2017)

6.5 Matrix Decomposition

The correlation between matrix decomposition and parallel solver performance is then studied. Decomposition methods have an influence on the resulting convergence and iterations, and eventually affect the parallel performance. In this study, the decomposition of the stiffness matrix in the geomechanics problem is specifically investigated. Stiffness matrices usually have many non-zero elements. Figure 6.10 schematically shows the typical non-zero elements of a stiffness matrix with the total degree of freedom of 204. There are 6658 non-zero elements. Since structured linear 3D hexahedral cells are used in the mesh, the maximum number of non-zero elements per row can reach up to 81.

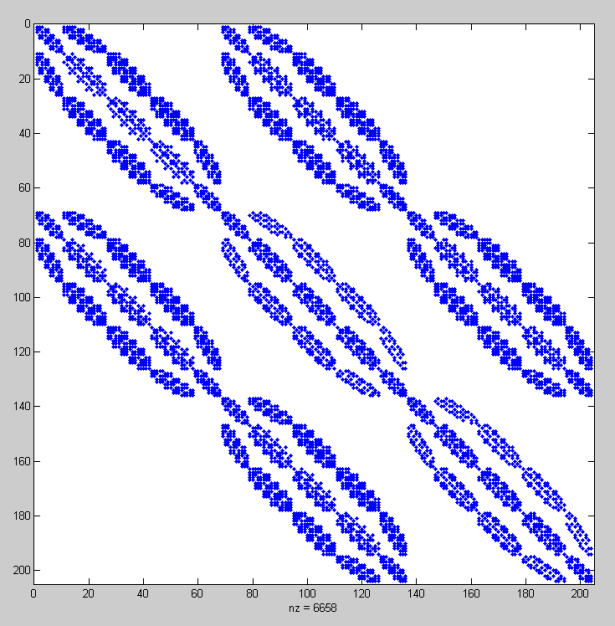

Figure 6.10. Non-zero elements of a stiffness matrix with degree of freedom of 204 (reprinted with permission from Guo et al. 2017)

The properties of the stiffness matrix actually used in this case are shown in Table 6.10. The stiffness matrix is still based on the inputs in Section 6.3 with 1024000 cells. The default decomposition method is to decompose the stiffness matrix into partitions with contiguous rows, and each partition has the same rows. Each partition is then distributed to a process. If the total row number of the matrix is not divisible by the process number, rows assigned to processes are rounded and a maximum difference of row numbers of one is allowed among partitions. Since each row does not always contain the same number of non-zero elements, imbalance can be introduced by the default decomposition method.

A different decomposition method is introduced. The same number of non-zero elements is assigned to each process. As a result, each process can receive different numbers of contiguous rows while it receives the same number of non-zero elements. In the assignment, a value called maximum non-zero element difference nnz_{diff} is defined to denote the difference of non-zero element numbers between the process with the heaviest load and the process with the lightest load. nnz_{diff} is written as

$$nnz_{diff} = nnz_{max} - nnz_{min}, \tag{6.2}$$

where nnz_{max} is the maximum non-zero elements on a single process and nnz_{min} is the minimum non-zero elements on a single process. Table 6.11 shows the decompositions made by this method compared to those by the default method for a 4-process case. The new method largely decreases the nnz_{diff}. In the default method, nnz_{diff} is 10126905 between processes 2 and 3. Using the new method, nnz_{diff} is largely reduced to 33 between processes 1 and 3. Thus, non-zero elements are more evenly distributed by the new method.

Parameter	**Value**
Number of non-zero elements	246224568
Total degree of freedom	3283188
Global row number	3283188
Global column number	3283188

Table 6.10. Properties of the stiffness matrix (reprinted with permission from Guo et al. 2017)

Process	Default decomposition strategy		New decomposition strategy	
	Local row number	Local non-zero number	Local row number	Local non-zero number
0	820797	57888006	866200	61556145
1	820797	66125799	764237	61556121
2	820797	66168834	763456	61556148
3	820797	56041929	889295	61556154

Table 6.11. Comparison between two decomposition methods for 4-process (reprinted with permission from Guo et al. 2017)

Parallel simulations using 2-, 4-, 8-, and 16-process are then carried out to compare the performances using the two decomposition methods. Except for the matrix decomposition, other parameters of the simulations are fixed. Batch jobs are used to ensure that the parallel environment is constant for all simulations and to reduce the impact of load variability in the supercomputer. Table 6.12 shows the details of the performance. The new decomposition method reduces the solver iterations and the MPI communication time. Since MPI communication is timed on each process and reported as the summation, MPI communication time can be actually greater than the execution time reported on the master process. The new decomposition method also reduces the solver time, with the only exception reported for the 4-process simulation.

It is also noted that with the increase of process number, the workload on each process becomes small and the communication cost increases. To address the issue of the increased communication cost, inter-process communication can be possibly handled by graph partitioners (e.g., Metis and Chaco) which utilize degree of freedom and mesh connectivity (Hendrickson and Leland 1993; Karypis and Kumar 1995).

Process	Default decomposition strategy		
	Total solver time, s	**Total solver iterations**	**Total solver communication time, s**
2	2928.7	7020	7290
4	1392.2	7860	16320
8	326.4	3810	7980
16	39.6	930	4080
Process	**New decomposition strategy**		
	Total solver time, s	**Total solver iterations**	**Total solver communication time, s**
2	2879.4	6990	7260
4	1399.0	7590	15780
8	315.7	3510	7320
16	26.8	810	3480

Table 6.12. Comparison between parallel runs using two decomposition methods

6.6 Conclusion

In this section, the parallel performance of the parallel simulator for coupled fluid-heat flow and elastoplasticity described in Section 2.2 is profiled in several case studies considering liquid injection, liquid production, plasticity, and matrix decomposition. Scalable results and practical speedups are obtained in the parallel runs. The portable parallel scheme does not require significant code re-development efforts and can be ported to serial coupled codes with similar structured easily. In conclusion:

(1) The best speedups are usually obtained at 32 processes, and the increase from 32 to 64 processes does not effectively improve the parallel performance for both flow and geomechanics problems.

(2) Nearly ideal scalability for the coupled simulation is obtained for up to 16 processes. Therefore, when the hardware is limited, 8- or 16-process runs are deemed practical.

(3) The overall scalability of the coupled flow and geomechanics simulation is still honored after the flow and the geomechanics problems are coupled.

(4) Workload imbalance among processes is observed when plasticity is introduced. The imbalance increases as the plasticity region expands.

(5) The new matrix decomposition method reduces MPI communication costs and the solver iterations.

7 CONCLUSIONS AND FUTURE WORK

7.1 Conclusions

In this work, two coupled flow and geomechanics simulators are presented. The first simulator is fully coupled and is based on finite element methods. It is used to study the effects of geomechanics on well performance and reservoir response, the stress and pressure evolutions at the infill location, and interwell interference. The second simulator is sequentially coupled, with the flow problem discretized by the finite volume method and the geomechanics problem discretized by the finite element method. The development of this simulator includes a portable parallelization scheme leading to practical speedups. Some aspects presented in this study which serve as a complement to the literature are listed as follows. The novelty of this work also lies in them.

(1) Geomechanical effects on well production and reservoir pressure in unconventional reservoirs are comprehensively modeled by the coupled flow and geomechanics simulator. Previous studies either used simplified geomechanics consideration (Yu and Sepehrnoori 2014) or did not consider several relevant parameters (An et al. 2017; Moradi et al. 2017).

(2) The study of production-induced stress state changes indicates that when the infill well is located in the area of an unconventional reservoir with known connections of existing fractures, legacy production of parent wells can have insignificant effects on the stress reversal at and around the infill well. This was not specifically observed in related studies.

(3) Non-uniform fracture half-lengths with dense distributions along parent wells are considered in the sensitivity analyses in this study. It incorporates features of parent well fracture geometries proved by field observations and fracture modeling studies.

(4) The usage of non-uniform fracture half-lengths helps to capture frac hits in the modeling results, and the assumption of uniform fractures treated with SRV is not effective in capturing frac hits.

(5) A portable scheme is proposed for the parallelized coupled flow and geomechanics simulator using the fixed-stress sequential method. This proposed scheme reduces the code re-development efforts for parallelization and can be ported to sequential codes with similar structures for practical speedups.

Based on the numerical investigations carried out in the case studies in this work, some conclusions can be drawn as follows.

(1) Geomechanical considerations decrease the simulated production rates. The increase of geomechanical effects leads to the increase of pressure depletion and more production rate decrease. In general, rock properties indicating reduced stiffness lead to more production rate decrease. The effects of parameters investigated in the analyses can be ranked from the greatest to the lowest as fracture number > fracture length > Young's modulus > Poisson's ratio > Biot's coefficient. Besides, the significant geomechanical effects on production and pressure are observed at locations experiencing large pressure depletion, as rock deformation is always induced by pressure disturbance in the simulation.

(2) Decreasing BHP and differential stress both lead to increased stress reversal at the infill location. They also move forward the beginning of stress reversal. Parent well

operation and reservoir properties are also relevant parameters impacting the stress reorientation at the infill location. Along the infill well, areas closer to parent well fracture tips have faster stress reversal and more S_{hmin} decrease. In addition, if the infill well lateral penetrates through known fractures connecting parent wells, the stress at the unfractured infill zones is not significantly reversed by parent well production.

(3) For the simulation of the hydraulic fracture propagations along the infill well, the assumption of uniform parent well fractures is not effective in generating frac hits between parent and infill well fractures. The use of parent well fractures with non-uniform half-lengths helps to capture frac hits whose existence is proved by field reports. The reason why non-uniform fracture half-lengths lead to frac hits is that the tips of the shorter parent well fractures experience strong stress reversal. This local stress reversal diverts infill well propagation in the longitudinal direction and makes infill well fractures hit adjacent parent well fractures.

(4) Differential stress and legacy production have significant effects on the resulting infill well fractures during the completion of the infill well. Perforation cluster locations have limited effects on how infill wells propagate longitudinally or transversely, but they affect the stress path an infill well fracture takes and contribute to frac hits. If fracturing interference is considered in the simultaneous propagation of multiple infill well fractures, the growth of the central fracture is inhibited by adjacent fractures due to stress shadow effects, and this inhibition becomes weaker as the fracture spacing increases.

(5) As parent well fracture geometry becomes more complex, the resulting stress evolution also becomes more heterogeneous. This increased heterogeneity leads to more

complex infill well fractures and interwell fracturing interference. However, the heterogeneity does not always lead to frac hits. It avoids frac hits in certain locations.

(6) The optimum speedup of the parallel simulation is usually obtained at 32 processes. Increasing to 64 processes does not improve the computational speed, and it actually decreases the parallel efficiency. For the parallel performance of the overall coupled simulator, nearly ideal scalability can be obtained for up to 16 processes, indicating that if there is a hardware limitation, 16-process runs can provide practical speedups. Imbalance introduced by plasticity is observed in the parallel environment, and the imbalance becomes stronger as the number of cells experiencing plasticity increase. Additionally, the new decomposition methods proposed in the parallelization study reduces MPI communication time and reduces the required iteration number to reach convergence.

7.2 Future Work

Some continuations of the work presented in this study can be considered so that the more relevant aspects can be investigated. Some possible directions are suggested as follow.

(1) The coupled flow and geomechanics model can be used to examine the effect of fluid injection in parent wells on remediating the stress reversal caused by legacy production. Pilot studies in Bakken have been conducted and mixed performances were reported (Bommer et al. 2017; Bommer and Bayne 2018). They serve as the motivation for an injection investigation using the models presented in this study.

(2) After the establishment of the interwell fracture network consisting of parent and infill well fractures, hydrocarbon production simulation jointly from the parent and infill wells can be carried out so that the effects of infill well completion on infill well production and on existing parent well production can be quantified by actual production simulation results. Two methods to incorporate the infill well fractures are proposed. The first is to still use the structured gird, while EDFM (Extended Discrete Fracture Model) is added to denote the highly curved infill well fractures (Li and Lee 2008). The second is to convert the reservoir mesh to fully unstructured grid, and complex shapes of hydraulic fractures can be explicitly denoted by unstructured cells. The unstructured grid is actually not very complicated to incorporate in the simulator presented in Section 2.1, since the external library DEAL.II includes the capability to handle unstructured gird (Bangerth et al. 2007) and it can read such grids generated by external mesh generators. The open-source package of Gmsh is recommended for the generation of unstructured grids (Geuzaine and Remacle 2009). That is to say, natural fractures can also be included in the coupled flow and geomechanics simulator in future work by using EDFM and unstructured grids.

(3) More physical effects can be considered in the first simulator presented in Section 2.1. Capillary pressure, three-phase flow, thermal effects, and gas desorption can be included so that it simulates more subsurface phenomena in unconventional reservoirs.

(4) Numerical schemes suitable for the first simulator (presented in Section 2.1) can be developed to improve the finite element simulation efficiency. Since the fully coupled method leads to a highly heterogeneous Jacobian matrix at each time step, the current

matrix solution is based on the direct solver. Suitable preconditioning methods and solvers can be tested for the solution of the not-well-conditioned matrix. Parallel solutions can also be considered for this simulator.

(5) For the parallel solver presented in Section 2.2, parallel data input reading can be investigated as the reading time for the grid and the associated connection data for meshes with more than one million cells can be more than one hour. Besides, in addition to the GMRES solver used in the simulation, other solvers such as BiCG and BiCGSTAB can be tested as they may work better for certain geomechanics cases. Also, other preconditioning methods like multigrid and more sophisticated domain decomposition can be tested for better matrix solution efficiency.

REFERENCES

Abousleiman, Y., Cheng, A.D., Cui, L., Detournay, E. and Roegiers, J.C. 1996. Mandel's problem revisited. *Geotechnique* **46**(2):187-195.

Ajani, A.A. and Kelkar, M.G. 2012. Interference study in shale plays. Presented at SPE Hydraulic Fracturing Technology Conference, The Woodlands, Texas, USA, 6-8 February. SPE-151045-MS.

Ajisafe, F.O., Solovyeva, I., Morales, A., Ejofodomi, E., and Porcu, M.M. 2017a. Impact of Well Spacing and Interference on Production Performance in Unconventional Reservoirs, Permian Basin. Presented at Unconventional Resources Technology Conference, Austin, Texas, USA, 24-26 July. URTeC-2690466-MS.

Ajisafe, F., Shan, D., Alimahomed, F., Lati, S. and Ejofodomi, E., 2017b. An Integrated Workflow for Completion and Stimulation Design Optimization in the Avalon Shale, Permian Basin. Presnted at SPE Western Regional Meeting, Bakersfield, California, 23-27 April. SPE-185672-MS.

Alpak, F.O. 2015. Robust fully-implicit coupled multiphase-flow and geomechanics simulation. *SPE Journal* **20**(06):1-366.

Altmann, J.B., Müller, B.I.R., Müller, T.M., Heidbach, O., Tingay, M.R.P. and Weißhardt, A., 2014. Pore pressure stress coupling in 3D and consequences for reservoir stress states and fault reactivation. *Geothermics* **52**:195-205.

An, C., Fang, Y., Liu, S., et al. 2017. Impacts of Matrix Shrinkage and Stress Changes on Permeability and Gas Production of Organic-Rich Shale Reservoirs. Presented at

the SPE Reservoir Characterization and Simulation Conference and Exhibition, Abu Dhabi, 8-10 May. SPE-186029-MS.

Aziz, K. and Settari, A. 1979. *Petroleum Reservoir Simulation*. London: Elsevier.

Bai, T., Will, J., Eckardt, S., Chang, D., Lake, E., Madyarov, A., Xiao, X., Fay, M., Meij, R., Yuan, R., and Gao, Y. 2016. Hydraulic Fracture Modeling Workflow and Toolkits for Well Completion Optimization in Unconventionals. Presented at SPE Hydraulic Fracturing Technology Conference, The Woodlands, Texas, USA, 9-11 February. SPE-179137-MS.

Balay, S., Abhyankar, S., Adams, M., et al. 2014. PETSc Users Manual Revision 3.5. Argonne National Laboratory.

Bangerth, W., Hartmann, R. and Kanschat, G. 2007. DEAL.II—a general-purpose object-oriented finite element library. *ACM Transactions on Mathematical Software (TOMS)* **33**:4.

Bataee, M. and Irawan, S. 2014. Review of geomechanical application in reservoir modeling. *Journal of Applied Science* **14**(10):981-990.

Biot, M.A. 1941. General theory of three-dimensional consolidation. *Journal of Applied Physics* **12**(2):155-164.

Biot, M.A. 1955. Theory of elasticity and consolidation for a porous anisotropic solid. *Journal of Applied Physics* **26**(2):182-185.

Biot, M.A. and Willis, D.G. 1957. The elastic coefficients of the theory of consolidation. *Journal of Applied Mechanics* **24**:594-601.

Bommer, P.A. and Bayne, M.A. 2018. Active Well Defense in the Bakken: Case Study of a Ten-Well Frac Defense Project, McKenzie County, ND. Presented at SPE Hydraulic Fracturing Technology Conference and Exhibition, The Woodlands, Texas, 23-25 January. SPE-189860-MS.

Bommer, P., Bayne, M., Mayerhofer, M., Machovoe, M., and Staron, M. 2017. Re-Designing from Scratch and Defending Offset Wells: Case Study of a Six-Well Bakken Zipper Project, McKenzie County, ND. Presented at SPE Hydraulic Fracturing Technology Conference and Exhibition. SPE-184851-MS.

Cao, R., Li, R., Girardi, A., Chowdhury, N., and Chen, C. 2017. Well Interference and Optimum Well Spacing for Wolfcamp Development at Permian Basin. Presented at Unconventional Resources Technology Conference, Austin, Texas, USA, 24-26 July. URTeC-2691962-MS.

Chin, L.Y. and Thomas, L.K. 1999. Fully coupled analysis of improved oil recovery by reservoir compaction. Presented at SPE Annual Technical Conference and Exhibition, Houston, Texas, USA, 3-6 Oct. SPE-56753-MS.

Chin, L.Y., Thomas, L.K., Sylte, J.E., and Pierson, R.G. 2002. Iterative coupled analysis of geomechanics and fluid flow for rock compaction in reservoir simulation. *Oil & Gas Science and Technology* **57**(5):485-497.

Chueh, C.C., Secanell, M., Bangerth, W., and Djilali, N. 2010. Multi-level adaptive simulation of transient two-phase flow in heterogeneous porous media. *Computers & fluids* **39**(9):1585-1596.

Cipolla, C.L., Fitzpatrick, T., Williams, M.J., and Ganguly, U.K. 2011. Seismic-to-simulation for unconventional reservoir development. Presented at the SPE Reservoir Characterization and Simulation Conference and Exhibition. SPE, Abu Dhabi, UAE, 9-11 October. SPE-146876-MS.

Cipolla, C.L., Lolon, E.P., Mayerhofer, M.J., and Warpinski, N.R. 2009. Fracture Design Considerations in Horizontal Wells Drilled in Unconventional Gas Reservoirs. Presented at the SPE Hydraulic Fracturing Technology Conference, The Woodlands, Texas, 19-21 January. SPE-119366-MS.

Coussy, O. 1995. *Mechanics of Porous Continua*, original edition. Wiley.

Daneshy, A. 2011. Hydraulic Fracturing of Horizontal Wells: Issues and Insights. Presented at the SPE Hydraulic Fracturing Technology Conference, The Woodlands, Texas, 24-26 January. SPE-140134-MS.

Dagum, L. and Menon, R. 1998. OpenMP: an industry standard API for shared-memory programming. *IEEE computational science and engineering* **5**(1):46-55.

Dean, R.H., Gai, X., Stone, C.M., and Minkoff, S.E. 2006. A comparison of techniques for coupling porous flow and geomechanics. *SPE Journal* **11**(01):132-140.

Dean, R.H. and Schmidt, J.H. 2009. Hydraulic-fracture predictions with a fully coupled geomechanical reservoir simulator. *SPE Journal* **14**(04):707-714.

Esquivel, R. and Blasingame, T.A. 2017. Optimizing the Development of the Haynesville Shale—Lessons-Learned from Well-to-Well Hydraulic Fracture Interference. Presented at Unconventional Resources Technology Conference, Austin, Texas, USA, 24-26 July. URTeC-2670079-MS.

Gai, X., Dean, R.H., Wheeler, M.F., and Liu, R. 2003. Coupled geomechanical and reservoir modeling on parallel computers. Presented at SPE Reservoir Simulation Symposium, Houston, Texas, USA, 3-5 February. SPE-79700-MS.

Gakhar, K., Rodionov, Y., Defeu, C., Shan, D., Malpani, R., Ejofodomi, E., Fischer, K., and Hardy, B., 2017. Engineering an Effective Completion and Stimulation Strategy for In-Fill Wells. Presented at SPE Hydraulic Fracturing Technology Conference and Exhibition, The Woodlands, Texas, 24-26 January. SPE-184835-MS.

Geertsma, J. 1966. Problems of rock mechanics in petroleum production engineering. Presented at 1st ISRM Congress, Lisbon, Portugal, 25 September-1 October.

Geertsma, J. 1957. The effect of fluid pressure decline on volumetric changes of porous rocks. SPE-728-G.

Geuzaine, C. and Remacle, J.F. 2009. Gmsh: A 3-D finite element mesh generator with built-in pre-and post-processing facilities. *International journal for numerical methods in engineering* **79**(11):1309-1331.

Guo, X., Wang, Y., Killough, J. 2016. The application of static load balancers in parallel compositional reservoir simulation on distributed memory system. *Journal of Natural Gas Science and Engineering* **28**:447-460.

Guo, X., Kim, J., Killough, J. 2017. Hybrid MPI-OpenMP scalable parallelization for coupled non-isothermal fluid-heat flow and elastoplastic geomechanics. Presented at SPE Reservoir Simulation Conference, Montgomery, Texas, 20-22 February. SPE-182665-MS.

Guo, X., Song, H., Wu, K., Killough, J. 2018a. Pressure characteristics and performance of multi-stage fractured horizontal well in shale gas reservoirs with coupled flow and geomechanics. *Journal of Petroleum Science and Engineering* **163**:1-15.

Guo, X., Wu, K., Killough, J. 2018b. Investigation of production-induced stress changes for infill well stimulation in Eagle Ford Shale. *SPE Journal*. SPE-189974-PA. Preprint.

Guo, X., Song, H., Killough, J., Du, L., Sun, P. 2018c. Numerical investigation of the efficiency of emission reduction and heat extraction in a sedimentary geothermal reservoir: a case study of the Daming geothermal field in China. *Environmental Science and Pollution Research* **25**(5):4690-4706.

Guo, X., Wu, K., Killough, J., Tang, J. 2018d. Understanding the mechanism of interwell fracturing interference based on reservoir-geomechanics-fracturing modeling in Eagle Ford Shale. Presented at Unconventional Resources Technology Conference, Houston, Texas, 23-25 July. URTeC-2874464-MS.

Gupta, J., Zielonka, M., Albert, R.A., El-Rabaa, A.M., Burnham, H.A., and Choi, N.H. 2012. Integrated methodology for optimizing development of unconventional gas resources. Presented at SPE Hydraulic Fracturing Technology Conference, The Woodlands, Texas, USA, 6-8 February. SPE-152224-MS.

He, Y., Cheng, S., Li, S. et al. 2017a. A Semianalytical Methodology To Diagnose the Locations of Underperforming Hydraulic Fractures Through Pressure-Transient Analysis in Tight Gas Reservoir. *SPE Journal* **22**(3):924-939. SPE-185166-PA.

He, Y. Cheng, S., Li, L. et al. 2017b. Waterflood Direction and Front Characterization With Four-Step Work Flow: A Case Study in Changqing Oil field, China. *SPE Reservoir Evaluation & Engineering* **20** (3): 708–725. SPE-178053-PA.

He, Y., Cheng, S., Qin, J. et al. 2017c. Successful Application of Well Testing and Electrical Resistance Tomography To Determine Production Contribution of Individual Fracture and Water-breakthrough Locations of Multifractured Horizontal Well in Changqing Oil Field, China. Presented at the SPE Annual Technical Conference and Exhibition, San Antonio, Texas, 9-11 October. SPE-187285-MS.

Hendrickson, B. and Leland, R., 1993. The Chaco users guide. Version 1.0 (No. SAND--93-2339). Sandia National Labs., Albuquerque, NM (United States).

Hubbert, M.K. 1956. Darcy's law and the field equations of the flow of underground fluids. SPE-749-G.

Hughes, T. J. R. 1987. *The Finite Element Method: Linear Static and Dynamic Finite Element Analysis*. Englewood Cliffs: Prentice-Hall.

Hwang, J., Szabian, M.J., and Sharma, M. 2017. Hydraulic Fracture Diagnostics and Stress Interference Analysis by Water Hammer Signatures in Multi-Stage Pumping Data. Presented at Unconventional Resources Technology Conference, Austin, Texas, 24-26 July 2017.

Jia, C., Zheng, M. and Zhang, Y., 2012. Unconventional hydrocarbon resources in China and the prospect of exploration and development. *Petroleum Exploration and Development* **39**(2):139-146.

Karypis, G. and Kumar, V. 1995. METIS--unstructured graph partitioning and sparse matrix ordering system, version 2.0.

Kerr, R.A. 2010. Natural gas from shale bursts onto the scene. *Science* **328**(5986): 1624-1626.

Kim, J., Tchelepi, H.A., and Juanes, R. 2009. Stability, accuracy and efficiency of sequential methods for coupled flow and geomechanics. Presented at SPE reservoir simulation symposium, The Woodlands, Texas, 2-4 February. SPE-119084-MS.

Kim, J.,Tchelepi, H.A. and Juanes, R. 2011. Rigorous coupling of geomechanics and multiphase ow with strong capillarity. Presented at SPE Reservoir Simulation Symposium, The Woodlands, Texas, 21-23 February. SPE-141268-MS.

Kim, J., Moridis, G., Yang, D. and Rutqvist, J. 2012. Numerical studies on two-way coupled fluid flow and geomechanics in hydrate deposits. *SPE Journal* **17**(02):485-501.

Kim, J., Moridis G., Sonnenthal E. et al. 2014. TOUGH-ROCMECH User's Manual, Lawrence Berkeley National Laboratory, Berkeley, California.

King, G.E. and Valencia, R.L. 2016. Well Integrity for Fracturing and Re-Fracturing: What Is Needed and Why? Presented at SPE Hydraulic Fracturing Technology Conference, The Woodlands, Texas, USA, 9-11 February. SPE-179120-MS.

King, G.E., Rainbolt, M.F., and Swanson, C. 2017. Frac Hit Induced Production Losses: Evaluating Root Causes, Damage Location, Possible Prevention Methods and

Success of Remedial Treatments. Presented at SPE Annual Technical Conference and Exhibition, San Antonio, Texas, USA. 9-11 October. SPE-187192-MS.

King, M.J., Wang, Z., Datta-Gupta, A. 2016. Asymptotic Solutions of the Diffusivity Equation and Their Applications. Presented at SPE Europec featured at 78th EAGE Conference and Exhibition, Vienna, Austria, 30 May-2 June.

Kim, J., Tchelepi, H. A., and Juanes, R. 2011. Stability and Convergence of Sequential Methods for Coupled Flow and Geomechanics: Fixed-stress and Fixed-strain Splits. *Computer Methods in Applied Mechanical Engineering* **200**: 1591–1606.

Li, L. and Lee, S.H. 2008. Efficient field-scale simulation of black oil in a naturally fractured reservoir through discrete fracture networks and homogenized media. *SPE Reservoir Evaluation & Engineering* **11**(04):750-758.

Lindsay, G., Miller, G., Xu, T., Shan, D., and Baihly, J. 2018. Production Performance of Infill Horizontal Wells vs. Pre-Existing Wells in the Major US Unconventional Basins. Presented at SPE Hydraulic Fracturing Technology Conference and Exhibition, The Woodlands, Texas, USA, 23-25 January. SPE-189875-MS.

Liu, G. and Ehlig-Economides, C. 2015. Comprehensive Global Model for before-Closure Analysis of an Injection Falloff Fracture Calibration Test. Presented at the SPE Annual Technical Conference and Exhibition, Houston, Texas, USA. DOI: 10.2118/174906-MS.

Liu, G. and Ehlig-Economides, C. 2017. New Model for DFIT Fracture Injection and Falloff Pressure Match. Presented at the SPE Annual Technical Conference and Exhibition, 9-11 October, San Antonio, Texas, USA. doi:10.2118/187191-MS.

Luo, J., Chen, Z., Wang, K., Deng, H. and Liu, H. 2015. An efficient and parallel scalable geomechanics simulator for reservoir simulation. Presented at SPE/IATMI Asia Pacific Oil & Gas Conference and Exhibition, Nusa Dua, Bali, Indonesia, 20-22 October.

Manchanda, R., Bhardwaj, P., Hwang, J. and Sharma, M.M. 2018. Parent-Child Fracture Interference: Explanation and Mitigation of Child Well Underperformance. Presented at SPE Hydraulic Fracturing Technology Conference and Exhibition, The Woodlands, Texas, 23-25 January.

Mandel, J. 1953. Consolidation des sols (étude mathématique) (Consolidation of soild (mathematical study)). *Geotechnique **3***(7):287-299.

Marongiu-Porcu, M., Lee, D., Shan, D., and Morales, A. 2016. Advanced Modeling of Interwell-Fracturing Interference: An Eagle Ford Shale-Oil Study. *SPE Journal* **21**(05):1567-1582.

Malpani, R., Sinha, S., Charry, L., Sinosic, B., Clark, B., and Gakhar, K. 2015. Improving hydrocarbon recovery of horizontal shale wells through refracturing. Presented at SPE/CSUR Unconventional Resources Conference, Calgary, Alberta, Canada, 20-22 October. SPE-175920-MS.

Marongiu-Porcu, M., Lee, D., Shan, D., and Morales, A. 2015. Advanced Modeling of Interwell Fracturing Interference: an Eagle Ford Shale Oil Study. Presented in SPE Annual Technical Conference and Exhibition, Houston, Texas, 28-30 September.

McNamee, J. and Gibson, R.E. 1960a. Displacement functions and linear transforms applied to diffusion through porous elastic media. *Quarterly Journal of Mechanics and Applied Mathematics* **13**(1):98-111.

McNamee, J. and Gibson, R.E. 1960b. Plane strain and axially symmetric problems of the consolidation of a semi-infinite clay stratum. *Quarterly Journal of Mechanics and Applied Mathematics* **13**(2):210-217.

Mikelić, A. and Wheeler, M.F. 2013 Convergence of iterative coupling for coupled flow and geomechanics. *Computational Geosciences* **17**(3):455-61.

Miller, M.A., Jenkins, C.D., and Rai, R.R. 2010. Applying innovative production modeling techniques to quantify fracture characteristics, reservoir properties, and well performance in shale gas reservoirs. Presented at SPE Eastern Regional Meeting, Morgantown, West Virginia, 13-15 October.

Miller, G., Lindsay, G., Baihly, J., and Xu, T. 2016. Parent Well Refracturing: Economic Safety Nets in an Uneconomic Market. Presented at SPE Low Perm Symposium, Denver, Colorado, USA, 5-6 May. SPE-180200-MS.

Minkoff, S.E., Stone, C.M., Bryant, S., Peszynska, M., and Wheeler, M.F. 2003. Coupled fluid flow and geomechanical deformation modeling. *Journal of Petroleum Science and Engineering* **38**(1-2):37-56.

Moradi, M., Shamloo, A., and Dezfuli, A.D. 2017. A sequential implicit discrete fracture model for three-dimensional coupled flow-geomechanics problems in naturally fractured porous media. *Journal of Petroleum Science and Engineering* **150:**312-322.

Nagel, N., Zhang, F., Sanchez-Nagel, M., Lee, B., and Agharazi, A. 2013. Stress shadow evaluations for completion design in unconventional plays. Presented at SPE Unconventional Resources Conference Canada, Calgary, Alberta, Canada, 5-7 November.

Olson, Jon E. and Wu, K. 2012. Sequential versus Simultaneous Multi-zone Fracturing in Horizontal Wells: Insights from a Non-planar, Multi-frac Numerical Model. Presented at the SPE Hydraulic Fracturing Technology Conference in The Woodlands, Texas, USA 6-8 February. SPE-152602-MS.

Peaceman, D.W. 1978. Interpretation of well-block pressures in numerical reservoir simulation. *SPE Journal* **18**(3):183-194.

Portis, D.H., Bello, H., Murray, M., Barzola, G., Clarke, P., and Canan, K. 2013. Searching for the optimal well spacing in the Eagle Ford shale: A practical tool-kit. Presented at Unconventional Resources Technology Conference, Denver, Colorado, USA, 12-14 August. URTeC-1581750-MS.

Pruess K., Oldenburg C., and Moridis G. 1999. TOUGH2 User's Guide, Version 2.0. Report LBNL-43134, Lawrence Berkeley National Laboratory, Berkeley, California.

Railroad Commission of Texas. 2015. http://www.rrc.state.tx.us

Rainbolt, M.F. and Esco, J. 2018. Paper Title: Frac Hit Induced Production Losses: Evaluating Root Causes, Damage Location, Possible Prevention Methods and Success of Remediation Treatments, Part II. Presented at SPE Hydraulic

Fracturing Technology Conference and Exhibition, The Woodlands, Texas, USA, 23-25 January. SPE-189853-MS.

Reagan, M. T., Moridis, G. J., Freeman, C. M. et al. 2013. Massively Parallel Simulation of Production from Oceanic Gas Hydrate Deposits. Presented in International Petroleum Technology Conference, Beijing, China, 26-28 March. IPTC-17026-MS.

Rezaei, A., Rafiee, M., Bornia, G., Soliman, M., and Morse, S. 2017a. Protection Refrac: Analysis of Pore Pressure and Stress Change Due to Refracturing of Legacy Wells. Presented at Unconventional Resources Technology Conference, Austin, Texas, USA, 24-26 July. URTeC-2667433-MS.

Rezaei, A., Rafiee, M., Siddiqui, F., Soliman, M., and Bornia, G. 2017b. The Role of Pore Pressure Depletion in Propagation of New Hydraulic Fractures during Refracturing of Horizontal Wells. Presented at SPE Annual Technical Conference and Exhibition, San Antonio, Texas, USA, 9-11 October. SPE-187055-MS.

Roussel, N.P. and Sharma, M.M. 2011. Optimizing fracture spacing and sequencing in horizontal-well fracturing. *SPE Production & Operations* **26**(02):173-184.

Roussel, N.P., Florez, H., and Rodriguez, A.A. 2013. Hydraulic fracture propagation from infill horizontal wells. Presented at SPE Annual Technical Conference and Exhibition, New Orleans, Louisiana, 30 September-2 October. SPE-166503-MS.

Rutqvist, J. and Stephansson, O. 2003. The role of hydromechanical coupling in fractured rock engineering. *Hydrogeology Journal* **11**(1):7-40.

Rutqvist, J. 2017. An overview of TOUGH-based geomechanics models. *Computers & Geosciences* **108**:56-63.

Safari, R., Lewis, R., Ma, X., Mutlu, U., and Ghassemi, A. 2017. Infill-Well Fracturing Optimization in Tightly Spaced Horizontal Wells. *SPE Journal* **22**(02).

Settari, A. and Mourits, F.M. 1998. A coupled reservoir and geomechanical simulation system. *SPE Journal* **3**(03):219-226.

Settari, A. and Walters, D.A. 2001. Advanced in coupled geomechanics and reservoir modeling with application to reservoir compaction. *SPE Journal* **6**(3):334-342.

Shovkun, I. and Espinoza, D.N. 2017. Coupled fluid flow-geomechanics simulation in stress-sensitive coal and shale reservoirs: Impact of desorption-induced stresses, shear failure, and fines migration. *Fuel* **195**:260-272.

Simpson, M.D., Patterson, R., and Wu, K. 2016. Study of Stress Shadow Effects in Eagle Ford Shale: Insight from Field Data Analysis. Presented at 50th US Rock Mechanics/Geomechanics Symposium, Houston, Texas, 26-29 June. ARMA-2016-190.

Song, H., Li, Z., Wang, Y., Zhu, W., Cao, Y., and Killough, J. 2015. A Novel Approach for Modeling Gas Flow Behaviors in Unconventional Reservoirs with Nanoporous Media. Presented at International Petroleum Technology Conference, Doha, Qatar, 6-9 December.

Tang, J., Wu, K., Zeng, B., Huang, H., Hu, X., Guo, X., Zuo, L. 2017. Investigate Effects of Weak Bedding Interfaces on Fracture Geometry in Unconventional Reservoirs. *Journal of Petroleum Science and Engineering*. doi: 10.1016/j.petrol.2017.11.037.

Terzaghi, K. 1923. Die Berechnung der Durchassigkeitsziffer des Tones aus dem Verlauf der hydrodynamischen Spannungserscheinungen. *Akademie der Wissenschaften in Wien. Sitzungsberichte* **11**:105-124.

Terzaghi, K. 1925. *Erdbaumechanik auf bodenphysikalischer Grundlage (Mechanics of earthworks based on rudiments of soil physics).* Deuticke.

Thomas, L., Chin, L., Pierson, R., et al. 2002. Coupled Geomechanics and Reservoir Simulation. Presented at SPE Annual Technical Conference and Exhibition, San Antonio, Texas, 29 September-2 October. SPE-77723-MS.

Tran, D., Settari, A., and Nghiem, L. 2004. New iterative coupling between a reservoir simulator and a geomechanics module. *SPE Journal* **9**(03):362-369.

Ugueto, C., Gustavo, A., Huckabee, P.T., Molenaar, M.M., Wyker, B., and Somanchi, K. 2016. Perforation cluster efficiency of cemented plug and perf limited entry completions; Insights from fiber optics diagnostics. Presented at SPE Hydraulic Fracturing Technology Conference, The Woodlands, Texas, 9-11 February.

Vermylen, J.P. 2011. Geomechanical studies of the Barnett shale, Texas, USA. Doctoral dissertation, Stanford University.

Verruijt, A. 2013. Theory and problems of poroelasticity. Delft University of Technology.

Wan, J., Durlofsky, L.J., Hughes, T.J.R., and Aziz, K., 2003. Stabilized finite element methods for coupled geomechanics-reservoir flow simulations. Presented in SPE Reservoir Simulation Symposium, Houston, Texas, 3-5 February.

Wang, Y. and Killough, J. E. 2014. A New Approach to Load Balance for Parallel/Compositional Simulation Based on Reservoir-Model Overdecomposition. *SPE Journal* **19** (02):304-315.

Wang, Z., Chen, L., King, M.J. 2017. Validation and Extension of Asymptotic Solutions of Diffusivity Equation and Their Applications to Synthetic Cases. Presented at SPE Reservoir Simulation Conference, Montgomery, Texas, USA, 20-22 February.

Wang, Z., Park, J., Xue, X., King, M.J., Datta-Gupta, A. 2018. Quantitative Production and Buildup Data Analysis From Unconventional Reservoirs Using a Novel w(τ) Formulation. Presented at EAGE European Conference on the Mathematics of Oil Recovery, Barcelona, Spain, 3-6 September.

Webster, P., Cox, B., and Molenaar, M. 2013. Developments in diagnostic tools for hydraulic fracture geometry analysis. Presented at Unconventional Resources Technology Conference, Denver, Colorado, USA, 12-14 August. URTEC-1619968-MS.

Weijermars, R., Sorek, N., Sen, D., and Ayers, W.B. 2017. Eagle Ford Shale play economics: US versus Mexico. *Journal of Natural Gas Science and Engineering* **38**:345-372.

Weng, X., Kresse, O., Chuprakov, D., Cohen, C.E., Prioul, R., and Ganguly, U. 2014. Applying complex fracture model and integrated workflow in unconventional reservoirs. *Journal of Petroleum Science and Engineering* **124**:468-483.

Wheaton, B., Miskimins, J., Wood, D., Lowe, T., and Barree, R. 2015. Integration of distributed temperature and distributed acoustic survey results with hydraulic

fracture modeling: a case study in the Woodford shale. Presented at Unconventional Resources Technology Conference, Denver, Colorado, USA, 25-27 August. URTeC-1922140-MS.

Wheeler, M.F. and Gai, X., 2007. Iteratively coupled mixed and Galerkin finite element methods for poro-elasticity. *Numerical Methods for Partial Differential Equations* **23**(4):785-797.

White, J., Castelletto, N., and Tchelepi, H. 2016. Block-Partitioned Solvers for Coupled Poromechanics: A Unified Framework. *Computer Methods in Applied Mechanics and Engineering* **303**:55-74.

Wu, K. and Olson, J.E. 2015a. Simultaneous multifracture treatments: fully coupled fluid flow and fracture mechanics for horizontal wells. *SPE Journal* **20**(02):337-346.

Wu, K. and Olson, J. E. 2015b. A simplified three-dimensional displacement discontinuity method for multiple fracture simulations. *International Journal of Fracture* **193**(02):191-204.

Wu, K., Olson, J., Balhoff, M.T., and Yu, W. 2016. Numerical analysis for promoting uniform development of simultaneous multiple-fracture propagation in horizontal wells. *SPE production & operations* **32**(01):41-50.

Wu R., Kresse, O., Weng, X., Cohen, C., and Gu, H. 2012. Modeling of interaction of hydraulic fractures in complex fracture networks. Presented at SPE Hydraulic Fracture Technology Conference, Texas, USA, 6-8 February. SPE-152052-MS.

Xie, J., Huang, H., Ma, H., Zeng, B., Tang, J., Yu, W., Wu, K. 2018. Numerical Investigation of Effect of Natural Fractures on Hydraulic-fracture Propagation in

Unconventional Reservoirs. *Journal of Natural Gas Science and Engineering* **54**:143-153.

Yaich, E., Diaz De Souza, O.C., Foster, R.A., and Abou-sayed, I.S. 2014. A Methodology to Quantify the Impact of Well Interference and Optimize Well Spacing in the Marcellus Shale. Presented at SPE/CSUR Unconventional Resources Conference–Canada, Calgary, Alberta, Canada, 30 September-2 October. SPE-171578-MS.

Yang, D. 2013. A Simulator with Numerical Upscaling for the Analysis of Coupled Multiphase Flow and Geomechanics in Heterogeneous and Deformable Porous and Fractured Media. Doctoral dissertation, Texas A&M University. Available electronically from http://hdl.handle.net/1969.1/151194.

Yang, D., Moridis, G.J., and Blasingame, T.A. 2014. A fully coupled multiphase flow and geomechanics solver for highly heterogeneous porous media. *Journal of Computational and Applied Mathematics* **270**:417-432.

Yu, W. and Sepehrnoori, K. 2014. Simulation of gas desorption and geomechanics effects for unconventional gas reservoirs. *Fuel* **116**:455-464.

Zhou, D., Zhang, G., Zhao, P., Wang, Y. and Xu, S. 2017. Effects of post-instability induced by supercritical CO 2 phase change on fracture dynamic propagation. *Journal of Petroleum Science and Engineering* **162**:358-366.

Zoback, M.D. 2007. *Reservoir geomechanics*. Cambridge University Press.